Multiple-Input Multiple-Output Optical Wireless Communications

Trần, Tuấn-Anh

Balliol College

Supervisor: **Prof. Dominic C. O'Brien**

Trinity Term 2013

A thesis submitted in partial fulfilment of the
requirements for the degree of Doctor of Philosophy at the
University of Oxford

Communications Research Group
Department of Engineering Science
University of Oxford
Parks Road, Oxford OX1 3PJ

Abstract

Visible-light optical wireless communications (OWC) is a potential technology that can help resolve the crowdedness of the radio-frequency bands, whilst conveniently exploiting energy-saving light-emitting diodes (LEDs) as transmitters for both illumination and communications. Since there usually are many LEDs in a lighting unit, OWC has a multi-input multi-output (MIMO) geometry which, thanks to its channel diversity, can offer wireless local networks at data-rates many times higher than possible with single-channel systems.

In such systems, MIMO-detection methods to separate the different optical channels play an important role in improving the system performance by helping reduce cross-talk between channels. To measure the performance of a particular geometry for MIMO communications, a simulation study, reported in this thesis, found that, amongst the signal-independent metrics, the condition number may be used as a rough predictor of the performance, whilst the channel Signal-to-Interference-and-Noise Ratio (SINR) is the most appropriate for geometry assessment. Combined with the fact that the overall performance of a MIMO system is mostly dominated by its worst channel, this indicates that the most effective way to improve the system performance is to maximise the worst channel's SINR.

One of the possible solutions to improving the SINRs is to use holograms to steer the transmitter images such that their distributions over the photo-detectors reduce overlaps. As LEDs emit partially-coherent light, the beam steering has to be carried out with partially-coherent illumination. By using two lenses to parallelise and collect partially-coherent light before and after the hologram, respectively, the source and image intensity distributions, and the autocorrelation of the hologram can be related in a succinct mathematical relationship.

This leads to the development of three computational algorithms based on the autocorrelation function to obtain a quantised hologram with the desired beam-steering capability. These algorithms have their cost functions and performance comparison done at the hologram plane instead of the image plane, which therefore takes less time than traditional image-based methods. Specifically, one of these algorithms is able to save significant time over both the other autocorrelation-based algorithms and the direct binary-search, by 33% and by 50% respectively.

A simulation-based study and a corresponding experiment, both reported in this thesis, found that the one of the proposed algorithms had poor power efficiency, whilst the other two were both highly effective in generating digital holograms with precise and power-efficient beam-steering performance. Of these two algorithms, one had superior time performance and was likely the best of the three proposed autocorrelation-based algorithms for generating beam-steering holograms.

MIMO-OWC simulation also demonstrated the capability of using beam-steering holograms to design the channel and improve the system performance. Combining reported findings, a strategy can be devised to optimise the throughput of an imaging MIMO-OWC system for a given transmitted power.

Acknowledgements

I would like to thank Prof. Dominic O'Brien, for his invaluable discussions and advice which enabled all my research, as well as for his general supervision of my work. I am also very grateful for his immense patience with my progress, which at times could have sped up a lot more had I not digressed into various other things.

I would like to express my gratitude to Mr Grahame Faulkner for his kind assistance with everything laboratory-related, for his tolerance of my ineptitude with experiments, and for being always up for a good chat.

The long years of research were made much more enjoyable by the presence of the jovial bunch at the Communications Research Group and all the wits at the Vietnamese Society at Oxford. Trang, Công, Hùng, Phi Anh, Helmi, Hyunchae, Yue, Leilei, Ning, Chris, Ariel and many others: I am really thankful to have you all as my friends, for all the procrastination and convivial bantering—it's good life!

An Oxford student cannot fail to mention his college, and Balliol exemplifies all that is of a great institution. I am indebted to the College for always extending the utmost help, and for having granted me all the exciting opportunities to see the world.

I would also like to acknowledge the generosity of the Clarendon Scholarship Fund that made this DPhil possible.

Finally, and most importantly, I wanted to thank my family for always standing next to me, supporting me, and being the source of everything I have today. I must have done mountains of good deeds in my previous lives to have been born into this wonderful family.

Con cám ơn Bố, Mẹ và tất cả mọi người trong gia đình đã cho con ngày hôm nay.

List of Publications

[1] **Tran, T.-A.**; O'Brien, D.C. (2013) *An autocorrelation-based hologram-design algorithm for beam-steering with partially coherent illumination* – Applied Optics (submitted)

[2] **Tran, T.-A.**; O'Brien, D.C. (2013) *LED holographic beam-steering for visible-light communications* – 2013 IEEE GLOBECOM Workshops on Optical Wireless Communications (in print)

[3] **Tran, T.-A.**; O'Brien, D.C. (2012) *Performance metrics for Multi-Input Multi-Output (MIMO) Visible Light Communications* – 2012 Int'l Workshop on Optical Wireless Communications, pp.1-3, Oct 2012

[4] Azhar, A.H.* and **Tran, T.-A.***; O'Brien, D.C. (2010) *Demonstration of high-speed data transmission using MIMO-OFDM visible light communications* – 2010 IEEE GLOBECOM Workshops on Optical Wireless Communications, pp.1052-1056, Dec 2010 (* equal contributions)

Table of Contents

Table of Figures

Mathematical symbols

t	Scalar
$\vec{\boldsymbol{t}}$	Vector of scalars t_i
$\underline{\boldsymbol{T}}$	Matrix composed of vectors $\vec{\boldsymbol{t}}_{\boldsymbol{i}}$
$s(t)$	Input symbol stream to MIMO system
$x(t)$	Input electrical signal in MIMO system
$P(t)$	Transmitted optical signal in MIMO system
$y(t)$	Received electrical signal in MIMO system
$\underline{\boldsymbol{H}}$	Channel matrix
h	Element of $\underline{\boldsymbol{H}}$; and optical channel gain
$\underline{\boldsymbol{G}}$	MIMO-detection matrix
$\mathrm{cond}(\underline{\boldsymbol{H}})$	Condition number of $\underline{\boldsymbol{H}}$
σ^2	Spectral power
$\underline{\boldsymbol{C}}$	Covariance matrix
$\tilde{T}$	Fourier Transform of function T
K	Hologram field distribution
R_{KK}	Autocorrelation of K
P_{accept}	Probability of accepting the proposed change
$*$	Scalar-convolution operator
$\otimes$	Vector-convolution operator
$\mathcal{F}\{\ \}$	Fourier Transform operator

Abbreviations

AWGN	Additive white Gaussian noise
BER	Bit-error rate
BPSK	Binary phase-shift keying
CCD	Charge coupled device
CSI	Channel state information
CSIR	CSI available at Rx only
CSIT	CSI available at Rx and Tx
FFT	Fast Fourier Transform
FLCOS	Ferroelectric liquid-crystal on silicon
IM/DD	Intensity modulation / Direct detection
IR	Infra-red
ISI	Inter-symbol interference
LED	Light-emitting diode
LoS	Line-of-sight
LR	Lattice-Reduction
MIMO	Multi-input multi-output
ML	Maximum likelihood
MMSE	Minimum mean-squared-error
NRZ-OOK	Non-return-to-zero on-off keying
OFDM	Orthogonal frequency-division multiplexing
OWC	Optical wireless communications
PCB	Printed circuit board
QAM	Quadrature amplitude modulation
RCLED	Resonant-cavity LED
RF	Radio frequency
Rx	Receiver
SER	Symbol-error rate
SINR	Signal-to-interference-and-noise ratio
SISO	Single-input single-output
SLM	Spatial light modulator
SNR	Signal-to-noise ratio
SXGA	Super extended graphics array
Tx	Transmitter
VBLAST	Vertical Bell Laboratories layered space-time
WLAN	Wireless local area network
ZF	Zero-forcing

Chapter I. Introduction to Multi-Input Multi-Output Optical Wireless Communication

A. Optical wireless communication

In the last decade, wireless local-area networks (WLAN) have become ubiquitous [2]. These WLAN systems are based predominantly on radio-frequency (RF) transmission as defined by various IEEE specifications [2, 3]. Despite their widespread use, RF-based communication systems have three main disadvantages:

- RF systems often require complex modulation and multiplexing schemes [2]. One reason is to accommodate multiple high-speed channels with a system bandwidth of only tens of MHz [3]. Another reason is to minimise interference to and from nearby access-points, since RF radiation can penetrate walls and other non-metallic barriers [2].

- RF-based WLANs operate within a strictly-regulated spectrum [4] which is already crowded, as depicted in [5].

- The spectrum used by RF-based WLANs is shared by medical appliances [4] leading to possible adverse radiation interference in critical environments such as hospitals [6].

In light of these constraints to RF-based technologies, since the 1980s, there has been research into optical wireless communication (OWC). Originally optical carriers were viewed as a competitor with RF carriers for industrial adoption (see ref.1-12 of [7], ref.1-3 of [8]). Recently, as the RF bands become almost full, there has been a trend to move the wireless carriers into higher, unregulated bands [9, 10]. OWC may offer simpler alternatives to the complex RF systems. The advantages of OWC over RF communication are:

- Its frequency bands are very broad – 350THz for the visible spectrum alone. This permits many more MHz-wide channels than possible in the RF systems [9-11].

- Visible-light and infra-red bands are currently unregulated (for example, see [4, 5]), which allows for essentially unconstrained development of OWC technologies, as well as easy worldwide adoption (*i.e.* no regulation-compatibility issues) [12].

- At the wavelengths of hundreds of nanometres, multipath fading is a negligible effect on the propagation of OWC carriers [13]. The link designs for OWC systems can thus be much simpler than for RF systems [9, 10, 12].

- The easy blockage of optical carriers by walls and everyday objects make OWC well-confined. Interference between adjacent OWC systems is thus far less of an issue than with RF. Hence the transmitted power can be significantly increased, only limited by eye-safety concerns [11, 12]. And the pressure on security, a major factor in RF systems [2], is reduced thanks to the absence of casual behind-the-wall eavesdropping in OWC [9].

For a summary comparison between RF links and OWC links, see [12].

Early research efforts in OWC were mainly concerned with infra-red (IR) systems [7-10, 12, 14]. However, recently there has been a surge of interest in solid-state lighting as a more energy-efficient technology to replace the incandescent and fluorescent lights [15-18]. Furthermore, eye-safety regulations are far less restrictive for visible light than for IR [19-21]. Thus OWC using the visible spectrum has been gaining in significance, with several application scenarios currently being studied: see [11, 22] for overviews of current research trends and commercial interests in visible-light OWC, and [23] for a demonstration. Recently, visible-light OWC over short ranges has been adopted into an industrial standard [24].

As with IR [12], all visible-light OWC systems are partially coherent and employ intensity-modulation / direct-detection (IM/DD) with photo-detector receivers [25-34]. Also, numerous efforts have been spent into researching the white Light-Emitting Diode (LED) of solid-state lighting as the OWC transmitters. Most of these endeavours in improving capacities of systems using white LEDs can be broadly classified into manipulating signal properties and signal processing [25-29], or experimenting with the geometry of the links [30-34].

Research into signal-processing techniques in this area aims to increase data-rates by widening either the effective bandwidths using frequency-equalisation [25, 27-29] or the physical bandwidth of the most limiting component—the LEDs [26].

B. Channel geometry and Multi-Input Multi-Output

Although channel-geometry research already attracted interest with IR-based OWC [7-10], recently the channel geometry of visible-light OWC has also gained research attention [30-34]. Due to the identical propagation of IR radiation and visible light [35], studies of IR geometries and channel properties have been adopted for visible-light systems.

Figure 1a shows the OWC geometry for a single-input single-output (SISO) channel, with a single white-LED system acting as both the lighting source of the room and the OWC transmitter (Tx). The receiver (Rx) is a photo-detector with additional optical concentrators. Light travels from the Tx to the Rx in a line of sight (LoS) and by diffuse paths off room surfaces. The SISO-OWC LoS connection is generally maintained by tracking mechanisms [10].

Figure 1b also shows the SISO-OWC geometry, but for the diffuse-only link. As can be seen from this figure, when the Tx-Rx line of sight is blocked, the SISO linkage has to rely on diffusive reflections of the light [8, 9, 12, 14]. Research into more complex diffuse systems is reported in [29-32].

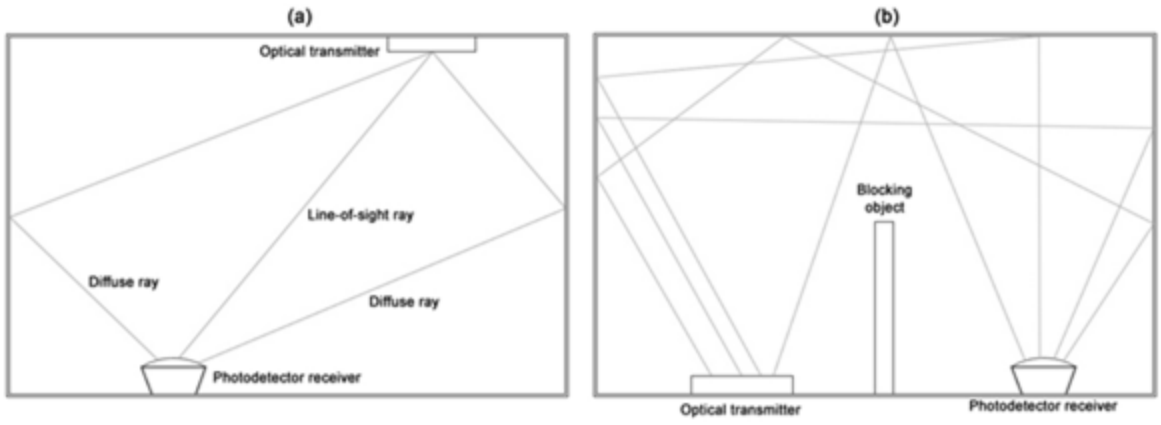

Figure 1. OWC geometry with 1 Tx and 1 Rx for (a) generic channel; (b) diffuse-only

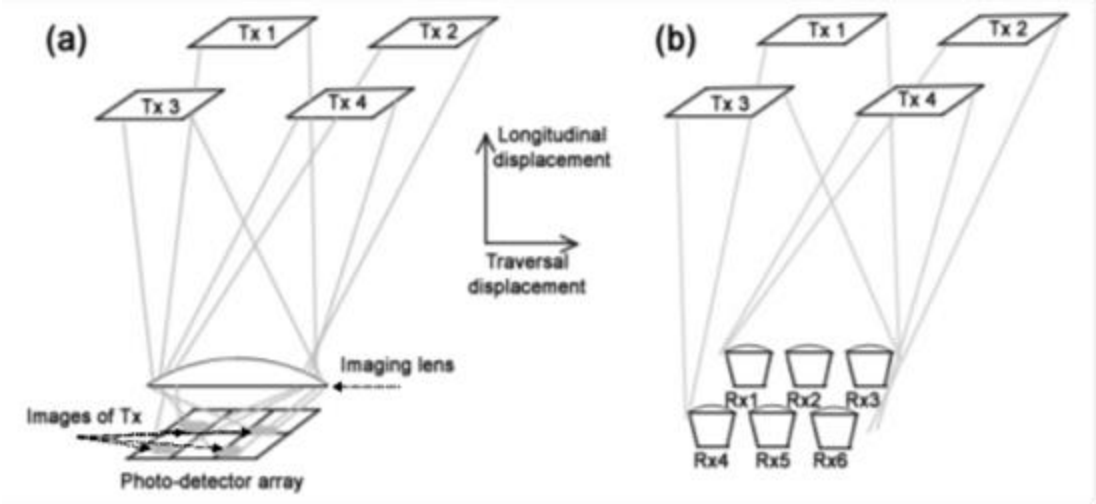

Figure 2. Schematic of 4-Tx 6-Rx MIMO systems: (a) Imaging, (b) Non-imaging

As reported in [9], the major drawbacks of OWC systems include high path-loss and high noise levels at the photo-detectors (mainly shot noise caused by ambient light.) Thus transmitted optical power is of importance to OWC performance. The LoS link, due to its shorter path and no diffusive loss, is more power-efficient than the diffuse link [35]. With the optical power limited by regulations [19-21], LoS channels are thus preferred to diffuse ones.

As reported in [18] a room will likely need many sets of LED light sources. By using these light sources as Tx for LoS channels [11, 25, 33], the benefits of a LoS multi-input multi-output (MIMO) system can be achieved.

Although MIMO techniques have long been widely used in RF communication to combat multipath-fading [13], recently a small body of research has been concerned with the adoption of MIMO in visible-light OWC. Figure 2 shows the LoS MIMO geometries for a typical OWC channel, depicted as consisting of 4 solid-state light-sources as the Tx, and an array of 6 photo-detectors in the Rx.

The MIMO technique allows multiple links to achieve the overall performance of a single link but at lower link-quality [13]. This equates to lower transmitted optical power for

each source at the same overall bit-rates. For the same transmitted optical power, a MIMO system performs better than SISO.

As the bandwidth of these sources are very limited (of the order of tens of MHz at maximum [28]) besides using equalisation schemes and complex modulation, the MIMO technique would allow multiple links to be established to increase data rates at multiple times of a single link. This however is done at lower link-quality [13]. This equates to lower transmitted optical power for each source at the same overall bit-rates. For the same transmitted optical power, a MIMO system performs better than SISO.

Furthermore, a single LoS link is susceptible to blockage. As can be seen from Figure 2, it is relatively more difficult to block all Tx-Rx links in these systems. Thus link outage is another advantage of LoS MIMO over LoS SISO.

As reported in [33], there are two typical geometries for LoS MIMO-OWC systems. Figure 2a depicts the imaging system, in which each Tx is imaged by a lens onto the receiver array. As such, the optical path between any pair of transmitter-receiver is conditional on the mapped image. In the non-imaging configuration as depicted in Figure 2b, there always exists an LoS linkage between a Tx and an Rx.

In MIMO systems, data from the Tx is transmitted through the OWC optical channels. Each Rx then collects the data from all the Tx (although differently attenuated). The Rx system decomposes the received signals into estimates of the transmitted data, using its knowledge of the channel information, which is formulated as a matrix. [33] reports that the imaging MIMO system yields better overall system performance than the non-imaging.

C. Beam-steering

The studies described in the previous section deal with the design of a passive geometry which would likely be more appropriate for systems with devices being stationary or of very limited mobility. To re-design the geometry for a wider range of configurations, active elements are required. There has been substantially less research conducted in this area, the majority of which is for laser-based rather than (LED-based) visible-light systems [36-40].

Figure 3 shows a system that has the potential to send the light beam to required positions [41], and potentially to manipulate the optical distributions to create the desired pattern [37]. This technology can be broadly classified into two families: mechanical, and electrical.

The most common method of mechanical beam-steering uses micro-mirrors which deflect the light by electrically altering the angles of the mirrors [42]. These micro-electro-

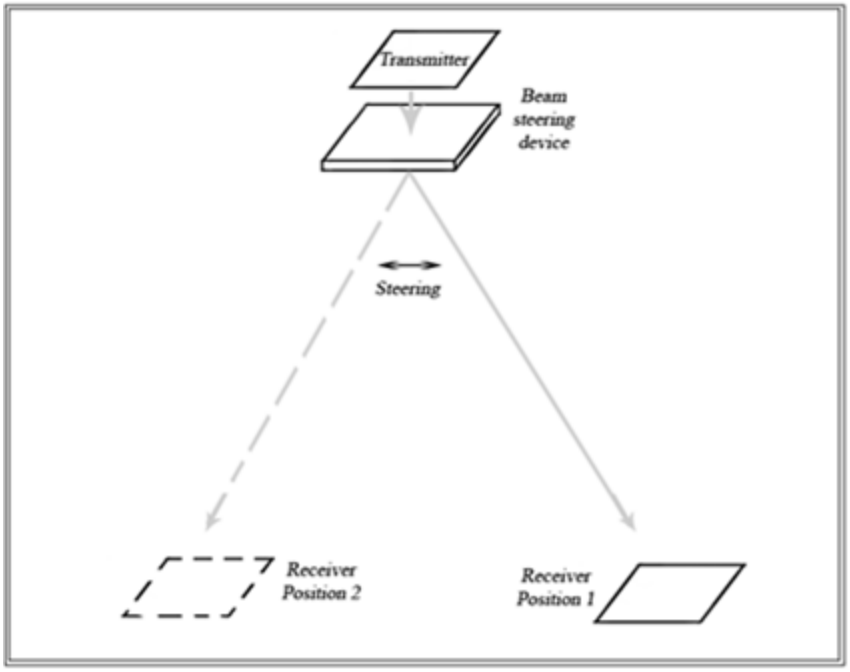

Figure 3. Schematic of an optical communication system with beam-steering

mechanical mirror systems have been widely available at linear sizes up to 2048 elements [43, 44] and deflection angles of ±12 degrees [42]. In addition, there are also beam-steering devices that employ mechanical translation of micro-lenses [45].

Non-mechanical steering devices are currently an active area of research, with several demonstrations of beam steering using a polarization-controlled diffractive element and a variable wavelength source [46]. It is also possible to use spatial light modulators (SLMs) as diffractive elements and achieve larger steering angles (*e.g.* see [47].) Other electrical techniques include: wavelength-based steering using a tunable source and a diffractive element [39]; waveguide and evanescent field techniques [48]; liquid-crystal prisms with changeable refractive index [36, 49]; liquid-filled lenses [50]; deformable lenses to steer and focus beams [51]; or true 'holographic' gratings in programmable media [52]. However, these types of devices often require complex optical systems for the programming mechanism.

Of these electrical devices, SLMs are perhaps the most promising for beam-steering and manipulation of the optical field due to their versatility and mature state of development. The most common SLMs are liquid-crystal silicon-backplane devices, first proposed in the 1980s [53]. The then-poor mirror quality led to poor diffraction efficiency, thus limited application. However, the recent surge in popularity of LCOS displays has made efficient LCOS SLMs available at reasonable cost.

Parallel to these SLM developments, there has also been development in holographic algorithms which make use of the LCOS SLMs for beam-steering. A digital hologram is generated algorithmically [32, 34, 37, 38, 54-67] and then displayed on the SLM to diffract light into the desired positions, as illustrated in Figure 3. Applications of these beam-steering holograms include optical switches [36, 41, 55, 57, 68], security patterns [63], free-space wave-front reconstruction [69, 70] and one-to-many communication systems [71]. However, these techniques mostly rely on coherent diffraction of the laser-emitted light and require

computationally-costly full propagation of light from the source to the image [32, 34, 37, 38, 53, 54, 56, 58, 59, 64, 65, 69, 72].

For optical wireless communications, the partially-coherent nature of the LED illumination makes the use of holograms less straightforward. General theories on the propagation of partially-coherent light have been available for nearly 80 years [73-75], but barring brief interest in the late 1980s and early 1990s (*e.g.* [57]), only recently have holograms started to be used with partially-coherent illumination [66, 70]. As such, partially-coherent beam-steering is much less mature as a technique than with coherent light, but its potential use with OWC which combines communication and illumination would offer great benefits at little additional complexity.

D. Scope and organisation of this thesis

For the more power-efficient LoS MIMO-OWC, two key questions are: How best can the transmitters and receivers be arranged to maximise the benefits of the MIMO geometry? And how can such optimal arrangements be realised?

The first part of this thesis concerns with finding the most suitable geometry-based metrics to measure the performance of MIMO geometric arrangements. Chapter II describes a representative model for the overall MIMO-OWC system, together with an analysis of the decomposition processing for MIMO signals. It also describes an analytical model of the MIMO-OWC channel matrix for future optimisation. Chapter III then investigates the overall performance and the geometry-based performance metrics, before describing a computer-based simulator for the MIMO-OWC system presenting simulation results.

The second part of the thesis focuses on developing a holographic beam-steering technique to improve MIMO-OWC performance. Chapter IV provides the theoretical analysis of the beam-steering architecture before proposing a new family of hologram-generating algorithms. Chapter V presents a computer-based simulator to assess the performance of the proposed algorithms. In Chapter VI, an experiment is described to verify the actual performance of the holograms generated with the proposed algorithms in steering beams for MIMO-OWC improvement.

Conclusions are drawn in Chapter VII, as well as future work to follow from the results presented in this thesis.

Chapter II. **MIMO-OWC system model**

Chapter I has presented an overview of research efforts in Optical Wireless Communication (OWC) in general, and in its Multiple-Input Multiple-Output architecture (MIMO-OWC) in particular. In this chapter, a MIMO-OWC system is described, including an effective electrical-equivalent equation and the link-budget of the system. The chapter also presents the available algorithms to detect MIMO channels into equivalent SISO ones. In the final part, the channel matrix is studied, with a theoretical model and an estimation algorithm introduced.

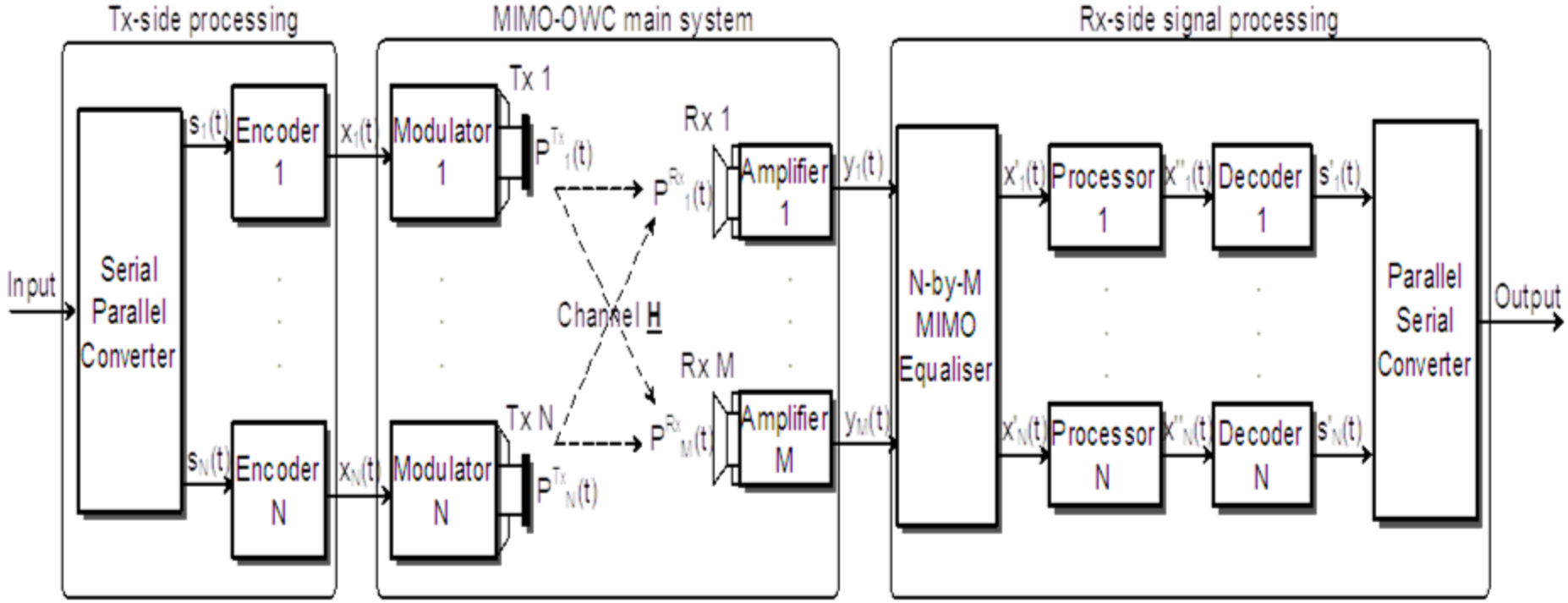

Figure 4. Block diagram of a MIMO-OWC system

A. Model of a MIMO-OWC system

1. Theoretical system-model for MIMO-OWC

Figure 5 depicts a MIMO-OWC system, whilst Figure 4 shows the electrical block diagram for such a system with N transmitters (Tx) and M receivers (Rx). A stream of data is fed into the system and is separated into N parallel streams $s_i(t)$ by a serial-to-parallel converter. Each of these N streams is encoded independently by an encoder module. The

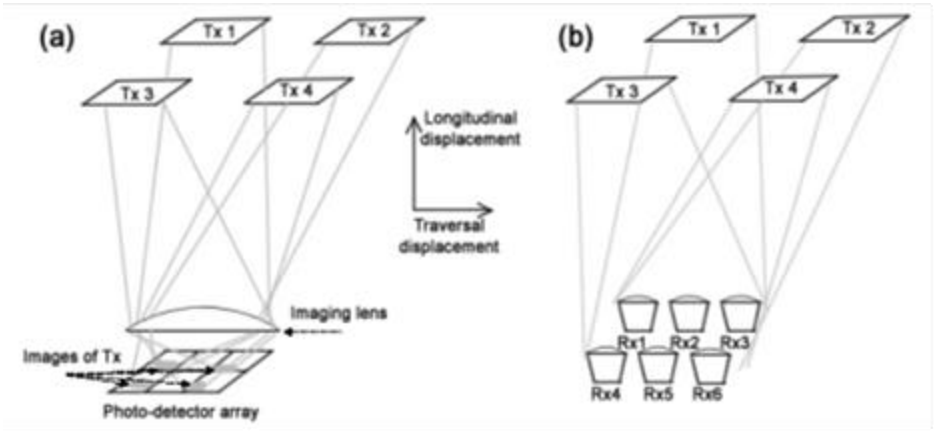

Figure 5. Schematic of 4-Tx 6-Rx MIMO systems: (a) Imaging, (b) Non-imaging

encoded digital stream $x_i(t)$ is then converted to an analogue signal and modulated to control the emitted power $P_i^{Tx}(t)$ of a corresponding LED-based Tx.

The light from the whole Tx system propagates through the OWC channel and is collected by each of the M photo-detectors in the Rx system. The received optical power $P_j^{Rx}(t)$ of each Rx is converted to a photo-current which is then amplified and sampled to give a digital signal. The M digital signals $y_j(t)$ are passed through a MIMO detector which gives N parallel outputs as recovered signals. Each of the recovered signals $x_i'(t)$ is then post-processed to give an estimate of the original digital signal $x_i(t)$. The estimated stream $x_i''(t)$

is then mapped to an appropriate constellation and decoded, including all error correction, to give an estimate $s_i'(t)$ of the original $s_i(t)$. The N parallel $s_i'(t)$ are then converted to a serial stream as the system output.

Overlooking the specifics of the encoding operation*, it can be seen that the effective inputs in this model are the N electrical-signal streams $x_i(t)$. Each of these is modulated onto an optical transmitter, most commonly a group of LEDs, and directly controls its optical-power output $P_i^{Tx}(t)$ [12] (also [26] for implementation). Since optical power is a non-negative quantity, there usually is a positive DC-level x_{DC} in the LED input to offset negative values of $x_i(t)$. The optical output $P_i^{Tx}(t)$ of the i^{th} Tx, of which the impulse response is $h_i^{Tx}(t)$, can thus be written as: ($*$ is the scalar-convolution operator)

$$P_i^{Tx}(t) = h_i^{Tx}(t) * (x_i(t) + x_{DC}) \qquad \text{Eq.1}$$

Note that Eq.1, x_{DC} is included to represent the fact that light intensity is non-negative, and has to be removed with electrical circuits in practice. In the simulation, however, for the sake of simplicity, x_{DC} and the corresponding DC-removing circuits were not implemented.

As discussed in [12], most OWC systems are based on Intensity Modulation and Direct Detection (IM/DD). Thus, if the optical impulse-response of the channel between the i^{th} Tx and the j^{th} Rx is $h_{ji}(t)$, the total optical power $P_j^{Rx}(t)$ collected by the j^{th} Rx can be written as [76]:

$$P_j^{Rx}(t) = \sum_{i=1}^{N} h_{ji}(t) * P_i^{Tx}(t) \qquad \text{Eq.2}$$

If the combined impulse response of the j^{th} photo-detector Rx and amplifier is $h_j^{Rx}(t)$ then the photocurrent $y_j(t)$ including the added electrical noise $n_j(t)$ of the Rx electronics, is:

* Some effects of modulation schemes on the symbol detection performance are discussed in Chapter II.B.

$$y_j(t) = h_j^{Rx}(t) * P_j^{Rx}(t) + n_j(t) \qquad \text{Eq.3}$$

The whole transfer from the N inputs $x_i(t)$ to the M outputs $y_j(t)$ of the MIMO-OWC main system can be thus written in vector form:

$$\vec{\boldsymbol{y}}(t) = \underline{\boldsymbol{h}}_{Rx}(t) \otimes \underline{\boldsymbol{H}}(t) \otimes \underline{\boldsymbol{h}}_{Tx}(t) \otimes [\vec{\boldsymbol{x}}(t) + \vec{\boldsymbol{x}}_{\boldsymbol{DC}}(t)] + \vec{\boldsymbol{n}}(t) \qquad \text{Eq.4}$$

In which:

$\vec{\boldsymbol{y}}(t)$: M-element vector of the Rx photocurrents

$\vec{\boldsymbol{x}}(t)$, $\vec{\boldsymbol{x}}_{\boldsymbol{DC}}(t)$: N-element vectors of the Tx electrical inputs

$\underline{\boldsymbol{h}}_{Tx}(t)$: N-by-N diagonal matrix of the N Tx-side responses $h_i^{Tx}(t)$ with $i = 1..N$

$\underline{\boldsymbol{H}}(t)$: M-by-N matrix of the sub-channel responses $h_{ji}(t)$ with $i = 1..N, j = 1..M$

$\underline{\boldsymbol{h}}_{Rx}(t)$: M-by-M diagonal matrix of the M Rx-side responses $h_j^{Rx}(t)$ with $j = 1..M$

$\otimes$ is the vector-convolution operator, applied analogously to the dot-product $\cdot$

If the OWC channel is assumed to be line-of-sight (LoS) only, then according to [77] the impulse responses of the $M \cdot N$ sub-channels can each be modelled as a delta-function $h_{ji}\delta(t-\tau)$ with propagation delays τ and time-independent constant h_{ji}. Thus, Eq.4 can be recast for each Rx channel, neglecting the common delay:

$$y_j(t) = \sum_{i=1}^{N} h_{ji}\left(\left(h_j^{Rx}(t) * h_i^{Tx}(t)\right) * (x_i(t) + x_{DC})\right) + n_j(t) \qquad \text{Eq.5}$$

Since the effect of narrow bandwidth on performance of MIMO systems is outside the scope of this research, it is assumed either that the bandwidths of Tx and Rx frequency responses are both larger than the signal bandwidth; or that appropriate system-response

equalisation is applied to the signals in the signal-processing stage [25, 27, 28]. Therefore, for simplicity the effects of responses can be neglected to yield:

$$\vec{\boldsymbol{y}}(t) = \underline{\boldsymbol{H}} \times [\vec{\boldsymbol{x}}(t) + \vec{\boldsymbol{x}}_{\boldsymbol{DC}}(t)] + \vec{\boldsymbol{n}}(t) \qquad \text{Eq.6}$$

Eq.6 has the same form as the system equation used in MIMO-RF analyses [78-80]. Each element of $\underline{\boldsymbol{H}}$ now contains the geometry-dependent path-loss and both Tx and Rx gains. Eq.6 is thus an effective electrical-equivalent description of the MIMO-OWC system (see **Error! Reference source not found.**.)

The M received electrical signals $y_j(t)$ are then processed in the next stages of the Rx, as shown in **Error! Reference source not found.**. Firstly, the transmitted signals are estimated by applying an N-by-M matrix $\underline{\boldsymbol{G}}$ to $\vec{\boldsymbol{y}}(t)$:

$$\vec{\boldsymbol{x}}'(t) = \underline{\boldsymbol{G}} \times \vec{\boldsymbol{y}}(t) \qquad \text{Eq.7}$$

The estimate of each of the transmitted signals is then passed through an appropriate processor (see **Error! Reference source not found.**) during which the frequency responses can be equalised, and the DC component for LED bias is removed. The output signal for the i^{th} channel is:

$$x_i''(t) = (\vec{\boldsymbol{g}}_i \cdot \vec{\boldsymbol{h}}_i)x_i(t) + \sum_{k=1,k\neq i}^{N} (\vec{\boldsymbol{g}}_i \cdot \vec{\boldsymbol{h}}_k)x_k(t) + \vec{\boldsymbol{g}}_i \cdot \vec{\boldsymbol{n}}(t) \qquad \text{Eq.8}$$

($\vec{\boldsymbol{g}}_i$, $\vec{\boldsymbol{h}}_k$ are the i^{th} row of $\underline{\boldsymbol{G}}$ and k^{th} column of $\underline{\boldsymbol{H}}$, respectively)

The N decoders $\vartheta_i\{\cdot\}$ then demodulate the N elements of this time-slice vector using the appropriate constellations and perform decoding to obtain the estimates $s_i'(t)$ of the symbols $s_i(t)$:

$$s_i'(t) = \vartheta_i\{x_i''(t)\} \qquad \text{Eq.9}$$

2. Power constraints and link-budget calculations

Eye-safety regulations (see [19-21]) constrain the emitted power of optical sources [19-21, 81] and thus influence link-budgets and OWC power allocations. From Eq.1, it can be seen that the output power of an intensity-modulated source is related directly to the signal amplitude. Rewriting Eq.1 with the assumption of a broad Tx frequency-response:

$$P_i^{Tx}(t) = h_i^{Tx}(x_i(t) + x_{DC}) = h_i^{Tx}x_i(t) + P_{DC} \qquad \text{Eq.10}$$

The constraint to optical output power for a single Tx can be written as:

Average: $$\langle P_i^{Tx}(t)\rangle = h_i^{Tx}\langle x_i(t)\rangle + P_{DC} \le P_{\max}^{av} \qquad \text{Eq.11}$$

Peak: $$\max_t\left(P_i^{Tx}(t)\right) = h_i^{Tx}\max_t\left(x_i(t)\right) + P_{DC} \le P_{\max}^{peak} \qquad \text{Eq.12}$$

Substituting Eq.10 into Eq.8 yields:

$$x_i''(t) = \frac{\vec{\boldsymbol{g}}_i \cdot \vec{\boldsymbol{h}}_i}{h_i^{Tx}}(P_i^{Tx}(t) - P_{DC}) + \sum_{k=1,k\neq i}^{N}\frac{\vec{\boldsymbol{g}}_i \cdot \vec{\boldsymbol{h}}_k}{h_k^{Tx}}(P_k^{Tx}(t) - P_{DC}) + \vec{\boldsymbol{g}}_i \cdot \vec{\boldsymbol{n}}(t) \qquad \text{Eq.13}$$

By inspecting Eq.13, it is easy to see that the optical power thus plays the same role, to a multiplication factor, as the electrical-signal amplitude in the RF system. The exact relationship between the channel-quality figure-of-merit and signal power for MIMO-OWC is discussed later in Chapter III.

As illustrations of the OWC link-budget issues, calculations are performed for a single-input single-output (SISO) system with random input and additive white Gaussian noise (AWGN) with power spectral-density N_0. Rewriting Eq.13 for the SISO case yields:

$$x''(t) = \frac{1}{h_{SISO}^{Tx}}(P^{Tx}(t) - P_{DC}) + \frac{1}{h_{SISO}^{Tx}h_{SISO}^{Rx}h_{SISO}^{chan}}n(t) \qquad \text{Eq.14}$$

With a Personick's factor k and a symbol rate R_s, the Signal-to-Noise Ratio (SNR) for this SISO channel [13] can be shown to be:

$$SNR_{SISO} = \frac{\left(h_{SISO}^{Rx} h_{SISO}^{chan}\right)^2}{k} \frac{\langle [P^{Tx}(t) - P_{DC}]^2 \rangle}{R_s N_0} \leq \frac{\left(h_{SISO}^{Rx} h_{SISO}^{chan}\right)^2}{k} \frac{\left[P_{\max}^{peak} - P_{DC}\right]^2}{R_s N_0} \quad \text{Eq.15}$$

The result in Eq.15 agrees with [12]. It also shows that for IM/DD OWC systems, the optical-power constraint $P_{\max}$ and path-loss h_{SISO}^{chan} both play a major role in system performance due to their square relationships with SNR. Thus, increasing received power in OWC is most effective to improve the link budget.

On the other hand, Eq.15 also shows that maintaining the same SNR (and consequently BER) whilst doubling the data rate requires a $\sqrt{2}$ increase of the received optical power. Thus received optical power is less important as a limiting factor in OWC than received electrical power is in RF systems.

B. MIMO detection and symbol detection

Chapter II.A has introduced a MIMO-OWC system model. This section, together with Chapter II.C and Chapter III, will form the theoretical analysis of the major components of that system model. In this chapter, detailed discussions on MIMO-detection methods will be presented: the chief focus will be on linear methods as they allow easy algebraic manipulations for theoretical studies on the optimisation rules for MIMO-OWC channels. Later, this chapter will discuss, in theoretical terms, some practical issues around symbol detection in MIMO systems, which will help the construction of the simulator in Chapter III.B.

1. MIMO detection

a. Overview

Chapter II has introduced Eq.6 which relates the M received signals $\vec{\boldsymbol{y}}(t)$ to the N transmitted signals $\vec{\boldsymbol{x}}(t)$ by means of a channel-matrix $\underline{\boldsymbol{H}}$. The next step in MIMO processing is to obtain estimates $\vec{\boldsymbol{x}}'(t)$ of the individual transmitted signals for further processing using SISO techniques (see **Error! Reference source not found.**.) This operation is known as 'MIMO detection' in the literature [82, 83].

Assuming bandwidths are greater than required for signal transmission, Eq.8 gives the recovered signal for the i^{th} channel:

$$x_i''(t) = (\vec{\boldsymbol{g}}_i \cdot \vec{\boldsymbol{h}}_i)x_i(t) + \sum_{k=1,k\neq i}^{N} (\vec{\boldsymbol{g}}_i \cdot \vec{\boldsymbol{h}}_k)x_k(t) + \vec{\boldsymbol{g}}_i \cdot \vec{\boldsymbol{n}}(t) \qquad \text{Eq.16}$$

($\vec{\boldsymbol{g}}_i$, $\vec{\boldsymbol{h}}_k$ are the i^{th} row of $\underline{\boldsymbol{G}}$ and k^{th} column of $\underline{\boldsymbol{H}}$, respectively)

Each row vector of the N-by-M MIMO-detector $\underline{\boldsymbol{G}}$ in Eq.16 recovers the signal stream of the corresponding channel whilst suppressing the interference from the other $(N-1)$

channels and the additive noise to a level required for reliable communications. To this end, there are several algorithms to construct $\underline{\boldsymbol{G}}$, broadly categorised as linear or nonlinear [82, 83]. Only the linear algorithms are studied in detail here, due to their simpler algebraic form for channel analysis, which will be crucial in formulating theoretical rules of channel-optimisation.

The linearity of the MIMO-detector $\underline{\boldsymbol{G}}$ means that the detecting operations of its N rows are independent from each other, *i.e.* one operation does not depend on the results of the others. Two widely-used linear methods are Zero-Forcing (ZF) and Minimum Mean-Square Error (MMSE) [82-84]. In both of these methods, the matrix $\underline{\boldsymbol{G}}$ is calculated entirely *a priori* without regards to the actual signal values transmitted.

b. Zero-Forcing

The ZF algorithm, also known as Inverse-Channel Detection [83], is perhaps the simplest MIMO-detection method. It focuses completely on suppressing the effects of cross-channel interference whilst recovering the desired signal to the original values, neglecting the presence of additive noise. From Eq.16, this means:

$$\begin{cases} \vec{\boldsymbol{g}}_i \cdot \vec{\boldsymbol{h}}_i = 1 \\ \vec{\boldsymbol{g}}_i \cdot \vec{\boldsymbol{h}}_k = 0 \ (\forall k \neq i) \end{cases} \text{ for } i = 1..N \qquad \text{Eq.17}$$

The well-known solution to Eq.17 is $\underline{\boldsymbol{G}} = \text{inverse}(\underline{\boldsymbol{H}})$. In MIMO systems, in order to be able to recover all transmitted signals, at least there must be no more Tx than Rx, *i.e.* $M \geq N$. The Moore-Penrose pseudo-inverse solution is then $\underline{\boldsymbol{G}} = \left(\underline{\boldsymbol{H}}^{\dagger} \times \underline{\boldsymbol{H}}\right)^{-1} \times \underline{\boldsymbol{H}}^{\dagger}$ ($\dagger$ denotes Hermitian transpose) [85]. The estimates now become:

$$\vec{\boldsymbol{x}}'(t) = \vec{\boldsymbol{x}}(t) + \underline{\boldsymbol{G}} \times \vec{\boldsymbol{n}}(t) = \vec{\boldsymbol{x}}(t) + \vec{\boldsymbol{n}}'(t) \qquad \text{Eq.18}$$

Eq.18 shows that the system has been completely parallelised (*i.e.* no interference) and thus is no different from that of N SISO channels. Assuming $E\left(\vec{\boldsymbol{n}}(t) \times \vec{\boldsymbol{n}}^{\dagger}(t)\right) = \sigma_n^2 \underline{\boldsymbol{I}}_M$, the altered noise added to the channel now has the covariance matrix:

$$E\left(\vec{\boldsymbol{n}}'(t) \times \vec{\boldsymbol{n}}'^{\dagger}(t)\right) = \sigma_n^2 \underline{\boldsymbol{G}} \times \underline{\boldsymbol{G}}^{\dagger} = \sigma_n^2 \left(\underline{\boldsymbol{H}}^{\dagger} \times \underline{\boldsymbol{H}}\right)^{-1} \qquad \text{Eq.19}$$

However, if the channel matrix $\underline{\boldsymbol{H}}$ is ill-conditioned (see Chapter III), the ZF solution is severely compromised on two accounts: the computational difficulty in calculating precise values for $\underline{\boldsymbol{G}}$, and the large amplification of noise power as can be seen in Eq.19. Therefore, ZF as the MIMO-detection algorithm is only used in relatively well-conditioned systems.

c. Minimum Mean-Square Error

Unlike the ZF solution, the MMSE algorithm tries to contain both the interference and the additive noise simultaneously, according to the minimum mean-square error criterion:

$$\underline{\boldsymbol{G}} = \arg\min_{\underline{\boldsymbol{G}}} E\left(\left[\vec{\boldsymbol{x}}(t) - \underline{\boldsymbol{G}} \times \vec{\boldsymbol{y}}(t)\right] \times \left[\vec{\boldsymbol{x}}(t) - \underline{\boldsymbol{G}} \times \vec{\boldsymbol{y}}(t)\right]^{\dagger}\right) \qquad \text{Eq.20}$$

If all N transmitted signals have the same power σ_x^2, and all M additive noise components also have the same power σ_n^2, the solution to Eq.20 is well-known [82, 83] ([86] for derivations):

$$\underline{\boldsymbol{G}} = \left(\underline{\boldsymbol{H}}^{\dagger} \times \underline{\boldsymbol{H}} + \frac{\sigma_n^2}{\sigma_x^2} \underline{\boldsymbol{I}}_N\right)^{-1} \times \underline{\boldsymbol{H}}^{\dagger} \qquad \text{Eq.21}$$

Alternatively, starting from the criterion in Eq.20, with $\underline{\boldsymbol{C}}_x = E\left(\vec{\boldsymbol{x}}(t) \times \vec{\boldsymbol{x}}^{\dagger}(t)\right)$ and $\underline{\boldsymbol{C}}_n = E\left(\boldsymbol{n}(t) \times \vec{\boldsymbol{n}}^{\dagger}(t)\right)$, it is possible to derive:

$$\underline{\boldsymbol{G}} = \underline{\boldsymbol{C}}_x \times \underline{\boldsymbol{H}}^{\dagger} \times \left(\underline{\boldsymbol{H}} \times \underline{\boldsymbol{C}}_x \times \underline{\boldsymbol{H}}^{\dagger} + \underline{\boldsymbol{C}}_n\right)^{-1} \qquad \text{Eq.22}$$

When $\underline{\boldsymbol{C}}_x = \sigma_x^2 \underline{\boldsymbol{I}}_N$ and $\underline{\boldsymbol{C}}_n = \sigma_n^2 \underline{\boldsymbol{I}}_M$, using singular-value decomposition on $\underline{\boldsymbol{H}}$, the two MMSE solutions as given by Eq.21 and Eq.22 can be shown to agree completely and thus be used interchangeably. Nonetheless, the form given in Eq.22 is able to accommodate a far broader range of MIMO systems, since neither of the transmit powers or the noise powers have to be all equal nor independent as implied in Eq.21. Hence, $\underline{\boldsymbol{G}}$ given by Eq.22 can be considered the generalisation of the well-known solution cited in literature. This form of the MIMO-detector is implemented for MMSE in the simulator described in Chapter II.

In practical systems where transmitted streams are all independent of each other and the additive noise is also independent ($\underline{\boldsymbol{C}}_x$ and $\underline{\boldsymbol{C}}_n$ are both diagonal,) the general Eq.22 can be reduced to Eq.21. Neglecting DC components, Eq.6 can be rewritten as:

$$\vec{\boldsymbol{y}}(t) = \underline{\boldsymbol{H}} \times \vec{\boldsymbol{x}}(t) + \vec{\boldsymbol{n}}(t) = \underline{\boldsymbol{H}} \times \left(\frac{1}{\overline{\sigma_x^2}} \underline{\boldsymbol{C}}_x^{\frac{1}{2}} \times \vec{\boldsymbol{\xi}}(t) \right) + \left(\frac{1}{\overline{\sigma_n^2}} \underline{\boldsymbol{C}}_n^{\frac{1}{2}} \times \vec{\boldsymbol{\eta}}(t) \right) \qquad \text{Eq.23}$$

$$\Leftrightarrow \overline{\sigma_n^2} \underline{\boldsymbol{C}}_n^{-\frac{1}{2}} \times \vec{\boldsymbol{y}}(t) = \frac{\overline{\sigma_n^2}}{\overline{\sigma_x^2}} \left(\underline{\boldsymbol{C}}_n^{-\frac{1}{2}} \times \underline{\boldsymbol{H}} \times \underline{\boldsymbol{C}}_x^{\frac{1}{2}} \right) \times \vec{\boldsymbol{\xi}}(t) + \vec{\boldsymbol{\eta}}(t) = \underline{\boldsymbol{H}}' \times \vec{\boldsymbol{\xi}}(t) + \vec{\boldsymbol{\eta}}(t) \qquad \text{Eq.24}$$

Because $E\left(\vec{\boldsymbol{\eta}}(t) \times \vec{\boldsymbol{\eta}}^{\dagger}(t)\right) = \overline{\sigma_n^2} \underline{\boldsymbol{I}}_M$ and $E\left(\vec{\boldsymbol{\xi}}(t) \times \boldsymbol{\xi}^{\dagger}(t)\right) = \overline{\sigma_x^2} \underline{\boldsymbol{I}}_N$, the MMSE MIMO-detector for the modified system in Eq.24 has the same form as expressed in Eq.21:

$$\underline{\boldsymbol{G}}' = \underline{\boldsymbol{H}}'^{\dagger} \times \left(\underline{\boldsymbol{H}}' \times \underline{\boldsymbol{H}}'^{\dagger} + \frac{\overline{\sigma_n^2}}{\overline{\sigma_x^2}} \underline{\boldsymbol{I}}_M \right)^{-1} = \left(\underline{\boldsymbol{H}}'^{\dagger} \times \underline{\boldsymbol{H}}' + \frac{\overline{\sigma_n^2}}{\overline{\sigma_x^2}} \underline{\boldsymbol{I}}_N \right)^{-1} \times \underline{\boldsymbol{H}}'^{\dagger} \qquad \text{Eq.25}$$

By comparing Eq.25 and the ZF solution, it can be seen that for the noiseless system, the MMSE solution reduces to that obtained with ZF. Furthermore, due to the presence of the additive identity matrix, the matrix inversion performed in MMSE is more stable for ill-conditioned channels. In Chapter III, it will be shown that the MMSE solution has another

advantage over ZF in that the effective noise power is not much amplified even when the channel matrix is ill-conditioned. Results from computer simulations also favour MMSE, as it offers SNR improvements of several dB compared with ZF [82, 83]. These advantages make MMSE the linear detection method of choice in this research.

d. Availability of channel-state information: CSIR and CSIT

The above discussions on the construction of the MIMO detector $\underline{\boldsymbol{G}}$ have been based on the assumption that the channel-state information (CSI) including $\underline{\boldsymbol{H}}$, is only available at the Rx (CSIR.) If the channel-state information is also available at the Tx (CSIT) then the transmitted signals $\vec{\boldsymbol{x}}(t)$ can be pre-processed to improve the Rx-side processing performance.

The simplest CSIT pre-processing technique is based on the singular-value decomposition (SVD) of the channel matrix $\underline{\boldsymbol{H}} = \underline{\boldsymbol{U}} \times \underline{\boldsymbol{S}} \times \underline{\boldsymbol{V}}^{\dagger}$, with unitary matrices $\underline{\boldsymbol{U}}$ and $\underline{\boldsymbol{V}}$, and *M*-by-*N* diagonal matrix $\underline{\boldsymbol{S}}$. Instead of the original vector $\vec{\boldsymbol{x}}(t)$ of encoded symbols, if the actual transmitted vector is $\vec{\boldsymbol{\xi}}(t) = \underline{\boldsymbol{V}} \times \vec{\boldsymbol{x}}(t)$ and if the received vector $\vec{\boldsymbol{y}}(t)$ is pre-multiplied with $\underline{\boldsymbol{U}}^{\dagger}$ to give $\vec{\boldsymbol{z}}(t)$, then the system equation becomes:

$$\vec{\boldsymbol{z}}(t) = \underline{\boldsymbol{U}}^{\dagger} \times \underline{\boldsymbol{H}} \times \vec{\boldsymbol{\xi}}(t) + \underline{\boldsymbol{U}}^{\dagger} \times \vec{\boldsymbol{n}}(t) = \underline{\boldsymbol{S}} \times \vec{\boldsymbol{x}}(t) + \underline{\boldsymbol{U}}^{\dagger} \times \vec{\boldsymbol{n}}(t) \qquad \text{Eq.26}$$

Eq.26 is effectively a parallel system of *N* SISO channels. Assuming identical and independent additive noise, the noise covariance in this parallel system is:

$$E\left(\underline{\boldsymbol{U}}^{\dagger} \times \vec{\boldsymbol{n}}(t) \times \vec{\boldsymbol{n}}^{\dagger}(t) \times \underline{\boldsymbol{U}}\right) = \underline{\boldsymbol{U}}^{\dagger} \times E\left(\vec{\boldsymbol{n}}(t) \times \vec{\boldsymbol{n}}^{\dagger}(t)\right) \times \underline{\boldsymbol{U}} = \overline{\sigma_n^2}\,\underline{\boldsymbol{I}}_M \qquad \text{Eq.27}$$

This is the same as the noise covariance before the pre-multiplication with $\underline{\boldsymbol{U}}^{\dagger}$. Therefore, the CSIT use of SVD has parallelised the system without any noise penalty. However, when $\underline{\boldsymbol{H}}$ is ill-conditioned, some elements on the main diagonal of $\underline{\boldsymbol{S}}$ are 0 or sufficiently small to make the corresponding parallel channels practically unusable.

To deal with ill-conditioned channel-matrices, another CSIT technique named Lattice-Reduction (LR) was introduced recently [83, 87-89]. The actual transmitted vector $\vec{\boldsymbol{\xi}}(t)$ is transformed from the original encoded-symbol vector $\vec{\boldsymbol{x}}(t)$ by an $\underline{\boldsymbol{H}}$-dependent matrix $\underline{\boldsymbol{P}}$ so that $\vec{\boldsymbol{x}}(t)$ and $\vec{\boldsymbol{\xi}}(t)$ both belong to the same symbol-constellation, but the basis vectors for $\vec{\boldsymbol{\xi}}(t)$ are more orthogonal than those for $\vec{\boldsymbol{x}}(t)$. The system equation becomes:

$$\vec{\boldsymbol{y}}(t) = \left(\underline{\boldsymbol{H}} \times \underline{\boldsymbol{P}}^{-1}\right) \times \left(\underline{\boldsymbol{P}} \times \vec{\boldsymbol{x}}(t)\right) + \vec{\boldsymbol{n}}(t) = \underline{\boldsymbol{H}}' \times \vec{\boldsymbol{\xi}}(t) + \vec{\boldsymbol{n}}(t) \qquad \text{Eq.28}$$

MIMO detection is then applied to the vector $\vec{\boldsymbol{y}}(t)$ to approximate $\vec{\boldsymbol{\xi}}(t)$ which is in turn transformed by $\underline{\boldsymbol{P}}^{-1}$ to give estimates of $\vec{\boldsymbol{x}}(t)$. Overall, this results in a variety of hybrid MIMO-detection techniques such as LR-ZF, LR-MMSE and LR-VBLAST. Analyses show that by using LR pre-processing, the system performance can improve by as much as 17 dB in SNR [83, 87]. This promising result demonstrates the benefits of CSIT, especially in problems which with CSIR are generally considered unsolvable without significant penalty such as ill-conditioned channel-matrices.

However, three problems remain before benefits of MIMO-OWC CSIT can be seen: (1) Accuracy of channel-state estimation; (2) Effects of channel-state estimation error on performance of CSIT techniques; (3) Reliable and economical OWC path to exchange CSI between Rx and Tx. Studies have been undertaken in each of these areas and a number of solutions have been recently proposed, though none has been universally adopted. For simplicity, this research is thus solely concerned with CSIR scenarios. Channel estimation will be discussed in Chapter II.C, whilst readers are referred to [90-93] and [34] for work in the problems (2) and (3) respectively.

2. Effects of MIMO detection on symbol detection

In this section, the effect of the MIMO detection on symbol detection is presented. The discussion firstly focuses on whether the post-processing on the Rx side has to be implemented in specific ways to benefit from the MIMO detection. Secondly, it shows how the MIMO detection affects the symbol detection of the different modulation schemes.

a. Order of the signal processing operations

In a typical SISO system, the symbol mapping and decision making are the last stages in the signal-processing chain [13]. However, the order of these operations in MIMO processing is a matter of some interest, since the MIMO detection generally distorts the noise so it no longer fits the AWGN model usually assumed in symbol detectors. This distortion can be seen in Eq.16, where the random noise after MIMO detection becomes $\vec{\boldsymbol{n}}'(t) = \underline{\boldsymbol{G}} \times \vec{\boldsymbol{n}}(t)$ and its covariance matrix is $E\left(\vec{\boldsymbol{n}}'(t) \times \vec{\boldsymbol{n}}'^{\dagger}(t)\right) = \sigma_n^2 \underline{\boldsymbol{G}} \times \underline{\boldsymbol{G}}^{\dagger}$. This matrix is generally not diagonal, as that of independent AWGN.

Performing the symbol detection before the MIMO detection has the advantage that the noise in the signals to be detected behaves as expected when a commonplace maximum-likelihood (ML) detector is used (see [13]). The value to be detected in each Rx channel is:

$$y_j'(t) = \sum_{i=1}^{N} h_{ji} h_j^{Rx}(t) * h_i^{Tx}(t) * (x_i(t) + x_{DC}) \qquad \text{Eq.29}$$

In an *M*-by-*N* system, with the transmitted-symbol alphabet of L symbols, the size of the alphabet of the symbol $y_j'(t)$ is thus L^N at maximum. This means that for each Rx channel, the AWGN-ML detector would have to search and compare metrics over a constellation of at most L^N symbols [13]. For larger values of L and especially of N (due to its being the exponent), this detection can be very slow and ineffective. Therefore the signals are usually

MIMO-detected before symbol-detected, since this order allows reasonable processing-time in exchange for some degradation in performance of AWGN-ML detectors.

However, if orthogonal frequency-division multiplexing (OFDM) is used in the MIMO system, it can be shown that performing a Fast-Fourier Transform (FFT) (see [13]) on each Rx channel before MIMO detection is advantageous. This ordering is able to contain the errors of symbol-detection, which is done after MIMO detection as discussed. The prerequisites for the success of this ordering are perfect knowledge of propagation delays, and sufficiently broad system-bandwidths for each OFDM sub-carrier.

b. The effects of modulation schemes on MIMO detection

ZF- and MMSE-based detectors perform differently depending on the modulation schemes used. Eq.16 shows the MIMO-detected signal of the i^{th} channel consists of two parts:

$$x_i''(t) = \underbrace{(\vec{\boldsymbol{g}}_i \cdot \vec{\boldsymbol{h}}_i)x_i(t)}_{desired} + \underbrace{\sum_{k=1,k\neq i}^{N} (\vec{\boldsymbol{g}}_i \cdot \vec{\boldsymbol{h}}_k)x_k(t) + \vec{\boldsymbol{g}}_i \cdot \vec{\boldsymbol{n}}(t)}_{undesired} \qquad \text{Eq.30}$$

For the same SNR, the AWGN-ML symbol detector works most efficiently when the undesired component is AWGN [13]. However, it can be seen from Eq.30 that the undesired component of the signal is not necessarily AWGN: $\vec{\boldsymbol{g}}_i \cdot \vec{\boldsymbol{n}}(t)$ is a sum of Gaussian components so it is Gaussian; but $(\vec{\boldsymbol{g}}_i \cdot \vec{\boldsymbol{h}}_k)x_k(t)$ and their sum[†] are not necessarily so.

If the MIMO detection is ZF-based, $\vec{\boldsymbol{g}}_i \cdot \vec{\boldsymbol{h}}_k = 0 \ \ \forall k \neq i$ and Eq.30 reduces to $\vec{\boldsymbol{g}}_i \cdot \vec{\boldsymbol{n}}(t)$. Thus the undesired component is AWGN, regardless of the pulse-shape of $x_k(t)$. This result shows that ZF-based MIMO detection can be used for all modulation schemes without any degradation in symbol-detection performance of the AWGN-ML detector.

[†] When N is large, the Central-Limit Theorem dictates the sum $\Sigma(\vec{\boldsymbol{g}}_i \cdot \vec{\boldsymbol{h}}_k)x_k(t)$ as approximately Gaussian.

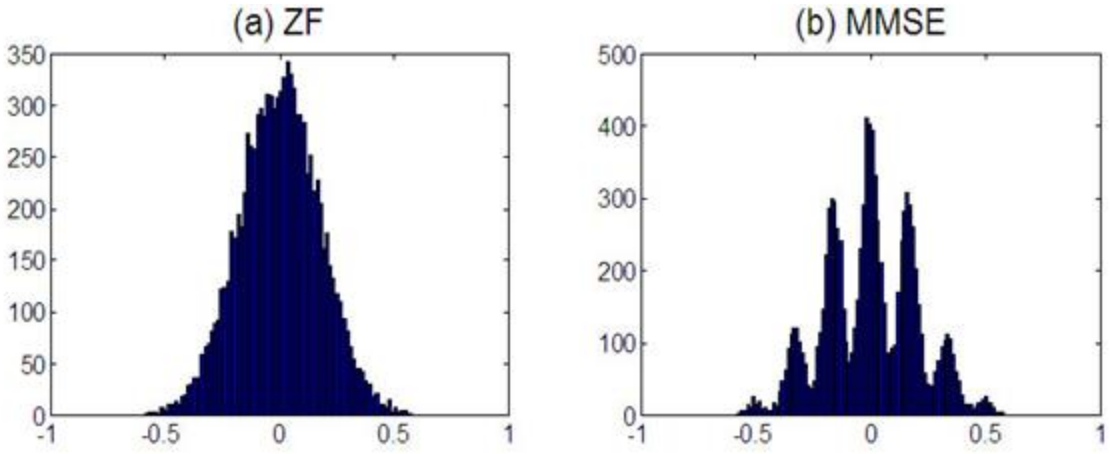

Figure 6. Amplitude histogram for the same channel with two recovery algorithms

With MMSE-based MIMO detection, $\underline{\boldsymbol{G}} = \left(\underline{\boldsymbol{H}}^{\dagger} \times \underline{\boldsymbol{H}} + (\sigma_n^2/\sigma_x^2)\underline{\boldsymbol{I}}_N\right)^{-1} \times \underline{\boldsymbol{H}}^{\dagger}$ thus $\vec{\boldsymbol{g}}_i \cdot \vec{\boldsymbol{h}}_k \neq 0 \;\; \forall k \neq i$. Hence the pulse-shape of $x_k(t)$ plays a role in determining whether the undesired signal component is AWGN. Figure 6 shows the histograms of signal amplitude for channel 2 in a 6-Tx 20-Rx MIMO system, using NRZ-OOK as the channel modulation (about a central DC level) and MIMO-detected with ZF and MMSE respectively (*cf*. Chapter III.) It can be seen that the signal obtained with the MMSE algorithm is not AWGN-interfered, leading to the performance degradation in the ML-detection.

A solution to this degradation is when $\sigma_n^2 \ll \sigma_x^2$. Then $\underline{\boldsymbol{G}}^{MMSE} \cong \underline{\boldsymbol{G}}^{ZF}$ and the effect of the $x_k(t)$ pulse-shape diminishes, giving MMSE-based algorithms the same ML-detection performance as the ZF-based ones. Another solution is when $x_k(t)$ is OFDM-modulated, then the multiple modulated sub-carriers would make the pulse-shape of $x_k(t)$ approach AWGN. The undesired component would therefore also approach AWGN, and the degradation in ML-detection performance with MMSE-based algorithms would in turn approach zero.

C. Modelling of the channel matrix

To investigate the MIMO-OWC channel properties, for optimisation studies, a theoretical model of the channel matrix is required. In this chapter, an analytical model for a MIMO-OWC general channel-matrix is discussed, together with an approximation model for an imaging channel-matrix. The last part of this chapter discusses the estimation of $\underline{\boldsymbol{H}}$ and estimation errors, introducing an estimation algorithm.

1. An analytical model of general MIMO-OWC channel matrix

A theoretical model for the channel matrix is necessary for analytical studies of the relationship between the MIMO-OWC performance and $\underline{\boldsymbol{H}}$. Eq.4 in Chapter II gives the full MIMO-OWC relationship. With perfect signal equalisation, it can be re-written:

$$\vec{\boldsymbol{y}}(t) = \underline{\boldsymbol{H}}(t) \otimes \left(\vec{\boldsymbol{x}}(t) + \vec{\boldsymbol{x}}_{\boldsymbol{DC}}(t)\right) + \vec{\boldsymbol{n}}(t) \qquad \text{Eq.31}$$

The elements $h_{ji}(t)$ of the M-by-N matrix $\underline{\boldsymbol{H}}(t)$ are the optical transfer function of the sub-channel between the i^{th} Tx and j^{th} Rx as shown in Eq.2. Since this IM/DD-based OWC system is partially coherent [12], the optical transfer function $h_{ji}(t)$ is effectively the intensity impulse response and thus is non-negative [76]. And because fading is negligible [12], $h_{ji}(t)$ is time-invariant.

According to [77], the optical transfer function $h_{ji}(t)$ can be decomposed into a LoS component and diffuse components. The LoS component is essentially an impulse function delayed by some propagation time τ_{ji}, and thus takes the form $h_{ji}^{LoS}\,\delta\left(t - \tau_{ji}\right)$. For an imaging Rx system as shown in Figure 7a, the constant h_{ji}^{LoS} represents the LoS fraction of the transmitted optical power arriving at the imaging lens. For the non-imaging Rx in Figure 7b,

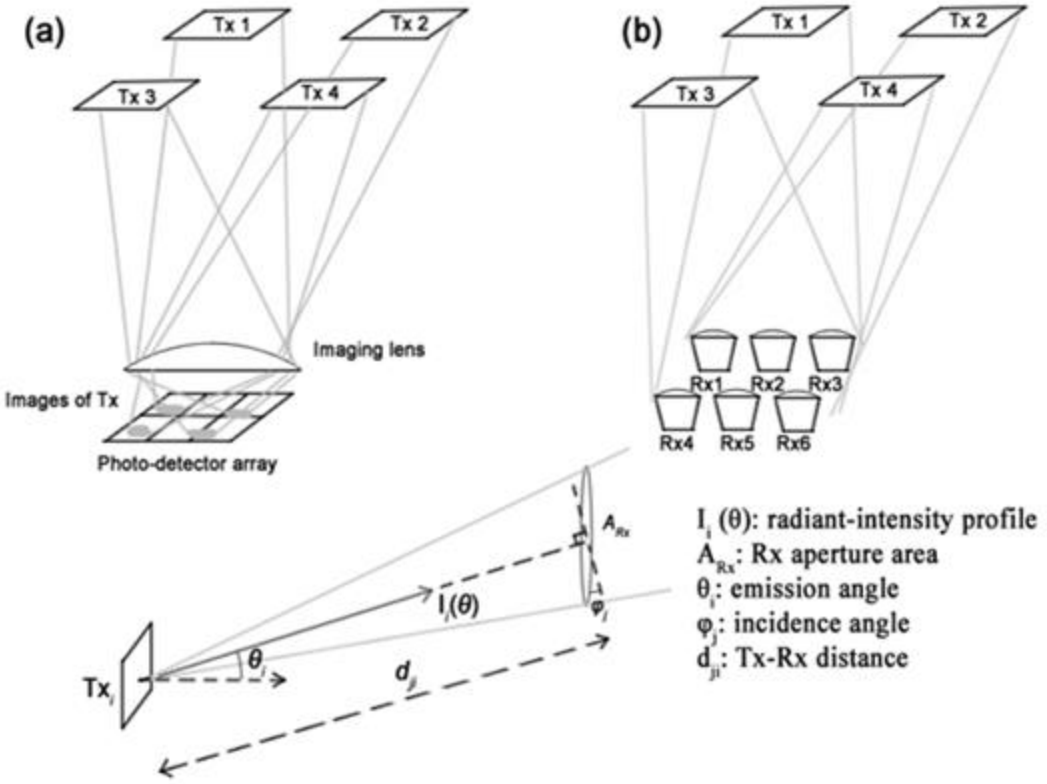

Figure 7. Geometries (not to scale) of 4-Tx 6-Rx channels: (a) Imaging; (b) Non-imaging; (c) Propagation path between the i^{th} Tx and the Rx aperture

h_{ji}^{LoS} represents the LoS fraction of the transmitted optical power directly collected by each photo-detector.

Figure 7a shows the geometry of the imaging channel, where light from each Tx arrives at the imaging lens and is directed by the lens to form a distinct image whose optical power is collected by the photo-detectors on which the image is incident. Figure 7b shows the non-imaging channel where light from all Tx arrives at the lens of each Rx element and is all collected as optical input for this Rx element. Figure 7c shows the propagation from the i^{th} Tx to the Rx aperture: imaging lens (for the imaging case) and j^{th} Rx element (for non-imaging.)

For imaging Rx collection-systems, h_{ji}^{LoS} can be factored as: $h_{ji}^{LoS} = h_i^{Rx\_lens} h_{ji}^{det}$. The constant $h_i^{Rx\_lens}$ is the fraction of the transmitted optical power from the i^{th} Tx arriving at the

front of the whole Rx collection-system. And h_{ji}^{det} represents the fraction of the Tx image 'steered' by the lens onto and therefore collected by the j^{th} photo-detector.

With γ denoting the photo-detector conversion factor, if the Rx subtends a small angle at the Tx, the inverse-square law gives:

$$h_{ji}^{LoS} = \gamma \frac{A_{Rx,j} \cos \varphi_{ji}}{d_{ji}^2} I_i(\theta_i) \qquad \text{Eq.32}$$

$$h_i^{Rx\_lens} = \gamma \frac{A_{Rx} \cos \varphi_i}{d_{Rx,i}^2} I_i(\theta_i) \qquad \text{Eq.33}$$

For extended-source systems (*i.e.* Rx subtending significant angles at Tx) the formulation is far more complex, and is outside the modelling scope of this research. Thus for more specific channel matrices with extended sources, ray-tracing simulation using ZEMAX is conducted.

The diffuse component represents the fraction of the transmitted optical power that arrives at the Rx after at least one reflection. In normal (homogeneous) environments, Fermat's principle dictates that this diffuse impulse-response cannot arrive before the LoS component [75]. The diffuse component can thus be written as $\eta_{ji}^{diff}(t - \tau_{ji})$. A model is proposed in [77] for the diffuse component, with the frequency-response of $\eta_{ji}^{diff}(t)$ as:

$$N_{ji}^{diff}(\omega) = \gamma \frac{A_{Rx}}{A_{room}} \frac{\rho_1}{1 - \langle \rho \rangle} \frac{1}{1 - j\omega \dfrac{\ln\langle \rho \rangle}{\langle t_{arrival}^{diff} \rangle}} \qquad \text{Eq.34}$$

Where: A denotes the area, ρ denotes the reflectivity coefficient, and $\langle \cdot \rangle$ the area-weighted averages.

Results in [77] show that the 3dB-bandwidth of the diffuse-only link is about 5MHz in diffusive environments. However, since A_{room} in Eq.34 is often at least 4π times larger than $d_{Rx,i}^2$ (or d_{ji}^2) in Eq.32, for $\rho \cong 0.75 - 0.8$ the LoS received power is about 2.5–4 times

stronger than the diffuse one, which agrees with [77]. The link thus can be shown to effectively have very broad 3dB-bandwidth. This leads to the approximation of the impulse response $h_{ji}(t)$ with a single impulse, which in turn can be approximated with that of the LoS link only.

For indoor systems, the differences in Tx-Rx propagation paths are typically small enough (~centimetres, compared with radiation free-space speed of $3 \cdot 10^8$ m/s) so that all τ_{ji} can be considered equal and neglected in analysis. Thus, the convolutional channel-matrix $\underline{\boldsymbol{H}}(t)$ in Eq.31 becomes the multiplicative $\underline{\boldsymbol{H}}$ in Eq.6.

For the non-image case, the elements of the multiplicative $\underline{\boldsymbol{H}}$ are given by:

$$h_{ji} = h_{ji}^{LoS} = \gamma \frac{A_{Rx,j} \cos \varphi_{ji}}{d_{ji}^2} I_i(\theta_i) \qquad \text{Eq.35}$$

From Eq.35, the elements h_{ji} for the non-imaging case are relatively straightforward to evaluate analytically. However, for the compact Tx and Rx in this research, d_{ji}^2 (and $\cos \varphi_j$) in the non-imaging Eq.35 are similar for all i and j. With identical $I_i(\theta)$ and $A_{Rx,j}$, the non-imaging $\underline{\boldsymbol{H}}$ is thus fairly uniform across rows and columns. Chapter III will show that this form of $\underline{\boldsymbol{H}}$ is undesirable, empirically verified in [33].

For the imaging case, the elements of the multiplicative $\underline{\boldsymbol{H}}$ in Eq.6 are given by:

$$h_{ji} = h_{ji}^{LoS} = \gamma h_{ji}^{det} \frac{A_{Rx} \cos \varphi_i}{d_{Rx,i}^2} I_i(\theta_i) \qquad \text{Eq.36}$$

The calculation of h_{ji} in Eq.36 involves the factors h_{ji}^{det} whose exact values can only be evaluated empirically (or by using the ray-tracing package ZEMAX). To help the theoretical studies of the imaging $\underline{\boldsymbol{H}}$, an analytical approximation is introduced to help the calculation of h_{ji}^{det}, and thus h_{ji} for the imaging case.

2. A hybrid geometric-optic model for the imaging-MIMO channel matrix

The model construction is divided into two stages. The first uses paraxial geometric-optics in two dimensions (2D) to approximate the size of the Tx image projected onto the Rx plane. The second then fits this image into a Gaussian intensity profile to facilitate the calculation of h_{ji}^{det} for the full three-dimensional (3D) system.

a. Two-dimensional model of an imaging MIMO system

Figure 8 shows the meridional plane of an imaging system consisting of a point source at position (r, z), a thin convex lens with focal length f_0 and radius R positioned at the origin, and an imaging screen parallel to and separated from the lens by a distance f which is variable for different levels of image defocusing. In this analysis, all rays between the source and the lens are assumed to be paraxial.

The thin lens formula [75] and elementary geometry on the similar triangles in Figure 8 give, for the defocused image of a point source at position (r, z), the meridional diameter d

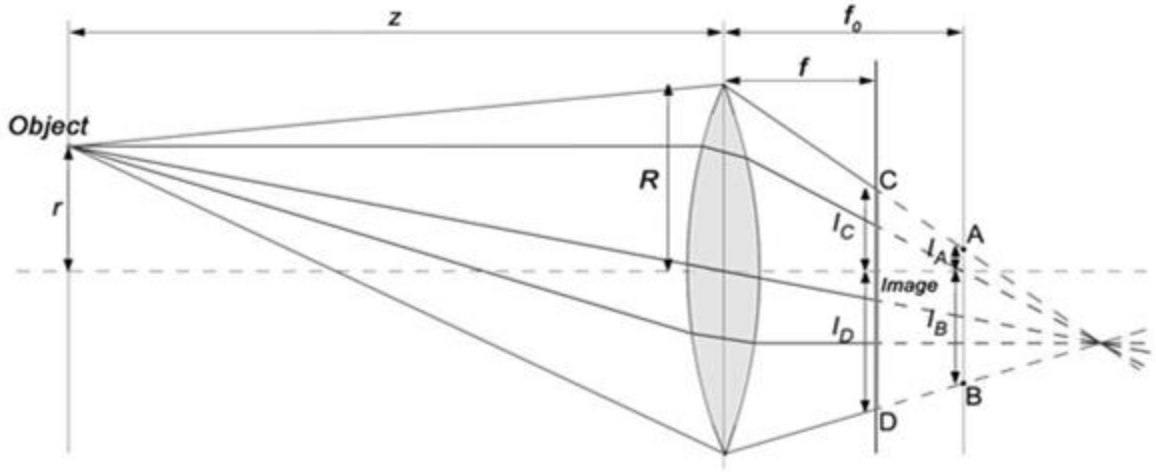

Figure 8. Schematic of the meridional plane of a 2D single-lens, defocused system

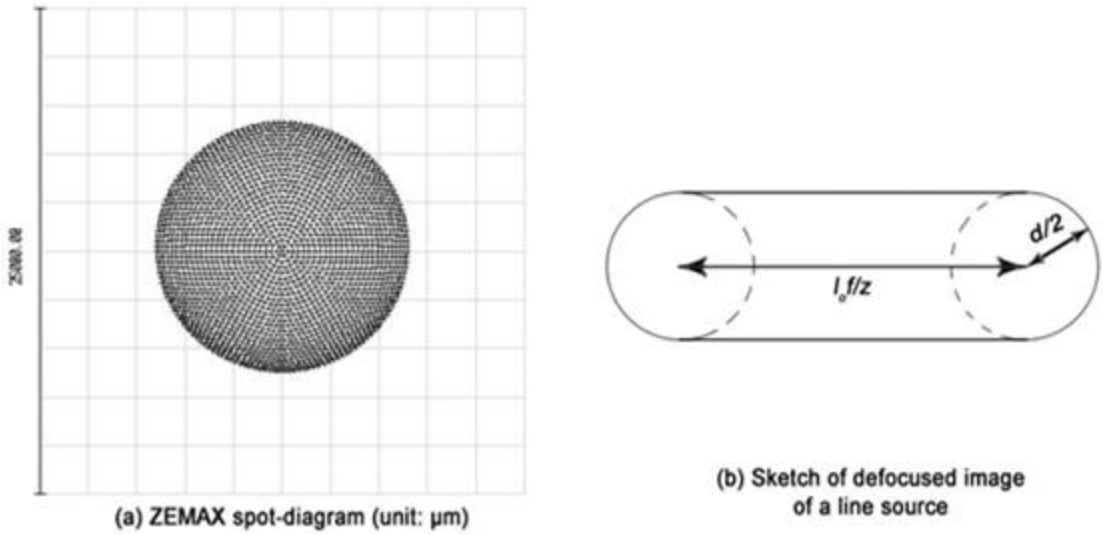

Figure 9. Defocused images of (a) an off-axis point-source, and (b) a line source

(line CD in Figure 8) and the distance r_i^{centre} of the image centre from the optical axis as:

$$\begin{cases} l_C = (l_A - R)\dfrac{f}{f_0} + R = f\dfrac{R-r}{z} + R\dfrac{f_0 - f}{f_0} \\ l_D = (l_B - R)\dfrac{f}{f_0} + R = f\dfrac{R+r}{z} + R\dfrac{f_0 - f}{f_0} \end{cases}$$

Eq.37

$$\Leftrightarrow \begin{cases} d = l_C + l_D = 2R\left(\dfrac{f}{z} + \dfrac{f_0 - f}{f_0}\right) \\ r_i^{centre} = \dfrac{l_C - l_D}{2} = -\dfrac{f}{z}r \end{cases}$$

Ray-tracing using ZEMAX® for the imaging of a point source shows that the defocused image is approximately a circular disc (see Figure 9.) Hence the extent of this defocused image can be described as a circle centred at r_i^{centre} and with radius $d/2$. The maximum extent of the defocused image of a line source of length l_0 (see Figure 9) can therefore be given by:

$$l_i = l_0\frac{f}{z} + 2R\left(\frac{f}{z} + \frac{f_0 - f}{f_0}\right) \qquad \text{Eq.38}$$

b. Three-dimensional model of imaging MIMO system

The Tx system consists of N planar light sources, all of which lie in a plane parallel to the plane of the imaging lens. Each Tx is a square Lambertian source of order m and of side-length w_{Tx}. The Rx system consists of an imaging thin lens of radius R and focal length f_0, and a set of M rectangular photo-detectors tiling closely to form a regular plane grid. The distance between the thin lens and the photo-detector plane is f. The Tx system is rotated about the longitudinal z-axis by ψ, relative to the Rx system.

The set (x_i, y_i, z_i) denotes the position of the centre of the i^{th} Tx relative to that of the imaging lens. The following components of h_{ji}^{LoS} in Eq.35 can be calculated:

$$d_{Rx,j} = (x_i^2 + y_i^2 + z_i^2)^{\frac{1}{2}} \text{ and } \cos\varphi_i = z_i(x_i^2 + y_i^2 + z_i^2)^{-\frac{1}{2}}$$
$$I_i(\theta_i) = I_i(\varphi_i) = \frac{(m+1)}{2\pi}\frac{z_i^m}{(x_i^2 + y_i^2 + z_i^2)^{\frac{m}{2}}} \qquad \text{Eq.39}$$

From Eq.37 and Eq.38, the centre (u_i, v_i) and side-length a of the Tx-image are:

$$a = \frac{f}{z_i}(w_{Tx} + 2R) + 2R\frac{f_0 - f}{f_0}$$
$$u_i = -\frac{f}{z_i}x_i \text{ and } v_i = -\frac{f}{z_i}y_i \qquad \text{Eq.40}$$

To calculate h_{ji}^{det} as the integration of the intensity distribution, a continuous-function model of this distribution must be found whose 3dB-span is the same as the image side. Simulation (see Figure 10) shows that the image intensity-distribution of a square source, centred at $(0,0)$, with the 3dB-span (*i.e.* image side) a, can be modelled with 4 Gaussians:

$$I_{\xi\eta}(\xi,\eta) = \frac{9}{4\pi a^2}\sum_{q=1}^{2}\sum_{p=1}^{2}\exp\left(-\frac{9}{a^2}((\xi + (-1)^p a)^2 + (\eta + (-1)^q a)^2)\right) \qquad \text{Eq.41}$$

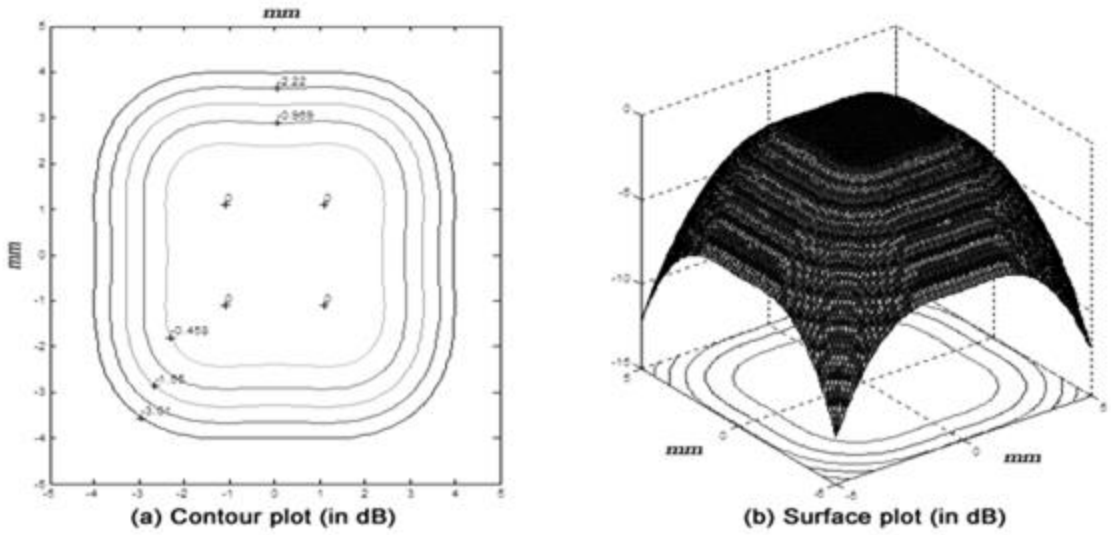

Figure 10. Simulated Tx-image intensity modelled by 4 Gaussians against $(\boldsymbol{\xi}, \boldsymbol{\eta})$

The coordinates (ξ, η) of the image's reference frame are related to the Rx's (x, y) by:

$$\xi = (x\cos\psi - y\sin\psi) - (u_i\cos\psi - v_i\sin\psi)$$
$$\eta = (x\sin\psi + y\cos\psi) - (u_i\sin\psi + v_i\cos\psi) \qquad \text{Eq.42}$$

Eq.42 is substituted into Eq.41 to obtain the intensity distribution $I_{uv}(x, y|u_i, v_i)$ of the i^{th} Tx-image, which is then integrated for each photo-detector to obtain h_{ji}^{det}. The integration of each Gaussian component of $I_{uv}(x, y|u_i, v_i)$ is of the following form:

$$\text{Integration} = \frac{1}{16}\begin{pmatrix}\left(\text{erf}\left(f_1(a, x_i, y_i, \psi, x_1)\right) - \text{erf}\left(f_2(a, x_i, y_i, \psi, x_2)\right)\right) \\ \left(\text{erf}\left(g_1(a, x_i, y_i, \psi, y_1)\right) - \text{erf}\left(g_2(a, x_i, y_i, \psi, y_2)\right)\right)\end{pmatrix} \qquad \text{Eq.43}$$

For the more general rectangular planar source, the integration in Eq.43 is intractable for generic ψ.

Substituting this h_{ji}^{det} into Eq.35, together with Eq.39 h_{ji} (and an analytical form of $\underline{\boldsymbol{H}}$) can be found. Using this model for each transmitter image, the overall channel matrix can be analytically formulated, which in turn gives insights into the positions the images must be moved to in order to improve the system performance.

3. Estimation of the MIMO-OWC channel matrix

a. Channel-estimation and estimation errors

From Chapter II.B, it can be seen that the channel-state information (CSI) must at least be known at the Rx for the MIMO detection to be viable. Although what CSI must be known is dependent on the algorithms in use, knowledge of the channel matrix is always required. Variations in $\underline{\boldsymbol{H}}$ come generally from changes in the channel geometry due to movement of terminals (see Eq.35.) The channel-estimation accuracy and its effect on the MIMO detection is thus an important issue.

Although both $\underline{\boldsymbol{H}}$ and $\underline{\boldsymbol{H}}_{est}$ as intensity responses are strictly non-negative [76], their difference $\underline{\boldsymbol{\Delta}} = \underline{\boldsymbol{H}} - \underline{\boldsymbol{H}}_{est}$ can be assumed able to take any real value such that $\delta_{ji} \leq h_{ji}$. The MIMO-detector $\underline{\boldsymbol{G}}$ is now calculated based on the estimate matrix $\underline{\boldsymbol{H}}_{est}$. The MIMO-detected i^{th} channel becomes:

$$x_i''(t) = \left(\vec{\boldsymbol{g}}_i \cdot \left(\vec{\boldsymbol{h}}_i^{est} + \vec{\boldsymbol{\delta}}_i\right)\right) x_i(t) + \sum_{k=1, k\neq i}^{N} \left(\vec{\boldsymbol{g}}_i \cdot \left(\vec{\boldsymbol{h}}_k^{est} + \vec{\boldsymbol{\delta}}_k\right)\right) x_k(t) + \vec{\boldsymbol{g}}_i \cdot \vec{\boldsymbol{n}}(t) \quad \text{Eq.44}$$

If a ZF-based algorithm is used, $\underline{\boldsymbol{C}}_e = \sigma_e^2 \underline{\boldsymbol{I}}_{M \cdot N}$, $\underline{\boldsymbol{C}}_x = \sigma_x^2 \underline{\boldsymbol{I}}_N$ and $\underline{\boldsymbol{C}}_n = \sigma_n^2 \underline{\boldsymbol{I}}_M$ then the recovery error $e(t) = x_i''(t) - x_i(t)$ and its variance are given by:

$$e_i(t) = \sum_{k=1}^{N} \left(\vec{\boldsymbol{g}}_i \cdot \vec{\boldsymbol{\delta}}_k\right) x_k(t) + \vec{\boldsymbol{g}}_i \cdot \vec{\boldsymbol{n}}(t)$$

$$\therefore E(|e_i(t)|^2) = \left(1 + N\sigma_e^2 \frac{\sigma_x^2}{\sigma_n^2}\right) \sigma_n^2 \left[\underline{\boldsymbol{G}} \times \underline{\boldsymbol{G}}^{\dagger}\right]_{ii} \quad \text{Eq.45}$$

Compared with the perfect case ($\sigma_e^2 = 0$), imperfect CSI increases the recovery-error variance by $N\sigma_e^2\frac{\sigma_x^2}{\sigma_n^2}$ times. Rewriting this proportion as:

$$\alpha = N\sigma_e^2\frac{\sigma_x^2}{\sigma_n^2} = N\frac{\sigma_e^2}{\max_j\left(h_{ji}^2\right)}\frac{\max\left(\sigma_{x\_rx}^2\right)}{\sigma_n^2} \qquad \text{Eq.46}$$

It can be seen from Eq.46 that the accuracy of the estimation algorithm must be smaller than $N\max\left(\sigma_{x\_rx}^2\right)/\sigma_n^2$ for the imperfect-CSI recovery-error not to be significantly larger than the error of the perfect-CSI case.

The frequency of CSI estimation is another interesting question. Continuous estimation for direct estimation of $\underline{\boldsymbol{H}}$ is discussed in [94] and for an indirect method via geometry measurements in [95]. Yet, geometrical changes are generally slow compared with symbol rates, making $\underline{\boldsymbol{H}}$ stable for long periods. Thus most estimates from these methods are redundant.

Infrequent estimation is less computationally wasteful and demanding since the estimation (see Chapter II.C.3.b) can be separated from the transmission. However, the question of when the estimate $\underline{\boldsymbol{H}}_{est}$ must be updated and based on what metrics still is an open question.

b. A simple estimation algorithm

For the simulations carried out in this research, a simple estimation algorithm based on calculating the variance of a training sequence is used. This algorithm estimates $\underline{\boldsymbol{H}}$ column-wise: only one Tx is enabled (all others are off) and the corresponding column of $\underline{\boldsymbol{H}}$ is estimated. Then this Tx is turned off, and the next one is enabled for the next iteration.

With a known noise power σ_n^2 and training sequence duration T, for the pair of the i^{th} Tx and the j^{th} Rx, the received signal $y_{ji}(t)$ can be expressed as:

$$y_{ji}(t) = h_{ji}x_i(t - \tau_{ji}) + n_j(t) \qquad \text{Eq.47}$$

To get a reasonable estimate of h_{ji}, the noise element in Eq.47 must be accounted for. As the instantaneous noise $n_j(t)$ cannot be measured but the noise power can, Eq.47 is manipulated as follows in order to express h_{ji} in terms of the measureable parameters

$$\therefore \sum_{t=0}^{T} y_{ji}^2(t) \cong h_{ji}^2 \sum_{t=0}^{T} x_i^2(t) + \sum_{t=0}^{T} n_j^2(t) + 2h_{ji} \sum_{t=0}^{T} x_i(t)n_j(t) \qquad \text{Eq.48}$$

$$\therefore \left(h_{ji}^{est}\right)^2 \cong \frac{\sum_{t=0}^{T} y_{ji}^2(t) - \sum_{t=0}^{T} n_j^2(t)}{\sum_{t=0}^{T} x_i^2(t)} \cong \frac{\sum_{t=0}^{T} y_{ji}^2(t) - \sigma_n^2 T}{\sum_{t=0}^{T} x_i^2(t)}$$

$$\because \sum_{t=0}^{T} x_i(t)n_j(t) \cong 0 \qquad \text{Eq.49}$$

The squaring in Eq.48 reflects that in IM/DD architecture, the power of the electrical output of the photo-detectors is proportional to the square of the optical intensity.

To avoid unrealistic values resulting from the two successive approximations in Eq.49 when h_{ji} is too small, an additional step is performed at the start: The maximum cross-correlation between $y_{ji}(t)$ and the known $x_i(t)$ is calculated and compared with the cross-correlation of $x_i(t)$ with AWGN noise. If the relative difference is under a threshold (0.6 is used as empirically determined from simulations), $y_{ji}(t)$ is considered noise and $h_{ji}^{est} = 0$.

The performance of this algorithm depends strongly on the assumption that bandwidth equalisation is perfect. To ensure the equalisation does not affect the estimation, a sinusoidal wave of a frequency in the system pass-bands can be used as the training sequence. This will allow the wave to retain its form during propagation and be only attenuated by the multiplicative h_{ji}. This training method is used in the experiment reported in [96].

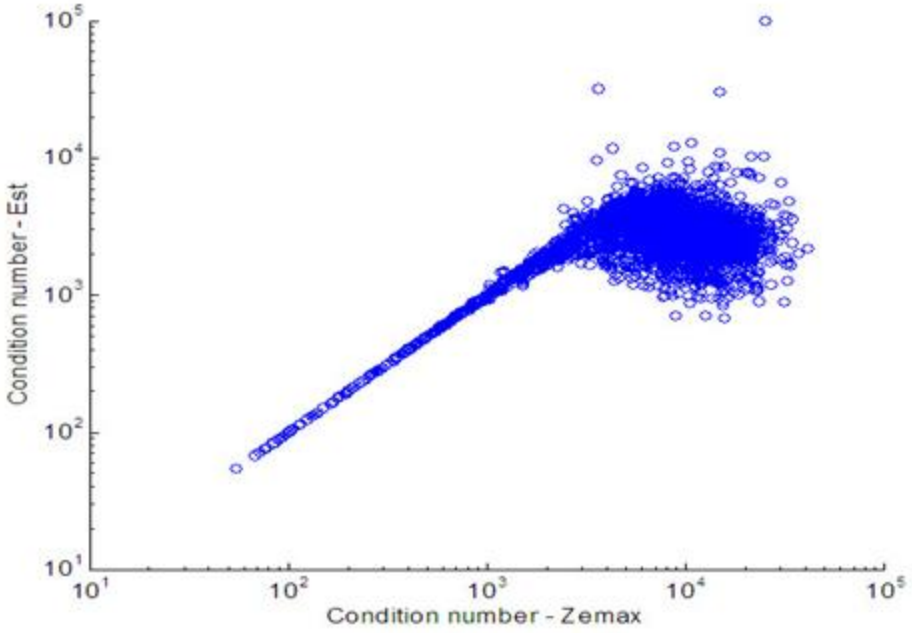

Figure 11. Condition number of the channel matrix versus that of its estimate

Figure 11 shows the pair-wise plot of the condition number[‡] of the channel matrix as obtained from ZEMAX and that of the matrix estimated with this algorithm (for simulation parameters listed, see Chapter III.B.2.c.) The 100-symbols long training sequence in the environment where $h_{ji} \cong 4 \cdot 10^{-6}$, $\sigma_x = 0.5$, $\sigma_n \cong 3 \cdot 10^{-8}$ and $N = 4$, gives the ratio α in Eq.46 the range between 0 and 0.08, with mean of $5.7 \cdot 10^{-5}$ and variance of $3.8 \cdot 10^{-6}$. With $\alpha \ll 1$, these results thus show that for the condition number up to 1000, this algorithm estimates the channel well.

[‡] The condition number is a popular figure of merit to succinctly describe, in a single number, the quality of a matrix for computation. In this diagram, as well as throughout this thesis, the definition based on norm 2 is used [97] L. N. Trefethen and D. Bau III, *Numerical linear algebra*. Philadelphia: SIAM, 1997..

D. Conclusion

This chapter presents an overview study of the several aspects of a MIMO-OWC system. Based on the link-budget calculations for the system, the optical-power constraint imposed by eye-safety regulations is considered as the most important limiting factor in single-channel communications, compared with other factors such as symbol rate or noise levels.

Several MIMO-detection methods are reported in Chapter II.B with MMSE found to be the preferred algorithm for implementation due to its robustness in high-overlap scenarios. Also, the effects of symbol detection on MIMO detection dictate that for the Rx processing, the detection should be performed after MIMO-detection. A corollary of this finding is that ZF-based detectors are more suitable for amplitude-keying modulation schemes, whilst MMSE would require modulation schemes where the signals are approximately white Gaussian noise such as OFDM.

As can be seen in the analyses in this chapter, the channel matrix $\underline{\boldsymbol{H}}$ must be known as input data for both the ZF and MMSE algorithms. Based on the model described in Chapter II.A of a line-of-sight MIMO-OWC system, Chapter II.C presents an analytical channel-matrix model for the MIMO systems, and introduces a simple deterministic estimation algorithm for $\underline{\boldsymbol{H}}$, which is judged to be effective according to a metric measuring estimation errors, also introduced in this chapter. This estimation algorithm will be used for system investigations in Chapter III.

To understand the relationship between the system geometry, Chapter III will study several metrics in simulation to assess their propriety in measuring the performance.

Chapter III. **Metrics for MIMO-OWC**

In order to understand the relationship between a particular geometry and the communication performance of the MIMO-OWC system built on it, this chapter will study how the channel matrix, as the embodiment of the system geometry, influences the overall performance, particularly the system Bit-Error-Rate (BER). Three metrics based solely on the channel matrix will be presented, namely the condition number, the Signal-to-Interference-and-Noise Ratio (SINR) and the SISO-equivalent Signal-to-Noise Ratio (SNR^{SISO}). A MATLAB program for MIMO-OWC will also be introduced as a platform to assess the accuracy of the proposed metrics in predicting the system performance, by conducting simulated transmission and correlating the BER with each of the metrics.

A. Modulation-independent metrics for MIMO-OWC

1. Bit-Error-Rate and worst-channel dominance

For each different modulation scheme, the BER can be expressed as a function of the Symbol-Error-Rate (SER), which measures performance in the actual transmission process [13]. In MIMO systems, the overall SER is just the average of the N channel SERs. The relationship between channel SER and the channel quality (represented by the Signal-to-Noise Ratio (SNR)) takes the general form [13]:

$$SER_i = \alpha \operatorname{erfc}\left(\beta\sqrt{SINR_i}\right) \quad \text{Eq.50}$$

Winitzki in [98] introduces an approximation for the function $\operatorname{erfc}(\cdot)$:

$$\operatorname{erfc}(x) \approx 1 - \frac{x}{|x|}\sqrt{1 - \exp\left(-x^2\frac{\frac{4}{\pi} + ax^2}{1 + ax^2}\right)} \quad \text{Eq.51}$$

Where:

$$a = 8\frac{(\pi - 3)}{3\pi(4 - \pi)} \quad \text{Eq.52}$$

This approximation is evaluated as having a relative difference of $3.5 \cdot 10^{-4}$ at most (where $x \cong 1.5$) and the difference tends to 0 for higher values of x, hence this is a good approximation, especially as the difference is measured in relative terms. Unless the number of Tx is in the region of hundreds, the discrepancy between this approximation and the correct value is negligible.

Substituting Eq.51 into Eq.50, with $\theta_i = \beta\sqrt{SINR_i}$, the channel SER becomes:

$$SER_i = \alpha\left(1 - \sqrt{1 - \exp\left(-\theta_i^2 \frac{\frac{4}{\pi} + a\theta_i^2}{1 + a\theta_i^2}\right)}\right) \quad \text{Eq.53}$$

By plotting the exponential function in Eq.53, it can be seen that, for $\theta_i^2 \geq 10$, the following approximation for the square-root factor in Eq.53 can start to be used:

$$\sqrt{1 - \exp\left(-\theta_i^2 \frac{\frac{4}{\pi} + a\theta_i^2}{1 + a\theta_i^2}\right)} \cong 1 - \frac{1}{2}\exp\left(-\theta_i^2 \frac{\frac{4}{\pi} + a\theta_i^2}{1 + a\theta_i^2}\right) \quad \text{Eq.54}$$

Considering the ratio γ_{ij} between the SERs for two channels i and j, using the approximation in Eq.54:

$$\gamma_{ij} = \frac{\alpha\left(1 - \sqrt{1 - \exp\left(-\theta_i^2 \frac{\frac{4}{\pi} + a\theta_i^2}{1 + a\theta_i^2}\right)}\right)}{\alpha\left(1 - \sqrt{1 - \exp\left(-\theta_j^2 \frac{\frac{4}{\pi} + a\theta_j^2}{1 + a\theta_j^2}\right)}\right)} \cong \frac{\exp\left(-\theta_i^2 \frac{\frac{4}{\pi} + a\theta_i^2}{1 + a\theta_i^2}\right)}{\exp\left(-\theta_j^2 \frac{\frac{4}{\pi} + a\theta_j^2}{1 + a\theta_j^2}\right)} \quad \text{Eq.55}$$

$$= \exp\left(\left(\theta_j^2 - \theta_i^2\right)\left(1 + \left(\frac{4}{\pi} - 1\right)\frac{1}{(a\theta_i^2 + 1)(a\theta_j^2 + 1)}\right)\right)$$

Without loss of generality, assuming $\theta_j^2 \geq \theta_i^2 \geq 10$, then from Eq.55 with $a \cong 0.14$:

$$\gamma_{ij} \geq \exp\left(\left(\theta_j^2 - \theta_i^2\right)\left(1 + \left(\frac{4}{\pi} - 1\right)\frac{1}{(a\theta_i^2 + 1)^2}\right)\right) \cong \exp\left(\theta_j^2 - \theta_i^2\right) \quad \text{Eq.56}$$

Thus, if the difference $\left(\theta_j^2 - \theta_i^2\right)$ is sufficiently large, the ratio γ_{ij} becomes large enough that the SER of channel i dominates that of channel j in the overall system SER calculation: for example, $\gamma_{ij} \geq 100$ for $\left(\theta_j^2 - \theta_i^2\right) \geq 4.6$. If the number of channels N is small enough (*e.g.* smaller than 10) and the condition on the difference $\left(\theta_j^2 - \theta_i^2\right)$ applies for all $j \neq i$, the worst channel i in the system thus dominates the system performance.

In SINR terms, this dominance is expressed as:

$$SINR_j - SINR_i = \frac{\ln \gamma_{ij}}{\beta^2} \geq \frac{\ln \alpha}{\beta^2} \quad \text{Eq.57}$$

Where α is a threshold value for γ_{ij} signifying the channel dominance.

This derivation is based upon several successive approximations, which are all conditional upon:

$$\min_i\{\theta_i^2\} \geq 10 \Leftrightarrow \min_i\{SINR_i\} \geq \frac{10}{\beta^2} \quad \text{Eq.58}$$

As an example, with $\beta = \sqrt{0.5}$ for Binary Phase-Shift Keying (BPSK) [13], this dominance by the worst-quality channel starts at $\min_i\{SINR_i\} = 20$ (or 13dB.) The SINRs for other channels, whose SERs are smaller than 1/100$^{\text{th}}$ of the worst-channel SER (corresponding to $\alpha = 100$) can be as low as 29.2 (or 14.7dB.) As this required difference diminishes in dB terms for larger worst-SNR, the worst-channel dominance of system performance can be considered a realistic approximation for most cases.

For the same modulation scheme, SER and thus BER are functions uniquely of the SINR, as α and β in Eq.50 are modulation-dependent [13]. Therefore, modulation-independent metrics to represent the system performance must correlate with the SER, as the ultimate performance metric, in the same way as the SNR does.

2. Geometry-based metrics

$$\vec{\boldsymbol{y}}(t) = \underline{\boldsymbol{H}} \times \vec{\boldsymbol{x}}(t) + \vec{\boldsymbol{n}}(t) \qquad \text{Eq.59}$$

Eq.59 describes the transfer between the Tx and the Rx of the modulated signals by neglecting the DC components in Eq.6. Of the two deterministic components of Eq.59, $\vec{\boldsymbol{x}}(t)$ is modulation-dependent, whilst the channel-matrix $\underline{\boldsymbol{H}}$, as can be seen from Eq.35, is a function of only the system geometry (and some constant factors.) Therefore, the metrics must be based on $\underline{\boldsymbol{H}}$, and on other signal-related factors which can be set constant for all modulation schemes.

a. Condition number

For a metric based only on the matrix $\underline{\boldsymbol{H}}$, it must be able to measure how easily $\underline{\boldsymbol{H}}$ can be recovered from Eq.59. The condition number of $\underline{\boldsymbol{H}}$, denoted $\mathrm{cond}(\underline{\boldsymbol{H}})$, is a suitable metric: larger $\mathrm{cond}(\underline{\boldsymbol{H}})$ leads to worse deviations of the estimate from $\vec{\boldsymbol{x}}(t)$ [97]. The condition number is the ratio of the largest singular value of $\underline{\boldsymbol{H}}$ to the smallest one [97].

The condition-number shows that a non-imaging system generally performs worse than the imaging one, for the same configurations. As can be seen from Eq.35, a non-imaging $\underline{\boldsymbol{H}}$ is relatively uniform, thus the singular values corresponding to the decomposable columns are zero or very small. The consequently large $\mathrm{cond}(\underline{\boldsymbol{H}})$ leads to the low performance of MIMO detection and decoding.

With the definitional minimum of 1 for condition numbers, channel matrices with condition numbers between 1 and 10 can empirically be considered ideal. Those with $\mathrm{cond}(\underline{\boldsymbol{H}})$ between 10 and 100 can be seen as well-conditioned, whilst $\mathrm{cond}(\underline{\boldsymbol{H}})$ beyond 1000 indicate ill-conditioned channel matrices.

b. Signal-to-Noise Ratio and Signal-to-Interference-and-Noise Ratio

If a ZF detector is used, the recovered signal for the i^{th} channel takes the form:

$$x_i''(t) = x_i(t) + \vec{\boldsymbol{g}}_i \cdot \vec{\boldsymbol{n}}(t) \qquad \text{Eq.60}$$

From Eq.60, the quality of this MIMO-detected channel is expressed via the SNR [13]:

$$SNR_i = \frac{E(|x_i(t)|^2)}{E(|\vec{\boldsymbol{g}}_i \cdot \vec{\boldsymbol{n}}(t)|^2)} = \frac{\sigma_x^2}{\sigma_n^2 \left[\underline{\boldsymbol{G}} \times \underline{\boldsymbol{G}}^{\dagger}\right]_{ii}} = \frac{\sigma_x^2}{\sigma_n^2 \left[\left(\underline{\boldsymbol{H}}^{\dagger} \times \underline{\boldsymbol{H}}\right)^{-1}\right]_{ii}} \qquad \text{Eq.61}$$

Eq.61 thus shows that, with a fixed signal variance σ_x^2 and constant noise power σ_n^2, the SNR of a ZF-detected channel is solely a function of the channel matrix and thus is modulation-independent. It is expected that due to the similarity of Eq.60 with that of a typical SISO channel [13], the relationship between this SNR and the SER should follow closely the theoretical predictions in Eq.50. However, this SNR definition suffers from the weakness of ZF detection. Since $\text{cond}\left(\underline{\boldsymbol{H}}^{\dagger} \times \underline{\boldsymbol{H}}\right) = \left(\text{cond}\left(\underline{\boldsymbol{H}}\right)\right)^2$, thus if $\underline{\boldsymbol{H}}$ is ill-conditioned, $\left(\underline{\boldsymbol{H}}^{\dagger} \times \underline{\boldsymbol{H}}\right)$ also is. This leads to the computational instability of Eq.61 since the inversion therein involves calculating the reciprocals of very small singular values [97].

In Chapter II.B, it is shown that the MMSE algorithm can alleviate the problem of the ill-conditioned channel matrix. However, since the cross-talk terms do not vanish with the MMSE detector, the concept of Signal-to-Interference-and-Noise Ratio (SINR) is introduced to take into account the cross-talk interferences to the estimate $x_i''(t)$ [99, 100]:

$$SINR_i = \frac{E\left(\left|x_i^{desired}(t)\right|^2\right)}{E\left(\left|x_i^{undesired}(t)\right|^2\right)} \text{ (see definitions of terms in Eq.30)} \qquad \text{Eq.62}$$

For the ZF detector, the SINR is equal to the conventional SNR, thus for consistency the ratio in Eq.61 is referred to as SINR^{ZF} from now on. The SINR of the MMSE detector can be shown to take the form [100]:

$$SINR_i^{MMSE} = \frac{\sigma_x^2}{\sigma_n^2 \left[\left(\frac{\sigma_n^2}{\sigma_x^2} \underline{\boldsymbol{I}}_N + \underline{\boldsymbol{H}}^{\dagger} \times \underline{\boldsymbol{H}} \right)^{-1} \right]_{ii}} - 1 \qquad \text{Eq.63}$$

Compared with Eq.61, the addition of $(\sigma_n^2/\sigma_x^2)\underline{\boldsymbol{I}}_N$ in Eq.63 stabilises the inversion, since the singular values of the matrix to be inverted are all larger than σ_n^2/σ_x^2. Thus the effective noise (denominator in Eq.63) is not much amplified for ill-conditioned $\underline{\boldsymbol{H}}$.

c. SISO-equivalent Signal-to-Noise Ratio

The definition of SINR (and by extension, the ZF-only SNR) so far presented is only applicable to the post-MIMO-detection channel, which for signal processing purposes is no different from a SISO channel. For comparison of this SISO-equivalent channel in MIMO with a true SISO channel, a pre-MIMO-detection metric is proposed. It is defined as the SNR calculated for the SISO system between the i^{th} Tx and the best Rx corresponding to it:

$$SNR_i^{SISO} = \frac{E\left(\left|h_{ji}x_i(t)\right|^2\right)}{E\left(\left|n_j(t)\right|^2\right)} = \frac{h_{ji}^2\sigma_x^2}{\sigma_n^2} \quad \text{with } j = \arg\max_j\left(h_{ji}\right) \qquad \text{Eq.64}$$

By comparing SINR and the corresponding SNR^{SISO}, the interference magnitude can be seen, illustrating the relative quality of the two MIMO and SISO channels, respectively.

B. Simulation of MIMO-OWC and results

The previous chapters have discussed the theoretical model of a MIMO-OWC system, with Chapter III proposing three geometry-based metrics for the system performance. In this chapter, a computer-based simulator is introduced for the MIMO-OWC system discussed in Chapter II. It also incorporates the processing and estimation discussions in Chapter II.B and Chapter II.C. The results of a computer-based experiment conducted with this simulator are also presented.

1. Computer-based simulator of the proposed model

a. System simulation in MATLAB

i. Structure overview

For research into relationships between the channel parameters and the performance of MIMO-OWC, a simulator of the system model has been built. The channel is simulated using the optical ray-tracing package ZEMAX-EE. The main code, written in MATLAB, then simulates the working of the MIMO system. Figure 12 shows the diagram of the components.

The system configurator is a graphic user-interface which takes user-defined inputs for the system which are fed to the appropriate modules as control data. The input-data module generates N pseudo-random bit-streams $\vec{\boldsymbol{s}}(t)$ of user-defined length. Each of these is encoded to full-depth NRZ-OOK and passed to the Tx-electronics simulator, where it is oversampled and band-limited (if selected.)

From this simulator's output and the channel matrix $\underline{\boldsymbol{H}}(t)$ supplied by the ZEMAX-based simulator, the noiseless received data is simulated. Vectors representing AWGN noise are added to the noiseless data.

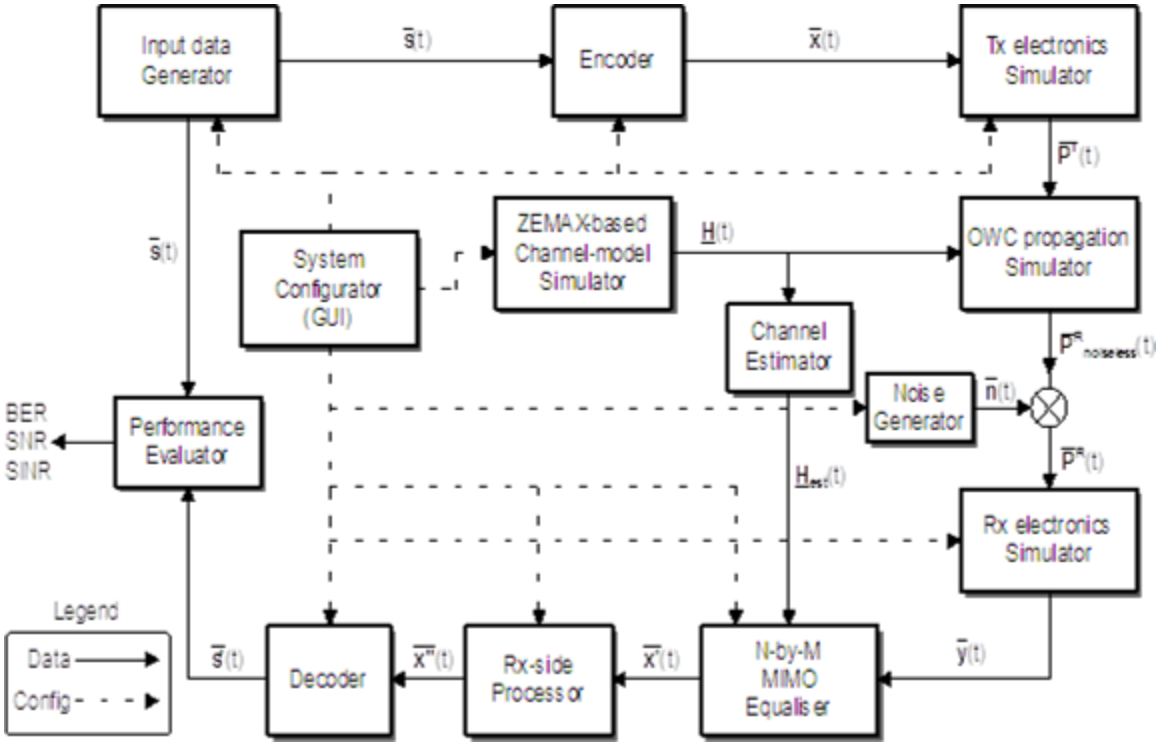

Figure 12. Block-diagram of the MATLAB simulator for general MIMO-OWC

At the Rx-electronics simulator, the output of the propagation simulator is down-sampled, quantised with an Analogue-to-Digital simulator and (if selected) band-limited again. The simulator output $\vec{\boldsymbol{y}}(t)$ is then MIMO-detected with an appropriate algorithm based on the estimated version of the channel matrix. The MIMO-detected data is (if necessary) post-equalised in the Rx-side processor module. The output $\vec{\boldsymbol{x}}''(t)$ is passed into decoders to get estimates of the original bit streams. These are then compared with $\vec{\boldsymbol{s}}(t)$ and system-performance metrics are output.

As discussed in Chapter III, the studied MIMO-OWC model is strictly LoS in nature, and the limitation by bandwidths of the Tx and Rx electronics is neglected. Thus:

- The channel matrix $\underline{\boldsymbol{H}}(t)$ is time-invariant and the OWC propagation simulator is reduced to a simple matrix-multiplication (*cf*. Eq.6.) Also, the ZEMAX-based channel simulator only needs to generate one channel matrix for each configuration, greatly

decreasing the ZEMAX simulation-time which is the single most time-consuming operation. Furthermore, the channel estimator needs to run only once for each configuration and design of the estimation process is thus greatly simplified.

- MIMO-detection is simplified from convolution recovery to multiplicative de-multiplexing. As can be seen in Eq.7 and Eq.8, the only operations required in this process now are calculating an appropriate MIMO-detector $\underline{\boldsymbol{G}}$ and multiplying it with the received signal streams.

- The multiplicative model of Eq.6 implies that effectively there is no temporal inter-symbol interference (ISI) in both $\vec{\boldsymbol{x}}(t)$ and $\vec{\boldsymbol{y}}(t)$. This allows for encoder and decoder to process the signals as a series of temporally-independent spatial-vectors.

- By allowing the optical power of sources in ZEMAX ray-tracing simulation to include all multiplicative constants for $\underline{\boldsymbol{H}}$ (*cf*. Eq.6), the electronics simulators can be avoided.

It is worth noting that the modularity of this simulator means that in future, extending this simulator for the operation of different channel types will be relatively straightforward. The propagation in both general OWC channels and strictly diffuse channels can be simulated with appropriate channel matrices $\underline{\boldsymbol{H}}(t)$ generated from ZEMAX, or from suitable analytical models (see Chapter II.C.) The other two matrix components of Eq.4, $\underline{\boldsymbol{h}}_{Tx}(t)$ and $\underline{\boldsymbol{h}}_{Rx}(t)$, can also be configured to be bandwidth-limited in the corresponding simulators.

ii. Improving simulation speed

To reduce simulation time, two architectural considerations are implemented:

- Channel matrices corresponding to all configurations are generated together in a single ZEMAX ray-tracing operation before the MATLAB simulator is called. This saves the computer memory from having to hold idle data useful only in the MATLAB simulation, since a single ZEMAX simulation can take up to hours to run, as found through experience.

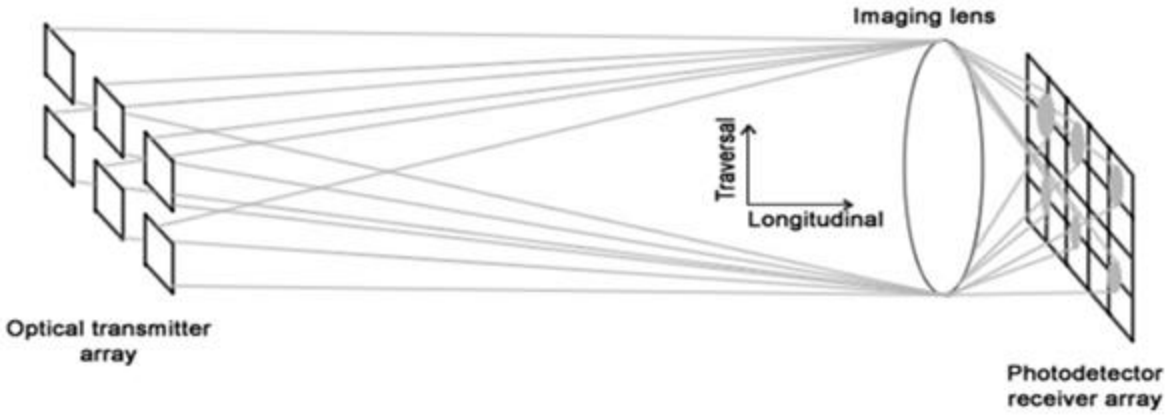

Figure 13. Geometry of the OWC channel in the experiment (not to scale)

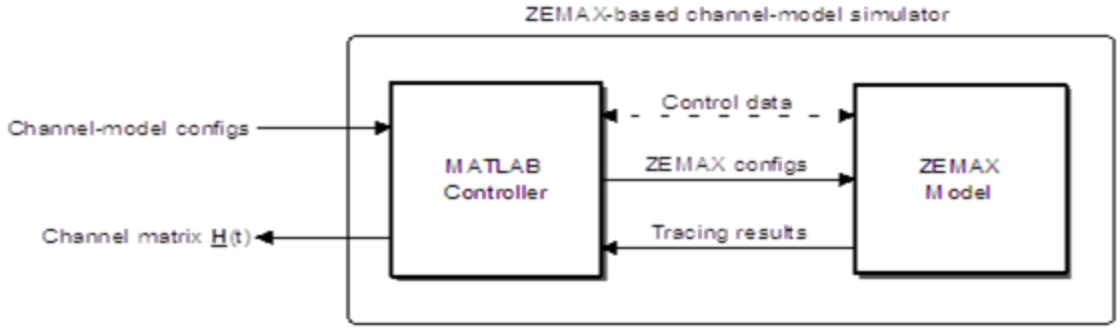

Figure 14. Block-diagram of the ZEMAX-based channel-model simulator

- As MATLAB only handle variables up to certain sizes [101], it is not possible to test the system with long data-streams within a single run. Thus a looping mechanism is designed to repetitively run the simulation with relatively shorter streams to collect sufficient statistics.

b. Channel simulation with ZEMAX

As already mentioned, propagation of visible light in the MIMO-OWC channel is simulated with the commercial ray-tracing package ZEMAX. To input configurations to and retrieve tracing results from ZEMAX, a MATLAB-based controller is built. Figure 14 shows the exchange of data between this controller and the relevant ZEMAX model.

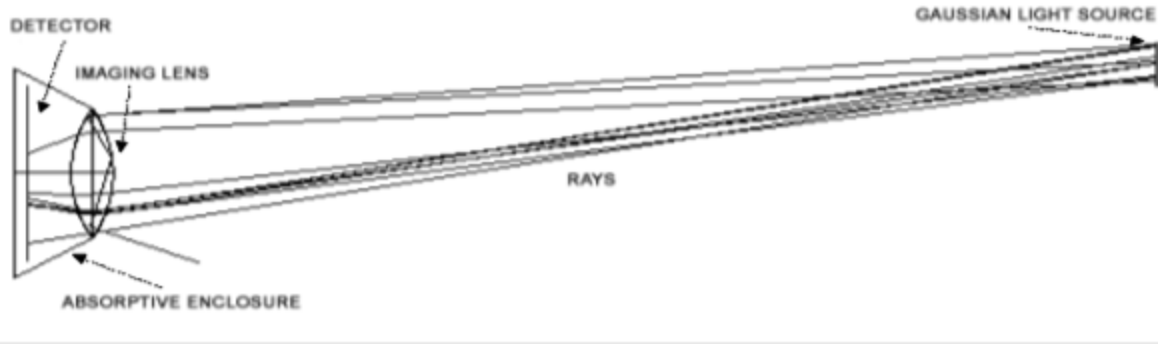

Figure 15. An imaging MIMO-OWC model in ZEMAX (not to scale)

Figure 13 shows the geometry of an imaging OWC channel. Figure 15 depicts the planar view of the channel model used in ZEMAX calculations.

With the Rx system fixed, the ray-tracing in ZEMAX for each Tx is performed by successively moving the only optical source round the set of Tx positions valid for the current geometric configuration. This predefined source has a Gaussian intensity profile. All emitted rays are traced to the photo-detector array. The absorptive enclosure around the receiver system is to ensure that rays arriving at the detector have to have passed through the imaging lens, which is analogous to the situation in reality where the lens aperture is the only opening for light from outside to reach the photodetectors.

For each Tx-Rx combination, ZEMAX collects all the rays from the source position corresponding to the i^{th} Tx, which arrive at the j^{th} photo-detector. Using its own ray-counting algorithm, ZEMAX then outputs the received power for each detector. The ratio between that figure and the total emitted power of the source is the element h_{ji} of the channel matrix $\underline{\boldsymbol{H}}(t)$.

2. Simulation-based experiment

a. Aims

This simulation-based experiment tests the suitability of the three metrics proposed in Chapter III.A.2, using the simulator described in Chapter III.B.1. It also provides empirical verification for the prediction of the worst-channel dominance as discussed in Chapter III.A.1.

b. Procedure

1. *N* pseudo-random bit streams are generated as input to the *N* parallel Tx processes.
2. For each channel geometry, the simulator runs with those *N* streams as input.
3. BER and SINR (based on Eq.62) for each SISO-equivalent channel are calculated.
4. Experimental SINR is compared with the SINR calculated from Eq.61 for ZF or Eq.63 for MMSE.
5. Experimental channel BER is plot against the theoretically-calculated SINR for the corresponding channel.
6. Experimental system BER is plotted against the lowest SINR at each configuration.

c. System configurations

As discussed in Chapter III.A.2.a, the non-imaging scenario is undesirable due to poor recovery performance, thus only the imaging scenario is simulated. The simulated MIMO-OWC system had 6 Tx and 20 Rx with the channel-geometry following that in Figure 13. Variables in the geometry are: power and beam angle of the light-source, number of detectors, material of the lens, and all geometric sizes and relative positions of all the components. The system parameters are shown in Table 1.

Relative centre displacement of Rx- and Tx-arrays	Longitudinal		50cm to 500cm (step of 5cm)
	Traversal		-200cm to 200cm (step of 10cm)
Transmitter	Array arrangement		Rectangular: 2 by 3, pitch 6.2cm
	Lambertian order of source		1
	Average power		0.5 mW
	Tracing		2.5 million rays per position
Receiver	Array arrangement		Rectangular: 4 by 5, pitch 0.4cm
	Field-of-view (full)		150 degrees
ZEMAX optical simulation	Imaging lens - Diameter		3 cm
	Imaging lens - F-number		1
	Wavelength		550nm
Data stream	Symbol length		Stream for each Tx is 50 repetitions of 1000 pseudo-random symbols
	Modulation scheme		Full-depth NRZ-OOK
Rx processing	Sampling		20 samples per symbol
	Analogue-to-Digital simulation	Amplitude	0.0001
		Resolution	16 bits per sample
	AWGN power		$10^{-16}.(\text{mod.amp})^2$

Table 1. Parameters of the 6-Tx 20-Rx MIMO-OWC system in the simulation

3. Results & Discussions

a. Performance metrics

In this section, the performances of the different metrics introduced in Chapter III are presented.

As discussed, the BER is used as the benchmark against which each of the proposed metrics is evaluated with regards to how well they measure the data transfer and processing. The lowest BER level assertable in the simulation are 10^{-4}. This is due to the stream length of 50,000 symbols per channel which permits reliable BER estimation to 10^{-4} only [102]. Therefore, cases where the simulated BERs were lower than 10^{-4} are not shown.

For comparison, each configuration in the simulation was run with both MMSE and ZF as the MIMO-detection algorithm. In the plots, each point represents the data for a single geometric position (*i.e.* a particular relative displacement between the Tx array and the Rx array.) And unless otherwise noted, the per-channel results are all from the physical channel 2 (corresponding with Transmitter 2) which, by visual inspections, are considered representative of all channels.

The calculated SINRs are the theoretical values for each channel calculated according to Eq.61 and Eq.63 from the channel matrix. The simulated SINRs are the ratios calculated arithmetically from the real signals collected and decoded for each channel using the fundamental definition in Eq.62.

Figure 16 shows the plots of the system BER versus the condition number of the channel matrix. The imprecise nature of the BER-$\mathrm{cond}(\underline{\boldsymbol{H}})$ trends, where one value of $\mathrm{cond}(\underline{\boldsymbol{H}})$ can correspond to three orders of magnitude of the BER, excludes $\mathrm{cond}(\underline{\boldsymbol{H}})$ from being a good indicator of the system performance. However, the BER-$\mathrm{cond}(\underline{\boldsymbol{H}})$ trends have the distinctly inverse-exponential shapes, similar to the classic relationship between BER and

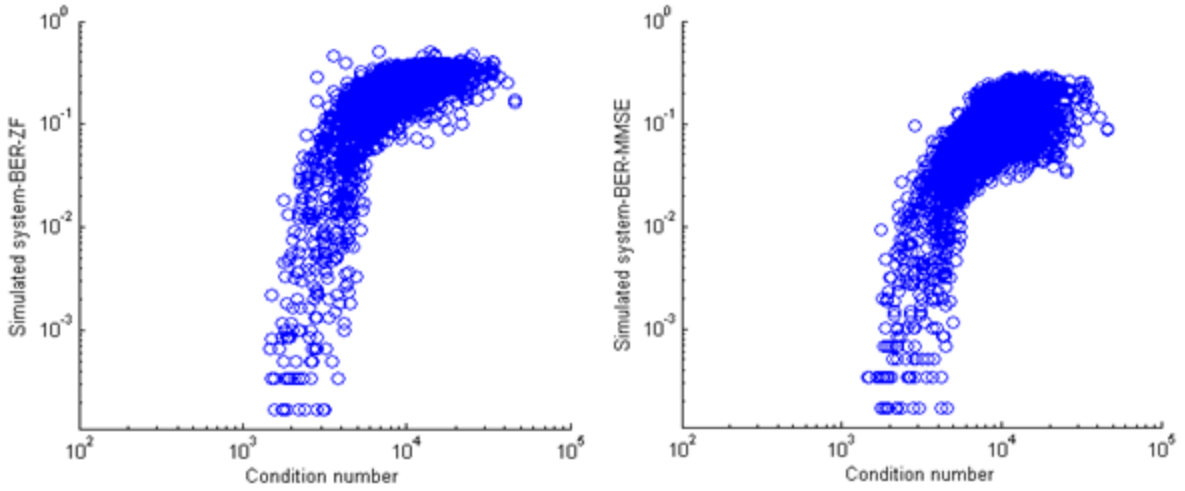

(a) (b)

Figure 16. Condition number vs (a) System-BER^{ZF} and (b) System-BER^{MMSE}

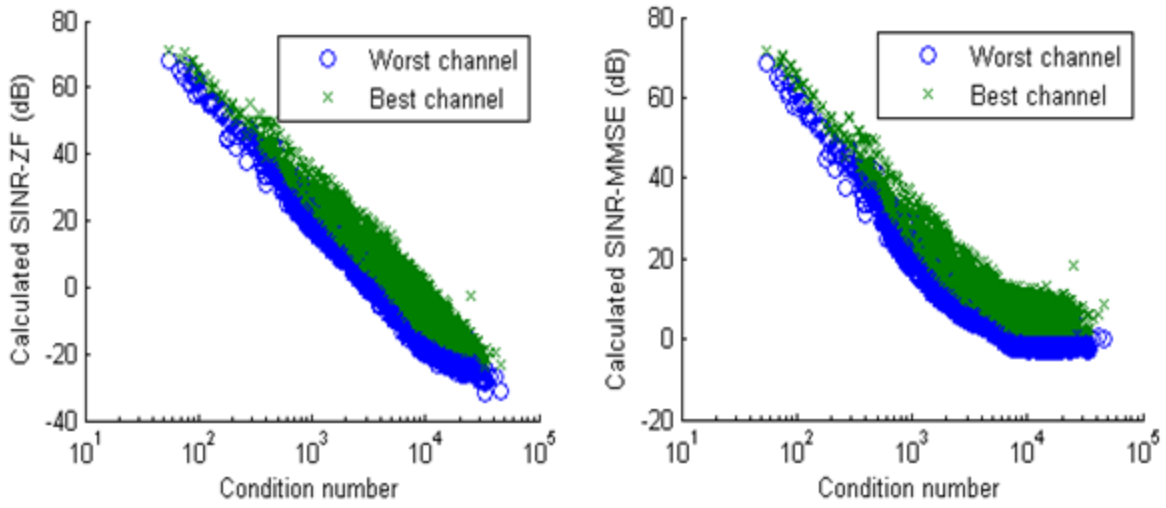

(a) (b)

Figure 17. Condition number vs (a) SINR^{ZF} and (b) SINR^{MMSE}

SNR. This thus points to certain correspondence between cond($\underline{\boldsymbol{H}}$) and SINR (or the MIMO-counterpart of SNR), and this is more clearly shown in Figure 17.

Figure 17 shows the plots of the SINRs for the best and the worst channels versus the condition numbers. The worst channels and the best channels are defined for each individual geometric position as the channels that have the lowest and the highest SINR, respectively, at that geometric position. The plateaued portion, where cond($\underline{\boldsymbol{H}}$) is high, of the MMSE plots in Figure 17b can be explained by the component $(\sigma_n^2/\sigma_x^2)\underline{\boldsymbol{I}}_N$ in Eq.63. This component starts to

dominate when there are channels with corresponding singular values smaller than 1 in magnitude (for the relevant algebraic manipulations, see, for example, [100].) As such, when the magnitude of the singular values of the worst channel becomes smaller than 1, the SINRs of all channels are affected, resulting in flat SINR trends for both the best and worst channels.

The downward sloping portions in both plots of Figure 17 point to a negative-power-law correspondence between cond($\underline{\boldsymbol{H}}$) and SINR. The exact reason behind this relationship is not known, and may be a consequence of the distribution of values in $\underline{\boldsymbol{H}}$. Further investigation is essential, since if this SINR-cond($\underline{\boldsymbol{H}}$) relationship is generally true, cond($\underline{\boldsymbol{H}}$) can serve as a metric to represent the trends of the computationally-involved SINR.

Both Figure 18 and Figure 19 show the channel SINRs plotted against the channel BER, for ZF and MMSE respectively, as well as the theoretical SNR-BER relationship for OOK modulation [103]. It can be seen that in all four graphs, there is good agreement, for most of the range, between the SINR-BER plots and the theoretical relationship for OOK.

Combining these results with the BER-cond($\underline{\boldsymbol{H}}$) and SINR-cond($\underline{\boldsymbol{H}}$) relationships in Figure 16 and Figure 17, respectively, it can be seen that the SINR-BER relationship shown

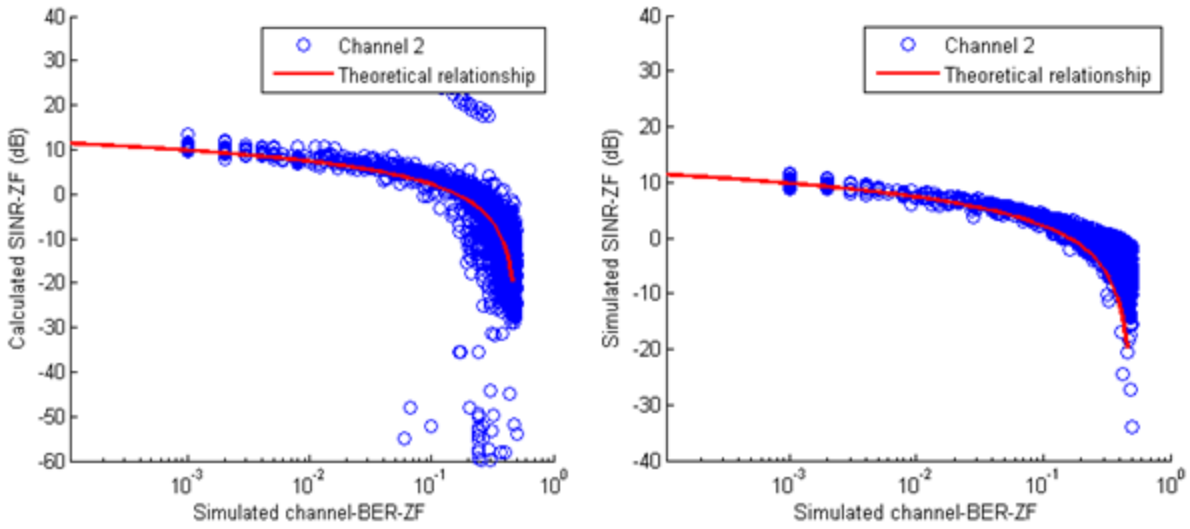

Figure 18. Simulated channel-BER^{ZF} vs (a) Calc. SINR^{ZF} and (b) Sim. SINR^{ZF}

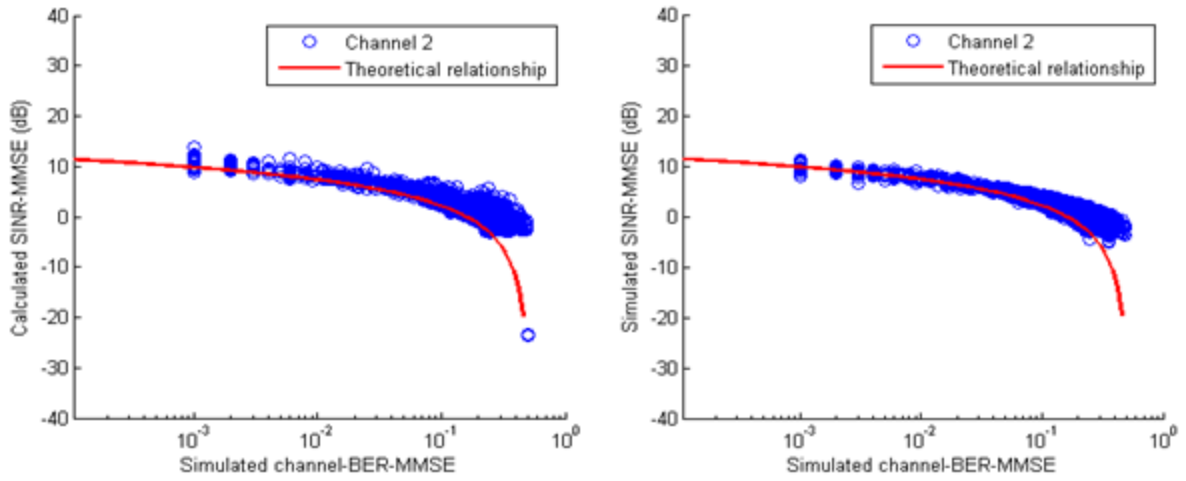

(a) (b)

Figure 19. Channel-BER^{MMSE} vs (a) Calc. SINR^{MMSE} and (b) Sim. SINR^{MMSE}

in Figure 18 and Figure 19 can be extrapolated for cases where the SINR is higher and the BER is lower than depicted.

The only exception where SINR and BER do not seem to correspond is in the rightmost portion of Figure 18a, where against channel-BER is plotted the SINR calculated directly from the algebraic expression in Eq.61. This violation can be explained by that $\underline{\boldsymbol{H}}$ corresponding with large BERs has very high condition numbers (*cf*. Figure 16) and thus is highly ill-conditioned. Therefore, the matrix inverse calculation in Eq.61 is prone to errors, leading to incorrect values for the calculated SINR.

In contrast, the plot between BER and the SINR values obtained from the definitional formula, where no matrix inversion is involved, corresponds almost perfectly with the theoretical prediction in Figure 18b.

Thus, the good fit between the SINR-BER plots and the theoretical single-channel BER-SNR relationship shows that SINR, already used as RF MIMO equivalent of the conventional SNR, can also be used in the optical MIMO communications to indicate channel quality. Its modulation-independence and closed-form relationship with $\underline{\boldsymbol{H}}$ (see Chapter III.A.2.b) suggests it as a good candidate for the design metric to optimise the channel quality.

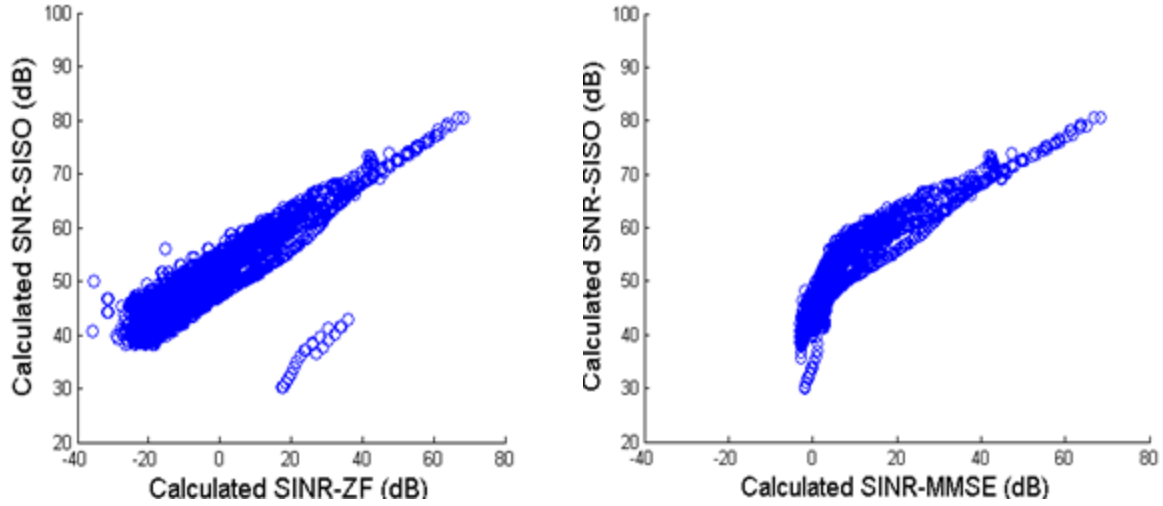

(a) (b)

Figure 20. SNR^{SISO} vs (a) $SINR^{ZF}$ and (b) $SINR^{MMSE}$

Figure 20 shows the plots between SINR and SNR^{SISO} (defined in Chapter III.A.2.c) for channel 2. It can be seen that SINR is always lower than SNR^{SISO}: except for the near-0dB range of SINR in Figure 20b, the differences between SNR^{SISO} and SINR are between 20dB and 50dB for both ZF and MMSE recovery algorithms. Hence the individual MIMO-OWC sub-channel is always worse than a corresponding SISO channel. Given the good fit of SINR-BER with the theoretical SNR-BER prediction for OOK, SNR^{SISO} does not to represent the channel quality well.

Another conclusion from Figure 20 is that under the same operating conditions, it is the presence of the interference term in the denominator of SINR in Eq.61 that causes the difference between SINR and SNR^{SISO}. Such huge shifts downwards in dB terms imply that interference are the main limiting factor in MIMO systems: this inference is also evidenced in the fact that in more well-conditioned MIMO configurations where SINR is larger, the SINR-SNR^{SISO} difference is smaller and this gap increases when SINR gets smaller, as seen in Figure 20. Thus reducing cross-channel interference would give the largest performance improvements for a given MIMO physical configuration.

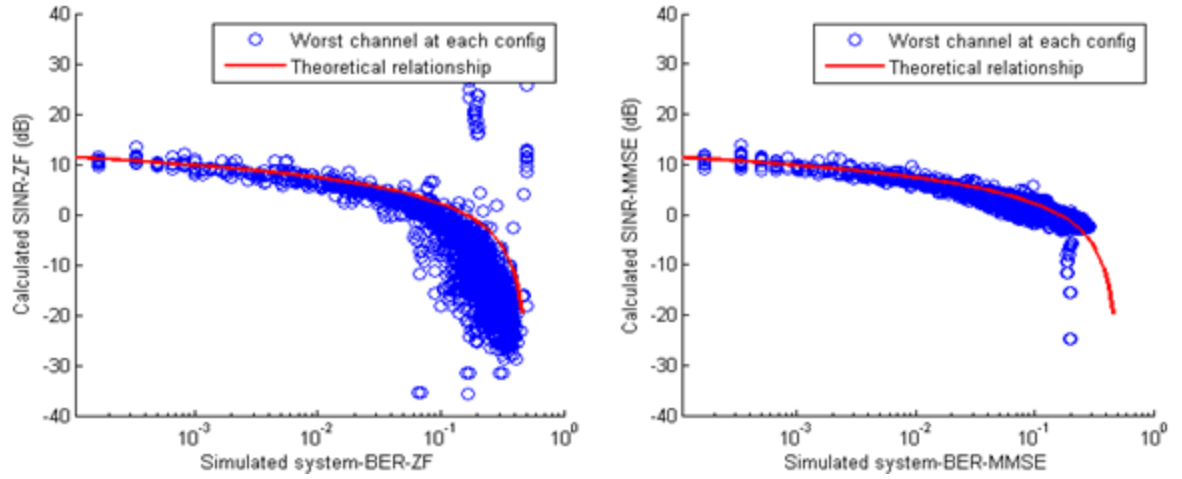

(a) (b)

Figure 21. System-BER vs Worst-channel SINR for (a) ZF and (b) MMSE

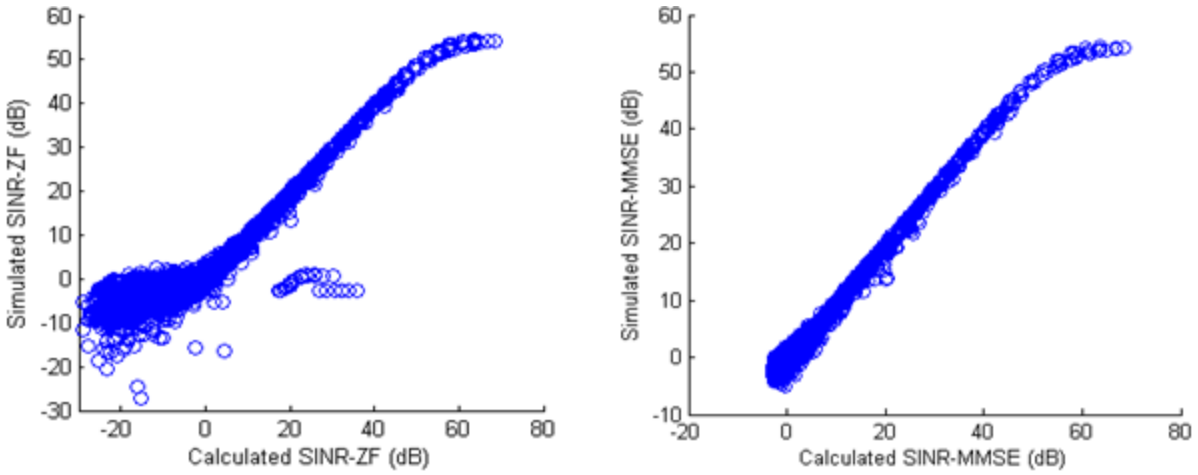

(a) (b)

Figure 22. Calculated vs Simulated for (a) $SINR^{ZF}$ and (b) $SINR^{MMSE}$

Error! Reference source not found. depicts the plots between the SINR for the worst channel at each Tx-Rx relative position, and the system-BER, and the theoretical SNR-BER relationship for OOK modulation [103]. For both ZF and MMSE, the worst-channel-SINR vs. system-BER plots follow quite closely the theoretical relationship for the left half of each graph where SINR is comparatively high, thus confirming the prediction of worst-channel dominance presented in Chapter III.A.1. The scattering at the right half of **Error! Reference source not found.**a is explained by the arithmetic imprecision due to the ill-conditioned $\underline{\boldsymbol{H}}$.

Finally, **Error! Reference source not found.** shows the plots of the SINR calculated from definitions in Eq.62 against the SINR for the same channel, but calculated from the channel matrix. In the ideal case, the plots should have a slope of unity throughout. The deviations at the upper right and lower left of both plots show the importance of the $\underline{\boldsymbol{H}}$-estimation accuracy. At the higher SINR (corresponding to smaller cond($\underline{\boldsymbol{H}}$) in Figure 17) small changes in h_{ji} values may cause significant changes in the singular values of $\underline{\boldsymbol{H}}$, and thus in the value of SINR. The imperfection at the lower SINR can be explained by large values of cond($\underline{\boldsymbol{H}}$) affecting inversion which is more pronounced with ZF than with MMSE, as already predicted in Eq.63. For the intermediate range, the estimation algorithm introduced in Chapter II.C.2 works well.

b. Spatial distributions

In this section, the spatial distributions of the 'good' and the 'bad' values of the metrics of interest are presented in order to understand how the relative geometrical positions between the Tx and the Rx arrays influence the link performance.

Figure 23 shows the spatial distribution of cond($\underline{\boldsymbol{H}}$) for the true (*i.e.* not estimated) channel matrix $\underline{\boldsymbol{H}}$. The most prominent feature of this distribution is the presence of the various radial lobes in an alternating fashion, symmetrical about the median plane of the system. In other words, for a given distance between the Tx and the Rx, when the azimuthal angle varies, cond($\underline{\boldsymbol{H}}$) alternatingly increases and decreases in value.

This variation can be explained by the fact that when the Tx moves azimuthally relative to the Rx, the images of the Tx move across the Rx surface. Two adjacent images thus go through alternating phases when they both are incident on the same Rx with similar powers, and when they are incident on two completely different Rx, *i.e.* they alternate between periods of high and low overlaps of the different images on the same Rx. Given the interpretation of

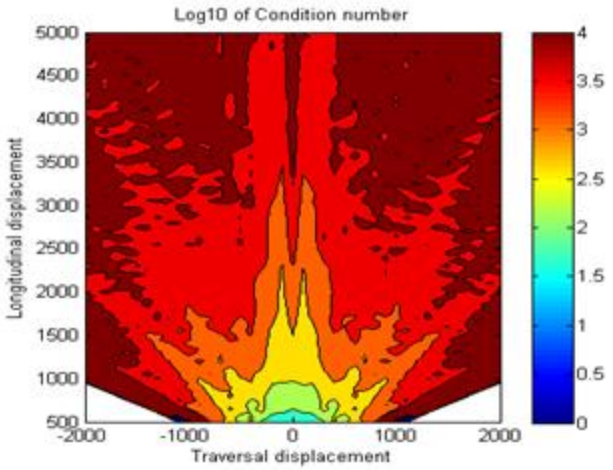

Figure 23. Contours of condition number: Linear displacements (in mm)

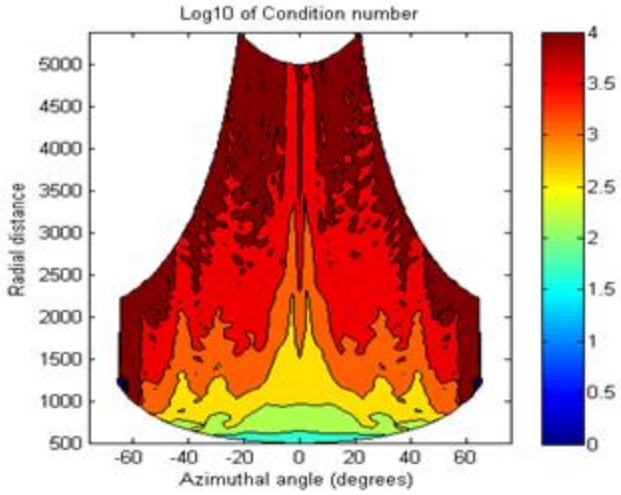

Figure 24. Contours of condition number: Polar displacements (radial distances in mm)

condition numbers as indications of the overlapping level, the existence of radially-distributed lobes is thus explained.

A corollary from this explanation, whose evidence can be seen in Figure 23 but is more prominent in Figure 24, is that the lobes at larger radial distances tend to be relatively thinner, *i.e.* lower ratio of width to length, than those at shorter radial distances. This is the direct result of the fact that at larger distances, the Tx images on the Rx surface are smaller, thus the transition between high and low levels of overlapping takes place over smaller angular variations, leading to the apparent thinness of the lobes.

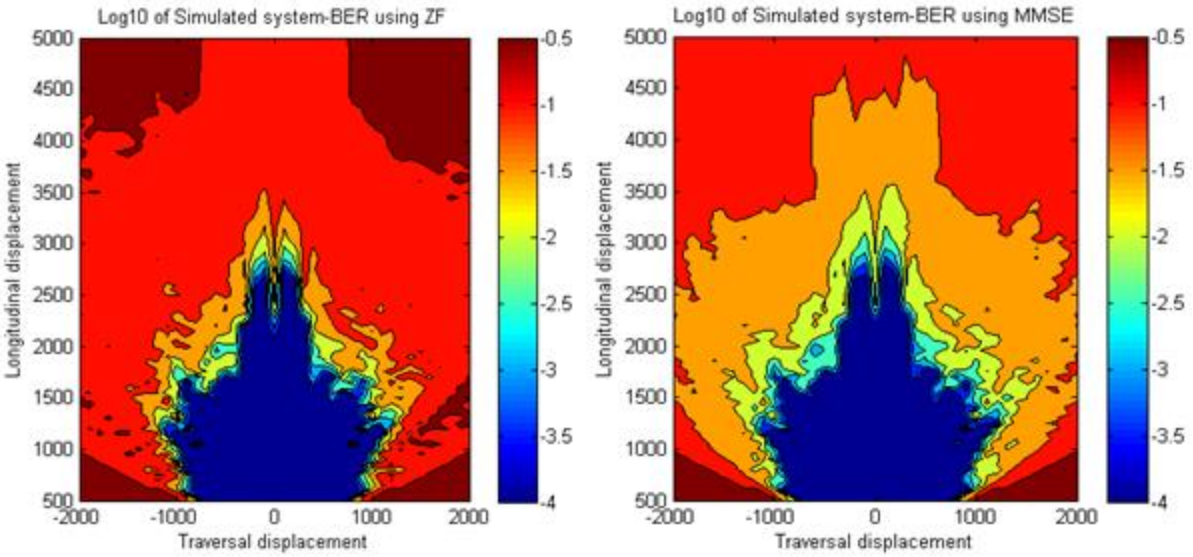

(a) (b)

Figure 25. Contours of system BER using (a) ZF and (b) MMSE (displacements in mm)

The straight-line boundaries at the lower corners of Figure 23 and the vertical cut-offs at about ±65 degrees in Figure 24 correspond to the nominal field-of-view of 150 degrees (full angle) of the Rx system.

Figure 25 shows the spatial distributions of the system BER when recovered with ZF and with MMSE. It can be seen that these BER spatial distributions take a broadly similar shape to the $\mathrm{cond}(\underline{\boldsymbol{H}})$ distribution shown in Figure 23, which attests to the rough correlation between $\mathrm{cond}(\underline{\boldsymbol{H}})$ and the system BER as depicted in Figure 16. There are two main features of these spatial distributions which distinguish them from Figure 23.

The first feature is that the lobes in the BER distribution are far less pronounced. In fact, besides the two central lobes (about the 0-cm traversal displacement) the other lobes are only discernible at the lower-valued contours (see also Figure 27 and Figure 26.) This indicates that techniques reducing $\mathrm{cond}(\underline{\boldsymbol{H}})$ only by separating the images without other improvements (*e.g.* increasing collected optical powers) have smaller effects on improving the overall system performance.

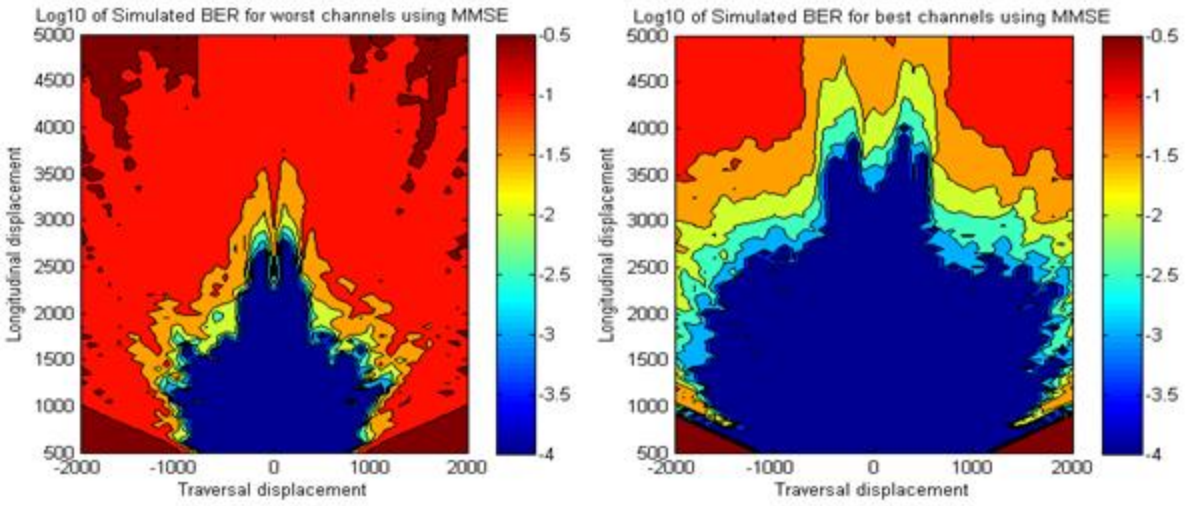

(a) (b)

Figure 26. Contour plots of BER^{MMSE} vs displacements for (a) Worst and (b) Best channels

The second is that the system performance quickly degrades at $BER \sim 10^{-2}$. This is shown in a sharp boundary dividing the region of acceptable performance ($BER \leq 2 \cdot 10^{-3}$) and that of unacceptable performance, as evidenced in the small spacing between the successive contours. This shows that at the 'right' order of magnitude of cond($\underline{\boldsymbol{H}}$) (in this simulation, about 10^3 and below) a small improvement of the image overlaps can result in a large improvement in system performance. Thus, image-separation techniques are most effective for the more benign channels where the elements of $\underline{\boldsymbol{H}}$ are relatively dissimilar[§].

Figure 26 and Figure 27 show the same distributions for both the worst channels and the best channels (found for every individual spatial position, *cf*. Figure 17). It can be seen clearly that the worst-channel distribution is almost identical to that of the overall system in the region of smaller BER, thus reinforcing the notion of worst-channel dominance as discussed in Chapter III.B.3.a. As a result of this dominance, only increasing the transmitted power

[§] When the elements of $\underline{\boldsymbol{H}}$ become too similar, cond($\underline{\boldsymbol{H}}$) quickly increases, approaching infinity when the elements are all identical. There is a body of mathematical research on the bounds of condition numbers imposed by the magnitude of matrix elements, which, however, is outside the scope of this thesis and is not reported here.

would only increase the system performance by the same factor as a single channel (*i.e.* the worst one) is improved, thus losing advantages of the MIMO technique. Therefore, it can again be seen that improving the condition number of the system is much more beneficial than a simple power boost.

At positions with higher BER, the overall system performance is approximated by neither the worst channel nor the best channel—*cf*. Figure 25. In these ill-conditioned regions (*i.e*. when the performance is poor and the BER is very high), especially for the worst channels, the MMSE algorithm is superior to the ZF, whilst offering similar performance in well-conditioned regions. This is in agreement with the theoretical predictions in Eq.61 and Eq.63 that when $\underline{\boldsymbol{H}}$ is well-conditioned, MMSE results converge to ZF.

In the region of ill-conditioned $\underline{\boldsymbol{H}}$, despite the BER for both ZF and MMSE being too high for currently known uses, it is worth noting that MMSE is vastly superior to ZF, with the contours enclosing much bigger areas. For example, the $10^{-0.5}$ contour with MMSE covers almost twice the ZF area, and almost all of the simulated area.

Both Figure 26 and Figure 27 show that the best channels have much better

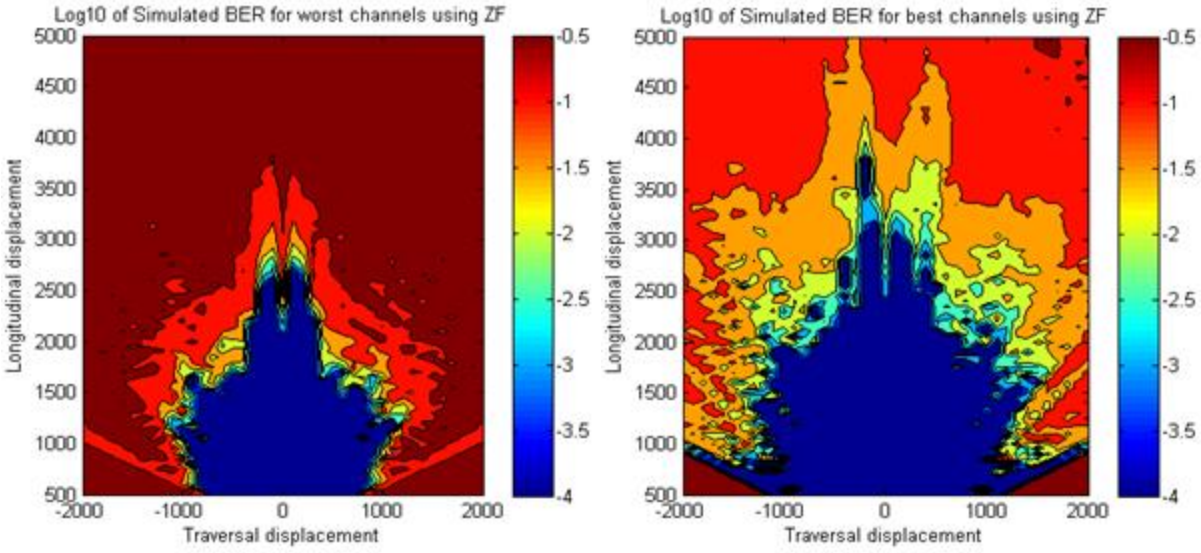

(a) (b)

Figure 27. Contour plots of BER^{ZF} vs displacements for (a) Worst and (b) Best channels

performance than the overall system (*i.e.* the average): firstly, the sub-10^{-3} BER region of the best-channel BER is bigger, almost three times as big with the MMSE recovery in Figure 26; and secondly, the transition between this region and the 'unacceptable' region is more gradual. This implies that even where the overall-system performance is considered unacceptable, it is still possible to form a communication link using a subset of the channels. An appropriate algorithm, such as water-filling, can be used to select the optimal subset for a given channel matrix by allocating the Tx power to the desired channels only [13, 80].

Another corollary from Figure 26 and Figure 27 is that, even though the worst-channel performance is similar using either ZF or MMSE, the best channels are very different for the two algorithms, which appear to 'scale up' the performance of the better channels (*cf*. Figure 26b and Figure 27b.) As such, a careful selection of the MIMO-detection algorithm, even though it has little to no impact on the system performance as a whole due to the worst-channel dominance, is still of great importance, especially for the channel-subset optimisation mentioned before (*cf*. water-filling algorithm for Tx power allocation in RF [80].)

C. Conclusion

In this chapter, to measure the theoretical quality of a particular geometry, three metrics have been proposed: the condition number, the Signal-to-Interference-and-Noise Ratio (SINR) and the SISO-equivalent Signal-to-Noise Ratio (SNR^{SISO}.) These metrics are all based on the channel matrix, and independent of the signals. Simulated transmission for the MIMO-OWC system using a MATLAB-based program shows that the channel SINR is the most appropriate metric as it correlates well with the ultimate transmission metric of BER. The simulation also illustrates that the condition number of the channel matrix, although not possessing a well-defined relationship with the system performance, can also be used as a rough predictor of the performance.

Also, from the theoretical investigation in Chapter III.A.1 of the formula for system Bit-Error-Rate (BER), it has been predicted that the overall performance of a MIMO system would be mostly dominated by its worst channel. This theoretical prediction has been subsequently confirmed with the data obtained from simulation. Combined with the insights on the channel SINR, this result is significant in that, to improve the overall system performance, the most effective way is to maximise the SINR of the worst channel.

As the channel SINRs are functions of the channel matrix, which in turn is a representation of the level of overlaps of the different transmitter images over the receiving photo-detectors, one of the ways to improve the SINRs is to steer the transmitter images such that their distributions over the photo-detectors would reduce the overlaps. In a MIMO-OWC system using visible light sources such as light-emitting diodes, this equates to performing beam steering for partially coherent light.

Chapter IV will study the theory of such a beam-steering operation using holograms and lay the analytical foundations for a family of novel hologram-generating algorithms for the partially-coherent-illumination regime.

Chapter IV. **Theoretical analysis of holographic beam-steering for partially-coherent light**

In Chapter III, simulation results show that improving the condition number of the channel matrix is the chief means to improve the MIMO performance. One way to alter the channel matrix is to use beam-steering techniques to move the transmitter images to desired locations on the receiver plane. Holographic techniques have been extensively used in forming different illumination patterns with coherent light [32, 34, 37, 53, 54, 56, 58, 59, 64,

65, 72]. For visible-light optical wireless communications where MIMO is typically proposed, the partially-coherent nature of the illumination makes the use of holograms less straightforward. General theories on the propagation of partially-coherent light have been available for nearly 80 years [73-75], but only recently have holograms started to be used with partially-coherent illumination [66, 70]. In this chapter, starting from the first principles of partially-coherent-light propagation, the theoretical foundations for holographic beam-steering will be discussed: equations will be derived relating the input and the desired output via the hologram; and two algorithms will be proposed for the search of that hologram.

A. Formulation of the partially-coherent propagation

1. For the general case

The generic relations between the source and image intensities given in §9.5.1 and §10.6.3 of [75] depend on a system-specific variable, which is not straightforward to calculate for partially coherent illumination. Therefore, for the partially coherent systems of interest,

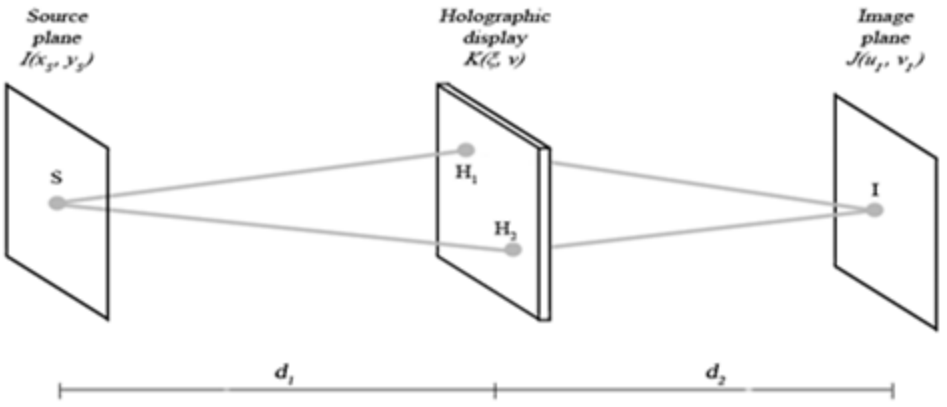

Figure 28. Schematic of the general holographic propagation

the full propagation will be analysed from first principles and the relationship between the source and the image will be derived.

Figure 28 shows the schematic of the system under analysis. Light from an incoherent source with intensity distribution $I(x_S, y_S)$ propagates to a holographic display device to be modulated by a hologram with transmittance $K(\xi, \nu)$ before propagating to an image plane

where the intensity is recorded. Using the van Cittert—Zernike theorem [**] [75] for propagation of partially-coherent quasi-chromatic illumination, the mutual intensity at the front of the hologram plane can be expressed as: ($\bar{k}$ is the wave number of the mean frequency of the quasi-monochromatic illumination)

$$J(\mathrm{H}_1,\mathrm{H}_2) = \iint\limits_{x_\mathrm{S},y_\mathrm{S}} I(x_\mathrm{S},y_\mathrm{S})\frac{e^{j\bar{k}(r_1-r_2)}}{r_1 r_2}dx_\mathrm{S}\,dy_\mathrm{S} \qquad \text{Eq.65}$$

With the hologram modulating the field distribution of the incident light, the mutual intensity at the back of the hologram plane becomes:

$$J'(\mathrm{H}_1,\mathrm{H}_2) = K(\mathrm{H}_1)K^*(\mathrm{H}_2)\iint\limits_{x_\mathrm{S},y_\mathrm{S}} I(x_\mathrm{S},y_\mathrm{S})\frac{e^{j\bar{k}(r_1-r_2)}}{r_1 r_2}dx_\mathrm{S}\,dy_\mathrm{S} \qquad \text{Eq.66}$$

Another step of propagation using the van Cittert—Zernike theorem gives the image intensity at image plane as: (with $s_1 = \mathrm{H}_1\mathrm{I}$, $s_2 = \mathrm{H}_2\mathrm{I}$)

$$J(\mathrm{I}) = \iint\limits_{\mathrm{H}_1,\mathrm{H}_2} J'(\mathrm{H}_1,\mathrm{H}_2)\frac{e^{j\bar{k}(s_1-s_2)}}{s_1 s_2}\Lambda(\mathrm{H}_1)\Lambda^*(\mathrm{H}_2)\,d\mathrm{H}_1\,d\mathrm{H}_2 \qquad \text{Eq.67}$$

Assuming paraxial rays, a propagation distance r from the source plane to the hologram plane can be approximated as: (where $(\xi,\nu) \equiv \mathrm{H}$)

$$r = d_1\sqrt{1+\left(\frac{\xi-x_\mathrm{S}}{d_1}\right)^2+\left(\frac{\nu-y_\mathrm{S}}{d_1}\right)^2} \cong d_1\left(1+\frac{1}{2}\left(\frac{\xi-x_\mathrm{S}}{d_1}\right)^2+\frac{1}{2}\left(\frac{\nu-y_\mathrm{S}}{d_1}\right)^2\right) \qquad \text{Eq.68}$$

Hence, the exponential phase term in Eq.66 becomes:

[**] The van Cittert—Zernike theorem assumes that the source is planar, at least spatially incoherent, of a small angular size and sufficiently distant from the observation planes. It also assumes that the illumination from the source is quasi-monochromatic, *i.e.* the spectral spread is much smaller than the mean frequency.

$$\frac{\exp\left(j\bar{k}(r_1 - r_2)\right)}{r_1 r_2} \cong \frac{1}{d_1^2}\begin{pmatrix} \exp\left(-j\bar{k}\left(x_S\frac{\xi_1 - \xi_2}{d_1} + y_S\frac{\nu_1 - \nu_2}{d_1}\right)\right) \\ \exp\left(j\bar{k}\frac{(\xi_1^2 + \nu_1^2) - (\xi_2^2 + \nu_2^2)}{2d_1}\right) \end{pmatrix} \qquad \text{Eq.69}$$

Substituting Eq.69 into Eq.66, grouping the variables together and denoting the Fourier Transform $\check{I}(\omega,\psi) = \mathcal{F}_{\omega,\psi}\{I(x,y)\}$, the mutual intensity $J(\mathrm{H}_1,\mathrm{H}_2)$ before the hologram becomes:

$$J(\mathrm{H}_1,\mathrm{H}_2) = \begin{pmatrix} \frac{1}{d_1^2}\exp\left(j\bar{k}\frac{(\xi_1^2 + \nu_1^2) - (\xi_2^2 + \nu_2^2)}{2d_1}\right) \\ \iint_{x_S,y_S} \begin{pmatrix} I(x_S,y_S) \\ \exp\left(-jx_S\frac{\bar{k}(\xi_1 - \xi_2)}{d_1}\right) \\ \exp\left(-jy_S\frac{\bar{k}(\nu_1 - \nu_2)}{d_1}\right) \end{pmatrix} dx_S\, dy_S \end{pmatrix} \qquad \text{Eq.70}$$

$$= \frac{1}{d_1^2}\begin{pmatrix} \exp\left(j\bar{k}\frac{(\xi_1^2 + \nu_1^2) - (\xi_2^2 + \nu_2^2)}{2d_1}\right) \\ \check{I}\left(\frac{\bar{k}(\xi_1 - \xi_2)}{d_1}, \frac{\bar{k}(\nu_1 - \nu_2)}{d_1}\right) \end{pmatrix}$$

According to §10.4.4 [75], the inclination factor $\Lambda(\cdot)$ is accounted for by $K(\cdot)$, thus the intensity at the image plane is:

$$J(\mathrm{I}) = \iint_{\mathrm{H}_1,\mathrm{H}_2} J(\mathrm{H}_1,\mathrm{H}_2)\frac{e^{j\bar{k}(s_1 - s_2)}}{s_1 s_2} K(\mathrm{H}_1)K^*(\mathrm{H}_2)\, d\mathrm{H}_1\, d\mathrm{H}_2 \qquad \text{Eq.71}$$

Substituting Eq.70 into Eq.71 and using a similar approximation as in Eq.69 for the exponential phase in Eq.71, the image intensity becomes: (where $(u_\mathrm{I}, v_\mathrm{I}) \equiv \mathrm{I}$)

$$J(\mathrm{I}) = \iint_{\xi_1,\nu_1} \iint_{\xi_2,\nu_2} \left(\begin{array}{c} \frac{1}{d_1^2 d_2^2} K(\mathrm{H}_1) K^*(\mathrm{H}_2) \\ \tilde{I}\left(\frac{\bar{k}(\xi_1 - \xi_2)}{d_1}, \frac{\bar{k}(\nu_1 - \nu_2)}{d_1} \right) \\ \exp\left(-j\bar{k}\left(u_\mathrm{I} \frac{\xi_1 - \xi_2}{d_2} + v_\mathrm{I} \frac{\nu_1 - \nu_2}{d_2} \right) \right) \\ \exp\left(j\bar{k} \frac{(\xi_1^2 + \nu_1^2) - (\xi_2^2 + \nu_2^2)}{2d_1} \right) \\ \exp\left(j\bar{k} \frac{(\xi_1^2 + \nu_1^2) - (\xi_2^2 + \nu_2^2)}{2d_2} \right) \end{array} \right) d\xi_2 \, d\nu_2 \, d\xi_1 \, d\nu_1 \qquad \text{Eq.72}$$

The quadratic exponential terms in Eq.72 can be re-written algebraically as follows:

$$\exp\left(j\bar{k} \frac{(\xi_1^2 + \nu_1^2) - (\xi_2^2 + \nu_2^2)}{2d_1} \right) \exp\left(j\bar{k} \frac{(\xi_1^2 + \nu_1^2) - (\xi_2^2 + \nu_2^2)}{2d_2} \right)$$

$$= \exp\left(j\bar{k} \frac{d_1 + d_2}{d_1 d_2} \frac{\big((\xi_1 - \xi_2) + 2\xi_2\big)(\xi_1 - \xi_2) + \big((\nu_1 - \nu_2) + 2\nu_2\big)(\nu_1 - \nu_2)}{2} \right) \qquad \text{Eq.73}$$

$$= \Phi\big((\xi_1 - \xi_2), (\nu_1 - \nu_2), \xi_2, \nu_2\big) = \Phi(\Delta\xi, \Delta\nu, \xi_2, \nu_2)$$

Substituting Eq.73 into Eq.72, the image intensity can be expressed as:

$$J(\mathrm{I}) = \iint_{\Delta\xi,\Delta\nu} \left(\begin{array}{c} \frac{1}{d_1^2 d_2^2} \tilde{I}\left(\frac{\bar{k}}{d_1} \Delta\xi, \frac{\bar{k}}{d_1} \Delta\nu \right) \\ \exp\left(-\frac{j\bar{k}}{d_2} (u_\mathrm{I} \Delta\xi + v_\mathrm{I} \Delta\nu) \right) \\ \iint_{\xi_2,\nu_2} \begin{pmatrix} K(\xi_2 + \Delta\xi, \nu_2 + \Delta\nu) K^*(\xi_2, \nu_2) \\ \Phi(\Delta\xi, \Delta\nu, \xi_2, \nu_2) \end{pmatrix} d\xi_2 \, d\nu_2 \end{array} \right) d\,\Delta\xi \, d\,\Delta\nu \qquad \text{Eq.74}$$

It can be seen from Eq.74 that there is no general closed-form, mathematically exact solution for the image intensity in the holographic set-up depicted in Figure 28. However, in certain cases, simplification can be made to turn Eq.74 into a functional relationship between the hologram and the image intensity distribution.

2. In the Fraunhofer region

In the Fraunhofer (*i.e.* far-field) region, the longitudinal distances of the propagation are much bigger than the traversal distances: $d_1, d_2 \gg (\xi_1^2 + \nu_1^2), (\xi_2^2 + \nu_2^2)$. Hence the quadratic term in Eq.73 can be approximated as $\Phi(\Delta\xi, \Delta\nu, \xi_2, \nu_2) \cong 1$.

This approximation simplifies Eq.74 into:

$$J_{Fraun}(\mathrm{I}) = \iint_{\Delta\xi,\Delta\nu} \left(\begin{array}{c} \frac{1}{d_1^2 d_2^2} \check{I}\left(\frac{\bar{k}}{d_1}\Delta\xi, \frac{\bar{k}}{d_1}\Delta\nu\right) \\ \exp\left(-\frac{j\bar{k}}{d_2}(u_{\mathrm{I}}\Delta\xi + v_{\mathrm{I}}\Delta\nu)\right) \\ \iint_{\xi_2,\nu_2} K(\xi_2 + \Delta\xi, \nu_2 + \Delta\nu)\mathrm{K}^*(\xi_2, \nu_2)\, d\xi_2\, d\nu_2 \end{array} \right) d\,\Delta\xi\, d\,\Delta\nu \qquad \text{Eq.75}$$

By recognising the inner integral in Eq.75 as the autocorrelation $R_{KK}(\Delta\xi, \Delta\nu)$ of $K(\xi, \nu)$, the Fraunhofer image intensity thus becomes:

$$J_{Fraun}(\mathrm{I}) = \frac{1}{d_1^2 d_2^2} \iint_{\Delta\xi,\Delta\nu} \left(\begin{array}{c} \check{I}\left(\frac{\bar{k}}{d_1}\Delta\xi, \frac{\bar{k}}{d_1}\Delta\nu\right) R_{KK}(\Delta\xi, \Delta\nu) \\ \exp\left(-j\frac{\bar{k}}{d_2}u_{\mathrm{I}}\Delta\xi - j\frac{\bar{k}}{d_2}v_{\mathrm{I}}\Delta\nu\right) \end{array} \right) d\,\Delta\xi\, d\,\Delta\nu \qquad \text{Eq.76}$$

The right-hand side of Eq.76 is the Fourier Transform of $\check{I}\left(\frac{\bar{k}}{d_1}\Delta\xi, \frac{\bar{k}}{d_1}\Delta\nu\right) R_{KK}(\Delta\xi, \Delta\nu)$. Thus, the image intensity can be expressed as:

$$J_{Fraun}(\mathrm{I}) = \frac{1}{d_1^2 d_2^2} \mathcal{F}_{\frac{\bar{k}}{d_2}u_{\mathrm{I}}, \frac{\bar{k}}{d_2}v_{\mathrm{I}}} \left\{ \check{I}\left(\frac{\bar{k}}{d_1}\Delta\xi, \frac{\bar{k}}{d_1}\Delta\nu\right) R_{KK}(\Delta\xi, \Delta\nu) \right\} \qquad \text{Eq.77}$$

Compared with the general image intensity in Eq.74, the image intensity for the Fraunhofer region as depicted in Eq.77 is much more tractable and shows a direct functional relationship with the source intensity and the hologram.

3. In the Fresnel region

In the Fresnel (*i.e.* near-field) region, approximations cannot be made for the quadratic term in Eq.73, which can be re-written as:

$$\Phi(\Delta\xi, \Delta\nu, \xi_2, \nu_2) = \begin{pmatrix} \exp\left(j\bar{k}\dfrac{d_1 + d_2}{d_1 d_2}\dfrac{(\Delta\xi)^2 + (\Delta\nu)^2}{2}\right) \\ \exp\left(j\bar{k}\dfrac{d_1 + d_2}{d_1 d_2}(\xi_2\Delta\xi + \nu_2\Delta\nu)\right) \end{pmatrix} \quad \text{Eq.78}$$

Substituting Eq.78 into Eq.74, the following expression for the image intensity in the Fresnel region is obtained:

$$J_{Fres}(\mathrm{I}) = \frac{1}{d_1^2 d_2^2}\iint_{\Delta\xi,\Delta\nu} \begin{pmatrix} \check{I}\left(\dfrac{\bar{k}}{d_1}\Delta\xi, \dfrac{\bar{k}}{d_1}\Delta\nu\right) G(\Delta\xi, \Delta\nu) \\ \exp\left(j\bar{k}\dfrac{d_1 + d_2}{d_1 d_2}\dfrac{(\Delta\xi)^2 + (\Delta\nu)^2}{2}\right) \\ \exp\left(-\dfrac{j\bar{k}}{d_2}(u_{\mathrm{I}}\Delta\xi + v_{\mathrm{I}}\Delta\nu)\right) \end{pmatrix} d\,\Delta\xi\, d\,\Delta\nu \quad \text{Eq.79}$$

$$= \frac{1}{d_1^2 d_2^2}\mathcal{F}_{\frac{\bar{k}}{d_2}u_{\mathrm{I}}, \frac{\bar{k}}{d_2}v_{\mathrm{I}}}\left\{\check{I}\left(\frac{\bar{k}}{d_1}\Delta\xi, \frac{\bar{k}}{d_1}\Delta\nu\right) G(\Delta\xi, \Delta\nu)\exp\left(j\bar{k}\frac{d_1 + d_2}{d_1 d_2}\frac{(\Delta\xi)^2 + (\Delta\nu)^2}{2}\right)\right\}$$

Where the function $G(\Delta\xi, \Delta\nu)$ is defined as follows:

$$G(\Delta\xi, \Delta\nu) = \iint_{\xi_2,\nu_2} \begin{pmatrix} K(\xi_2 + \Delta\xi, \nu_2 + \Delta\nu)K^*(\xi_2, \nu_2) \\ \exp\left(j\bar{k}\dfrac{d_1 + d_2}{d_1 d_2}(\xi_2\Delta\xi + \nu_2\Delta\nu)\right) \end{pmatrix} d\xi_2\, d\nu_2 \quad \text{Eq.80}$$

As can be seen in Eq.79, the function $G(\Delta\xi, \Delta\nu)$ contains all the information about the hologram, but Eq.80 shows that it does not have a mathematically closed form, that makes it a simple function of the hologram. As such, the formula in Eq.79 cannot be reduced into, and consequently the physical set up in Figure 28 cannot offer, a closed-form relationship between the input intensity, the hologram and the image intensity.

B. Propagation in a two-lens configuration

The formula for the image intensity in the Fresnel region as seen in Eq.79 differs from that for the intensity in the Fraunhofer region in Eq.77 by a quadratic term, which hinders algebraic simplification. This hints to the inclusion of lenses into the propagation path to eliminate such quadratic terms (cf. [76].)

The Fraunhofer solution is valid for cases where the distances d_1 and d_2 are infinitely large. In geometric optics, such scenarios are equivalent to the cases where the beams are well parallelised and the rays are asymptotically parallel to each other. To bring the images from infinity back to more realistic distances, the geometric-optics solution is to use convex lenses to collect and focus the parallelised beams into planar images (see Figure 29.)

In this section, a rigorous analysis is presented for the propagation from the source plane to the image plane, via two lenses and a hologram as set up in Figure 29. Although the final results appear similar to those expected by Fourier optics (*cf.* [76]), this analysis is significant in proving that those results are applicable for partially-coherent systems, where

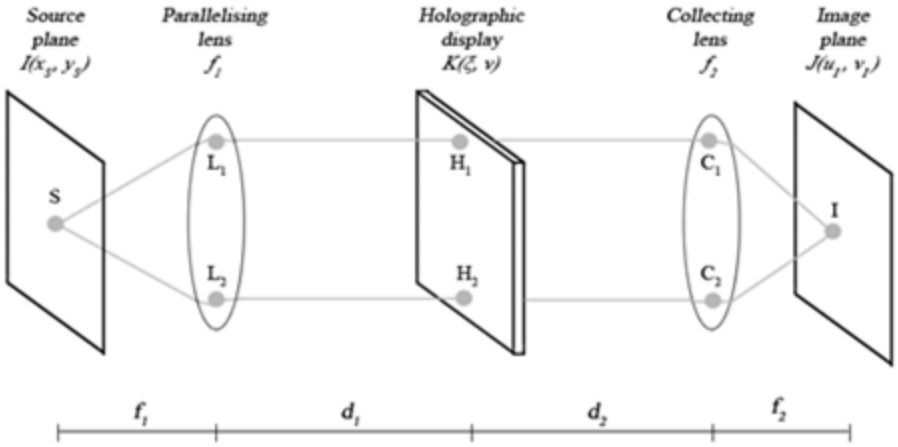

Figure 29. Schematic of the two-lens holographic propagation

the input wave-front is not planar and the final image is detected as intensity distribution (rather than a field distribution as in [76].)

The inclusion of the lenses requires the analysis of the new intermediate propagation. By putting a convex lens with focal length f_1 between the source plane and the hologram plane such that the source plane and a focal plane of the lens coincide, the mutual intensity immediately after this parallelising lens can be written as: (where $(\theta, \vartheta) \equiv \mathrm{L}$)

$$J(\mathrm{L}_1, \mathrm{L}_2) \cong \iint_{x_\mathrm{S}, y_\mathrm{S}} \left(\begin{array}{c} I(x_\mathrm{S}, y_\mathrm{S}) \frac{1}{f_1^2} \\ \exp\left(-j\bar{k} \left(x_\mathrm{S} \frac{\theta_1 - \theta_2}{f_1} + y_\mathrm{S} \frac{\vartheta_1 - \vartheta_2}{f_1} \right) \right) \\ T_1(\mathrm{L}_1) T_1^*(\mathrm{L}_2) \exp\left(j\bar{k} \frac{(\theta_1^2 + \vartheta_1^2) - (\theta_2^2 + \vartheta_2^2)}{2f_1} \right) \end{array} \right) dx_\mathrm{S}\, dy_\mathrm{S} \qquad \text{Eq.81}$$

Where $T_1(\mathrm{L})$ is the transfer function of the lens, given as [76]

$$T_1(\mathrm{L}) = \exp\left(-j\bar{k} \frac{(\theta^2 + \vartheta^2)}{2f} \right) \qquad \text{Eq.82}$$

Thus, $T_1(\mathrm{L}_1) T_1^*(\mathrm{L}_2)$ cancels out the quadratic term in the integrand of Eq.81, and simplifies the mutual intensity $J(\mathrm{L}_1, \mathrm{L}_2)$ into:

$$J(\mathrm{L}_1, \mathrm{L}_2) \cong \frac{1}{f_1^2} \tilde{I}\left(\frac{\bar{k}\Delta\theta}{f_1}, \frac{\bar{k}\Delta\vartheta}{f_1} \right) \qquad \text{Eq.83}$$

Applying the van Cittert—Zernike theorem for the propagation between the parallelising lens and the hologram plane, the mutual intensity immediately before the hologram is: (where $r_1 = \mathrm{L}_1\mathrm{H}_1, r_2 = \mathrm{L}_2\mathrm{H}_2$)

$$J(\mathrm{H}_1, \mathrm{H}_2) \cong \iint_{\mathrm{L}_1, \mathrm{L}_2} J(\mathrm{L}_1, \mathrm{L}_2) \frac{e^{j\bar{k}(r_1 - r_2)}}{r_1 r_2} d\mathrm{L}_1\, d\mathrm{L}_2 \qquad \text{Eq.84}$$

Using a similar approximation as in Eq.68, the quadratic phase in Eq.84 can be approximated as: (where $(\xi, \nu) \equiv \mathrm{H}$)

$$(r_1 - r_2) \cong (\Delta\xi - \Delta\theta)\big((\Delta\xi + 2\xi_2) - (\Delta\theta + 2\theta_2)\big) + (\Delta\nu - \Delta\vartheta)\big((\Delta\nu + 2\nu_2) - (\Delta\vartheta + 2\vartheta_2)\big) \qquad \text{Eq.85}$$

By substituting Eq.85 into Eq.84, assuming paraxiality and neglecting the quadratics of the deltas, the mutual intensity immediately before the hologram plane can be evaluated by separation of variables as follows:

$$J(\mathrm{H}_1, \mathrm{H}_2) \cong \iint_{\Delta\mathrm{L}, \mathrm{L}_2} \begin{pmatrix} \frac{1}{f_1^2 d_1^2} \tilde{I}\left(\frac{\bar{k}\Delta\theta}{f_1}, \frac{\bar{k}\Delta\vartheta}{f_1}\right) \\ \exp\left(j\bar{k}\frac{(\Delta\xi - \Delta\theta)(\xi_2 - \theta_2)}{d_1}\right) \\ \exp\left(j\bar{k}\frac{(\Delta\nu - \Delta\vartheta)(\nu_2 - \vartheta_2)}{d_1}\right) \end{pmatrix} d\Delta\mathrm{L}\, d\mathrm{L}_2$$

$$= \iint_{\theta_2, \vartheta_2} \begin{pmatrix} \frac{1}{f_1^2 d_1^2} \exp\left(j\bar{k}\frac{\Delta\xi(\xi_2 - \theta_2) + \Delta\nu(\nu_2 - \vartheta_2)}{d_1}\right) \\ \iint_{\Delta\theta, \Delta\vartheta} \begin{pmatrix} \tilde{I}\left(\frac{\bar{k}\Delta\theta}{f_1}, \frac{\bar{k}\Delta\vartheta}{f_1}\right) \\ \exp\left(-j\frac{\bar{k}\Delta\theta}{f_1}\frac{f_1(\xi_2 - \theta_2)}{d_1}\right) \\ \exp\left(-j\frac{\bar{k}\Delta\vartheta}{f_1}\frac{f_1(\nu_2 - \vartheta_2)}{d_1}\right) \end{pmatrix} d\Delta\theta\, d\Delta\vartheta \end{pmatrix} d\theta_2\, d\vartheta_2 \qquad \text{Eq.86}$$

$$= \frac{1}{\bar{k}^2 d_1^2} \iint_{\theta_2, \vartheta_2} \begin{pmatrix} I\left(\frac{f_1(\theta_2 - \xi_2)}{d_1}, \frac{f_1(\vartheta_2 - \nu_2)}{d_1}\right) \\ \exp\left(-j\bar{k}\frac{\Delta\xi(\theta_2 - \xi_2) + \Delta\nu(\vartheta_2 - \nu_2)}{d_1}\right) \end{pmatrix} d\theta_2\, d\vartheta_2$$

$$= \frac{1}{\bar{k}^2 f_1^2} \tilde{I}\left(\frac{\bar{k}\Delta\xi}{f_1}, \frac{\bar{k}\Delta\nu}{f_1}\right)$$

Comparing the mutual intensity in Eq.86 with that obtained for the no-lens case in Eq.70, it is obvious that the inclusion of the parallelising lens helps eliminate the quadratic term $\exp\left(j\bar{k}\frac{(\xi_1^2+\nu_1^2)-(\xi_2^2+\nu_2^2)}{2d_1}\right)$ already, which agrees with the analysis in [76].

Using Eq.86, the mutual intensity immediately after the hologram plane is thus:

$$J'(\mathrm{H}_1,\mathrm{H}_2) = \frac{1}{\bar{k}^2 f_1^2} K(\mathrm{H}_1)K^*(\mathrm{H}_2)\breve{I}\left(\frac{\bar{k}\Delta\xi}{f_1},\frac{\bar{k}\Delta\nu}{f_1}\right) \qquad \text{Eq.87}$$

Again, applying the van Cittert—Zernike theorem for the hologram-collecting lens propagation, the mutual intensity before the collecting lens is: (where $s_1 = \mathrm{H}_1\mathrm{C}_1$, $s_2 = \mathrm{H}_2\mathrm{C}_2$)

$$J(\mathrm{C}_1,\mathrm{C}_2) \cong \iint\limits_{\mathrm{H}_1,\mathrm{H}_2} J'(\mathrm{H}_1,\mathrm{H}_2)\frac{e^{j\bar{k}(s_1-s_2)}}{s_1 s_2} d\mathrm{H}_1\, d\mathrm{H}_2 \qquad \text{Eq.88}$$

Using Eq.68 for the quadratic approximation of distances, the intensity distribution at the back focal-plane of the collecting lens (focal length f_2) is: (with $(\zeta,\eta) \equiv \mathrm{C}$, $(u_\mathrm{I}, v_\mathrm{I}) \equiv \mathrm{I}$)

$$J(\mathrm{I}) = \frac{1}{f_2^2}\iint\limits_{\mathrm{C}_1,\mathrm{C}_2}\left(\begin{matrix} J(\mathrm{C}_1,\mathrm{C}_2)\exp\left(-j\bar{k}\left(u_\mathrm{I}\frac{\zeta_1-\zeta_2}{f_2}+v_\mathrm{I}\frac{\eta_1-\eta_2}{f_2}\right)\right) \\ \exp\left(j\bar{k}\frac{(\zeta_1^2+\zeta_1^2)-(\eta_2^2+\eta_2^2)}{2f_2}\right)T_2(\mathrm{C}_1)T_2^*(\mathrm{C}_2)\end{matrix}\right) d\mathrm{C}_1\, d\mathrm{C}_2 \qquad \text{Eq.89}$$

As with the parallelising lens, the term $T_2(\mathrm{C}_1)T_2^*(\mathrm{C}_2)$ cancels out the quadratic term of the propagation, simplifying Eq.89 into:

$$J(\mathrm{I}) = \frac{1}{f_2^2}\iint\limits_{\mathrm{C}_1,\mathrm{C}_2} J(\mathrm{C}_1,\mathrm{C}_2)\exp\left(-j\bar{k}\left(u_\mathrm{I}\frac{\Delta\zeta}{f_2}+v_\mathrm{I}\frac{\Delta\eta}{f_2}\right)\right) d\mathrm{C}_1\, d\mathrm{C}_2 \qquad \text{Eq.90}$$

Substituting $J(\mathrm{C}_1,\mathrm{C}_2)$ from Eq.88 into Eq.90 and expanding the quadratic phase, the integral part $G(\mathrm{I})$ of the image intensity $J(\mathrm{I})$ can be evaluated in the following steps with separation of variables:

$$G(\mathrm{I}) = \iint_{\Delta\mathrm{C},\mathrm{C}_2} \iint_{\Delta\mathrm{H},\mathrm{H}_2} \begin{pmatrix} \frac{1}{d_2^2} \tilde{I}\left(\frac{\bar{k}\Delta\xi}{f_1}, \frac{\bar{k}\Delta\nu}{f_1}\right) K(\Delta\mathrm{H} + \mathrm{H}_2) K^*(\mathrm{H}_2) \\ \exp\left(-j\bar{k}\left(u_\mathrm{I}\frac{\Delta\zeta}{f_2} + v_\mathrm{I}\frac{\Delta\eta}{f_2}\right)\right) \\ \exp\left(j\bar{k}\frac{(\Delta\xi - \Delta\zeta)(\xi_2 - \zeta_2)}{d_2}\right) \\ \exp\left(j\bar{k}\frac{(\Delta\nu - \Delta\eta)(\nu_2 - \eta_2)}{d_2}\right) \end{pmatrix} \begin{pmatrix} d\Delta\mathrm{H} \\ d\mathrm{H}_2 \\ d\Delta\mathrm{C} \\ d\mathrm{C}_2 \end{pmatrix}$$

$$= \iiint_{\Delta\mathrm{H},\mathrm{H}_2,\Delta\mathrm{C}} \begin{pmatrix} \begin{pmatrix} \frac{1}{d_2^2} \tilde{I}\left(\frac{\bar{k}\Delta\xi}{f_1}, \frac{\bar{k}\Delta\nu}{f_1}\right) K(\Delta\mathrm{H} + \mathrm{H}_2) K^*(\mathrm{H}_2) \\ \exp\left(-j\bar{k}\left(u_\mathrm{I}\frac{\Delta\zeta}{f_2} + v_\mathrm{I}\frac{\Delta\eta}{f_2}\right)\right) \end{pmatrix} \\ \int_{C_2 - P_2} \begin{pmatrix} \exp\left(j\frac{\bar{k}(\Delta\zeta - \Delta\xi)}{d_2}(\zeta_2 - \xi_2)\right) \\ \exp\left(j\frac{\bar{k}(\Delta\eta - \Delta\nu)}{d_2}(\eta_2 - \nu_2)\right) \end{pmatrix} \begin{pmatrix} d(\zeta_2 - \xi_2) \\ d(\eta_2 - \nu_2) \end{pmatrix} \end{pmatrix} \begin{pmatrix} d\Delta\mathrm{C} \\ d\mathrm{H}_2 \\ d\Delta\mathrm{H} \end{pmatrix}$$

Eq.91

$$= \iint_{\Delta\mathrm{H},\mathrm{H}_2} \begin{pmatrix} \frac{1}{\bar{k}^2} \tilde{I}\left(\frac{\bar{k}\Delta\xi}{f_1}, \frac{\bar{k}\Delta\nu}{f_1}\right) K(\Delta\mathrm{H} + \mathrm{H}_2) K^*(\mathrm{H}_2) \\ \int_{\Delta C} \begin{pmatrix} \exp\left(-j\left(\frac{u_\mathrm{I} d_2}{f_2}\frac{\bar{k}\Delta\zeta}{d_2} + \frac{v_\mathrm{I} d_2}{f_2}\frac{\bar{k}\Delta\eta}{d_2}\right)\right) \\ \delta\left(\frac{\bar{k}(\Delta\zeta - \Delta\xi)}{d_2}, \frac{\bar{k}(\Delta\eta - \Delta\nu)}{d_2}\right) \end{pmatrix} d\frac{\bar{k}\Delta\zeta}{d_2} d\frac{\bar{k}\Delta\eta}{d_2} \end{pmatrix} d\mathrm{H}_2\, d\Delta\mathrm{H}$$

$$= \int_{\Delta\mathrm{H}} \begin{pmatrix} \frac{1}{\bar{k}^2} \tilde{I}\left(\frac{\bar{k}\Delta\xi}{f_1}, \frac{\bar{k}\Delta\nu}{f_1}\right) \exp\left(-j\bar{k}\left(u_\mathrm{I}\frac{\Delta\xi}{f_2} + v_\mathrm{I}\frac{\Delta\nu}{f_2}\right)\right) \\ \int_{\mathrm{H}_2} K(\Delta\mathrm{H} + \mathrm{H}_2) K^*(\mathrm{H}_2)\, d\mathrm{H}_2 \end{pmatrix} d\Delta\mathrm{H}$$

$$= \frac{1}{\bar{k}^2} \iint_{\Delta\xi,\Delta\nu} \begin{pmatrix} \tilde{I}\left(\frac{\bar{k}}{f_1}\Delta\xi, \frac{\bar{k}}{f_1}\Delta\nu\right) R_{KK}(\Delta\xi, \Delta\nu) \\ \exp\left(-j\left(\frac{\bar{k}u_\mathrm{I}}{f_2}\Delta\xi + \frac{\bar{k}v_\mathrm{I}}{f_2}\Delta\nu\right)\right) \end{pmatrix} d\,\Delta\xi\, d\,\Delta\nu$$

The last result in Eq.91 is the Fourier Transform of $\check{I}\left(\frac{\bar{k}}{f_1}\Delta\xi, \frac{\bar{k}}{f_1}\Delta\nu\right) R_{KK}(\Delta\xi, \Delta\nu)$. Therefore, the image intensity can also be expressed as a Fourier Transform:

$$J(\mathrm{I}) = \frac{1}{\bar{k}^4 f_1^2 f_2^2} \mathcal{F}_{\frac{k}{f_2}u_\mathrm{I}, \frac{k}{f_2}v_\mathrm{I}} \left\{ \check{I}\left(\frac{\bar{k}}{f_1}\Delta\xi, \frac{\bar{k}}{f_1}\Delta\nu\right) R_{KK}(\Delta\xi, \Delta\nu) \right\} = \\ = \frac{1}{\bar{k}^6 f_2^2} \tilde{R}_{KK}\left(\frac{\bar{k}}{f_2}\mathrm{I}\right) * I\left(-\frac{f_1}{f_2}\mathrm{I}\right) \qquad \text{Eq.92}$$

This formulation is almost identical to that for the image intensity in the Fraunhofer region without lenses (*cf*. Eq.77), except for the different scaling factors. Thus, Eq.92 can be used to model the image intensity in both the Fraunhofer and Fresnel regions.[††]

It can be seen from Eq.92 that any hologram $K(\xi, \nu)$ that successfully steers a point-source beam (a Kronecker delta in the ideal case) to I_n, also offers similar steering capacity with a source of a different intensity distribution. This can be shown mathematically as a convolution between the point-source image intensity $J(\mathrm{I})$ and the true input intensity distribution $I(x, y)$:

$$J(\mathrm{I}) = \frac{1}{\bar{k}^6 f_2^2} \tilde{R}_{KK}\left(\frac{\bar{k}}{f_2}\mathrm{I}\right) * I\left(-\frac{f_1}{f_2}\mathrm{I}\right) = J(\mathrm{I}) * I\left(-\frac{f_1}{f_2}\mathrm{I}\right) \qquad \text{Eq.93}$$

Therefore, the hologram search can be performed with a point source, and it still works when used with a different source distribution. It also means that a hologram that successfully steers one source also gives the same steering performance with any other sources.

However, it must be noted that: since Eq.92 is derived for partially coherent propagation whilst a point-source is spatially coherent, Eq.93 is only mathematically correct and useful in

[††] It should be noted that Eq.92 can be derived in a less rigorous manner by marrying a geometric-optic treatment of the 4-*f* correlator[76] J. W. Goodman, *Introduction to Fourier Optics*, 2nd ed. Singapore: McGraw-Hill, 1996. with the result presented in [75] M. Born and E. Wolf, *Principles of optics: Electromagnetic theory of propagation, interference and diffraction of light*, 7th ed. Cambridge: Cambridge University Press, 1999..

obtaining the desired hologram, whilst not useful in simulating propagation in physical systems.

The significance of the result in Eq.92 is that, given a simple and realistic 2-lens set-up, the image intensity distribution in the image plane can be easily calculated using the known distributions at the hologram plane only, without any propagation to the image plane.

For a given input and a desired output, Eq.92 and Eq.93 only offer the continuous autocorrelation function as solution. This continuous autocorrelation will have to be translated into a discrete hologram for digital display devices. To minimise quantisation errors, the simplest solution to this translation is to carry out a hologram search. The next section proposes two criteria and corresponding algorithms for such a search operation.

C. Proposed algorithms for hologram search

Figure 30 depicts the flowchart of the direct-binary-search as the hologram-generation algorithm [38, 54, 58, 59, 61, 63, 65]. It requires a new replay to be calculated for every hologram pixel-change using a four-dimensional integration to propagate light from the source plane to the image plane (*cf*. Eq.74.) This computationally costly calculation can be avoided by using Eq.91 to move the comparison target from the image plane to the hologram plane, thus forming a new iterative hologram-search algorithm type which only require the propagation of the desired image to the hologram plane.

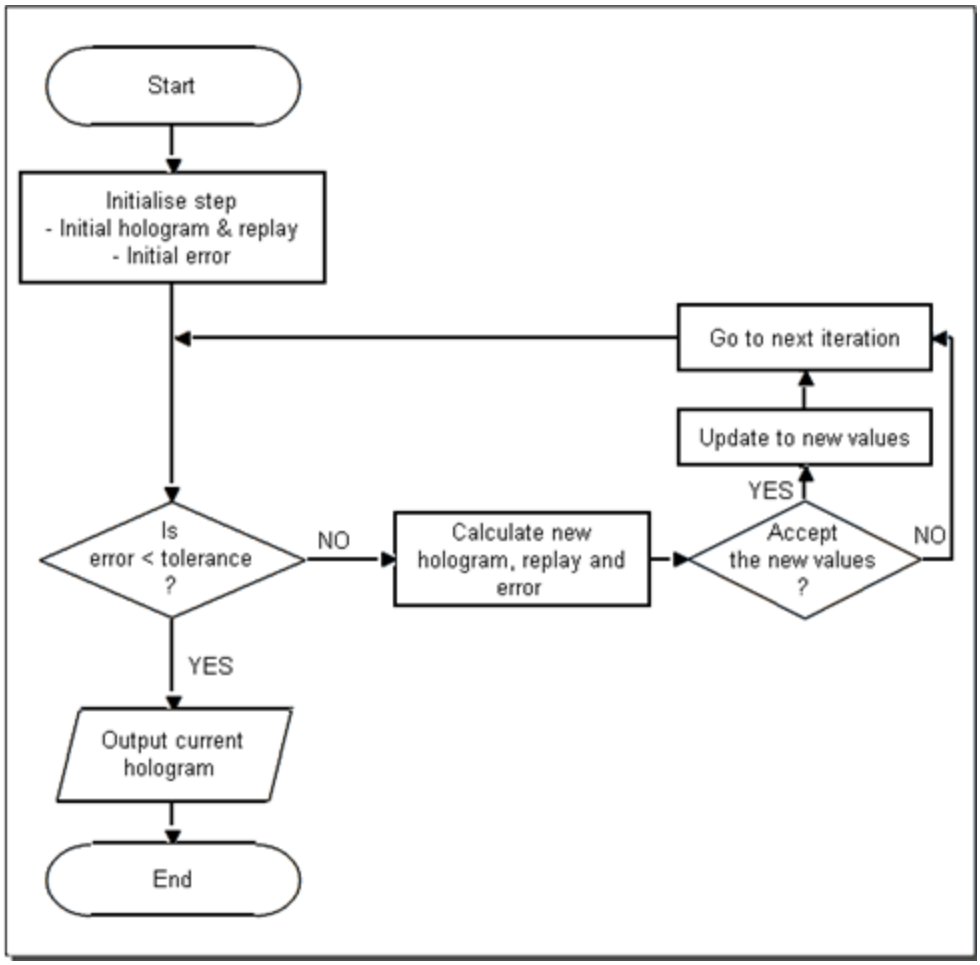

Figure 30. Flow-chart for direct binary search

1. Cost function for new hologram-search

A hologram search is an optimisation process through which the different holograms are iteratively assessed by a given cost function to find the hologram that gives the best performance. Given the importance of the cost function as criterion to determine a hologram's performance, it can be seen that different cost-functions give rise to different search-algorithms, even when using the same underlying iterating structure.

The generic cost function for any search algorithms can be written as a function of the difference between the current search state Ψ, and the desired state Ψ_d:

$$e(\Psi) \equiv f(\Psi - \Psi_d) \qquad \text{Eq.94}$$

From Eq.92, it can be seen that for a given source intensity distribution $I(x, y)$ in a system with fixed parameters (hence the constants in Eq.92 are fixed), the image intensity is a function only of the autocorrelation function R_{KK} of the hologram K. Therefore, the search for a hologram that gives the desired image intensity can also be interpreted as the search for a hologram whose autocorrelation function is closest to a desired autocorrelation.

This points to two directions for developing the cost functions: the first is to use the image intensity $J(\mathrm{I})$ directly as the state Ψ in Eq.94; whilst the second is to use the autocorrelation function R_{KK} as Ψ. Each cost function formulated from these development directions will become a different search criterion, and as discussed, give rise to a corresponding search algorithm.

In this analysis, the aim is to compare the performance of autocorrelation-based differences and those based on the full image-intensities. Therefore the form of $f(\cdot)$ in Eq.94 is taken as the simple mean of squared differences between two distributions, and its

optimisation is the well-known minimum mean-squared-errors (MMSE) process. Other cost-functions have been studied elsewhere (*e.g.* [61-63, 104].)

a. ACF criterion – Hologram autocorrelation as search state

Replacing the state Ψ in Eq.94 with the autocorrelation function R_{KK} of the hologram K, the cost function as the mean of squared differences can be expressed as:

$$e(R) \equiv \iint_{\alpha,\beta} \left| R_{KK}(\alpha,\beta) - R_{KK_d}(\alpha,\beta) \right|^2 d\alpha d\beta \qquad \text{Eq.95}$$

Using the relationship developed in Eq.92, $R_{KK}(\alpha,\beta)$ can be expressed as:

$$R_{KK}(\alpha,\beta) = \bar{k}^6 f_1^2 \frac{\mathcal{J}\left(-\frac{\bar{k}}{f_2}\alpha, -\frac{\bar{k}}{f_2}\beta\right)}{\mathcal{I}\left(\frac{\bar{k}}{f_1}\alpha, \frac{\bar{k}}{f_1}\beta\right)} \qquad \text{Eq.96}$$

Substituting Eq.96 into Eq.95, it can be seen that the cost function becomes:

$$e(R) \equiv \bar{k}^6 f_1^2 \iint_{\alpha,\beta} \left| \frac{\mathcal{J}\left(-\frac{\bar{k}}{f_2}\alpha, -\frac{\bar{k}}{f_2}\beta\right) - \mathcal{J}_d\left(-\frac{\bar{k}}{f_2}\alpha, -\frac{\bar{k}}{f_2}\beta\right)}{\mathcal{I}\left(\frac{\bar{k}}{f_1}\alpha, \frac{\bar{k}}{f_1}\beta\right)} \right|^2 d\alpha d\beta \qquad \text{Eq.97}$$

Since two functions with identical Fourier transforms are identical, Eq.97 thus shows that $e(R)$ based directly on the autocorrelation function R_{KK} as expressed in Eq.95 does give a measurement of similarity between the current image intensity and the target intensity. Consequently, $e(R)$ is a valid cost function for the hologram search and will be known as the ACF criterion.

b. IMG criterion – Image intensity as search state

The cost function is defined as the mean of squared differences between the current image intensity $J(\mathrm{I})$ and the desired distribution $J_d(\mathrm{I})$:

$$e(J) \equiv const \int_{\mathrm{I}} |\bar{J}(\mathrm{I}) - \bar{J}_d(\mathrm{I})|^2 \, d\mathrm{I} \qquad \text{Eq.98}$$

Where $\bar{J}(\mathrm{I})$ is the normalised intensity distribution, defined as:

$$\bar{J}(\mathrm{I}) \equiv \frac{J(\mathrm{I})}{\int_{\mathrm{I}} J(\mathrm{I}) \, d\mathrm{I}} \qquad \text{Eq.99}$$

Neglecting the constant, the integral in Eq.98 can be expressed using Parseval's theorem as: (where $\tilde{\bar{J}}(\mathrm{Z})$ is the Fourier Transform of $\bar{J}(\mathrm{I})$)

$$e(J) = \int_{\mathrm{Z}} \left|\tilde{\bar{J}}(\mathrm{Z}) - \tilde{\bar{J}}_d(\mathrm{Z})\right|^2 d\mathrm{Z} \qquad \text{Eq.100}$$

From the definition in Eq.99, the Fourier-domain function $\tilde{\bar{J}}(\mathrm{Z})$ takes the form:

$$\tilde{\bar{J}}(\mathrm{Z}) = \mathcal{F}\left\{\frac{J(\mathrm{I})}{\int_{\mathrm{I}} J(\mathrm{I}) \, d\mathrm{I}}\right\} = \frac{\mathcal{F}\{J(\mathrm{I})\}}{\int_{\mathrm{I}} J(\mathrm{I}) \, d\mathrm{I}} = \frac{\tilde{J}(\mathrm{Z})}{\int_{\mathrm{I}} J(\mathrm{I}) \, d\mathrm{I}} = \frac{\tilde{J}(\mathrm{Z})}{\tilde{J}(0,0)} \qquad \text{Eq.101}$$

Substituting Eq.101 in to Eq.100, the cost function becomes:

$$e(J) = \int_{\mathrm{Z}} \left|\frac{\tilde{J}(\mathrm{Z})}{\tilde{J}(0,0)} - \frac{\tilde{J}_d(\mathrm{Z})}{\tilde{J}_d(0,0)}\right|^2 d\mathrm{Z} \qquad \text{Eq.102}$$

From Eq.92, $\tilde{J}(\alpha,\beta)$ as the Fourier Transform of the image intensity can be expressed:

$$\tilde{J}(\alpha,\beta) = \frac{f_2^2}{\bar{k}^6 f_1^4} \tilde{I}\left(-\frac{f_2}{f_1}\alpha, -\frac{f_2}{f_1}\beta\right) R_{KK}\left(-\frac{f_2}{\bar{k}}\alpha, -\frac{f_2}{\bar{k}}\beta\right) \qquad \text{Eq.103}$$

Substituting Eq.103 into Eq.102, the cost function, as a function of the hologram autocorrelation, then takes the form:

$$e(R) = e(J) = \int_{\alpha,\beta} \left| \frac{\breve{I}\left(-\frac{f_2}{f_1}\alpha, -\frac{f_2}{f_1}\beta\right) R_{KK}\left(-\frac{f_2}{\bar{k}}\alpha, -\frac{f_2}{\bar{k}}\beta\right)}{\breve{I}(0,0) R_{KK}(0,0)} - \frac{\breve{J}_d(\alpha,\beta)}{\breve{J}_d(0,0)} \right|^2 d\alpha d\beta \quad \text{Eq.104}$$

Eq.104 shows that the cost function based directly on image intensities can be expressed as that of scaled autocorrelation functions. Thus, an appropriately scaled autocorrelation function can be taken as proxy for the image intensity in the hologram search process.

The search algorithm using Eq.104 as the fitting criterion (named the IMG criterion) will be referred to as the IMG algorithm

2. Hologram-search algorithms

a. Architecture of the algorithms

Figure 30 depicts the flow-chart describing the architecture of the hologram-generating algorithms using the autocorrelation-based ACF and IMG cost-functions.

The algorithm starts with taking in the intensity distribution I of the source, and the desired intensity distribution J_d for the image as input arrays. From these, the desired

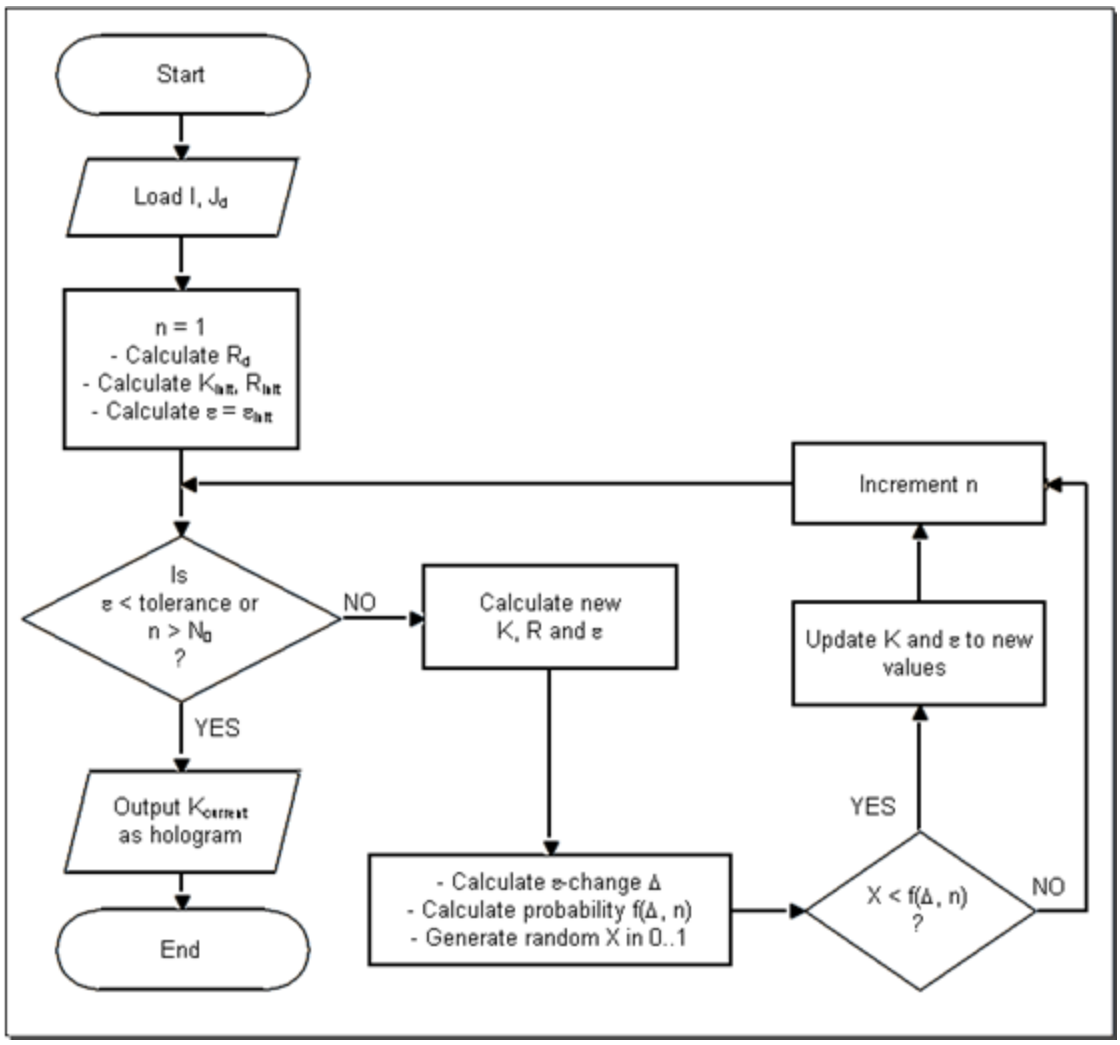

Figure 31. Flow-chart for the autocorrelation-based algorithms

hologram autocorrelation R_{d} can be calculated from Eq.92. These distributions are stored as pre-loaded and pre-calculated array constants.

As part of the initialisation phase, the algorithm also initialises the hologram K to a random state K_{init} of a binary-phase array, and calculates the corresponding autocorrelation[‡‡] R_{init} of this hologram. From this R_{init} and the pre-calculated R_{d}, depending on the algorithm and its respective cost-function as discussed in Chapter IV, an initial value $\varepsilon_{\mathrm{init}}$ of the search error is calculated. If this value is smaller than a certain constant which represents the algorithm's tolerance for differences between the realisable quantised hologram and the desired one, K_{init} is output as the search result. The algorithm then stops.

If the initial error is larger than the tolerance constant, then the algorithm enters the iteration phase where each iterative loop has two steps—proposal step and evaluation step—in order to decide if the hologram needs to be updated.

In the proposal step, a hologram K_{proposed} is generated, differing from the current hologram by one pixel. The corresponding autocorrelation R_{proposed} and the search error $\varepsilon_{\mathrm{proposed}}$ of this proposed hologram are obtained.

In the evaluation step, an evaluation metric Δ is calculated from $\varepsilon_{\mathrm{proposed}}$, which is the signed difference between $\varepsilon_{\mathrm{proposed}}$ and the search error $\varepsilon_{\mathrm{current}}$ for the current hologram. An acceptance probability $f(\Delta, n)$ is also calculated by a simulated-annealing algorithm for this current iteration (indexed as n.) A random variable is then sampled from the uniform distribution between 0 and 1: if this variable is smaller than $f(\Delta, n)$, the current hologram is updated to the new value of K_{proposed}. Otherwise, the current hologram retains the value it

[‡‡] The autocorrelation is calculated using circular convolution to account for the effect of hologram-padding in the experiment with the SLM—see Chapter VI.B.2.

has at the start of this current loop. The iteration index n is incremented regardless of the evaluation decision.

In order to determine whether another iteration is needed, the error value for the current hologram (new if updated) is again compared with the tolerance constant. If the error is smaller than the tolerance, then the algorithm outputs the current hologram as the search result before stopping. Otherwise, the algorithm enters a new iteration of the loop.

To avoid infinite looping, an upper limit for the number of iterations is set, which is the constant N_0 as discussed in Chapter IV. This limit is taken as a multiple of the number of hologram pixels N so that each hologram pixel is evaluated the same number of times for potential update. Once the index n reaches the upper limit of N_0, the search terminates, the algorithm outputs the current hologram and stops.

The algorithms based on this architecture and using the autocorrelation-based criteria are named, according to the corresponding criteria, the ACF and the IMG algorithms.

b. Probabilistic hologram-search with simulated annealing

The hologram-generation algorithms have an optimisation process as the core. Deterministic gradient-based optimisation techniques suffer from the impossibility to escape local minima once trapped and thus works only with convex functions [105]. For a function whose convexity is either theoretically or empirically not guaranteed or unknown, stochastic optimisation offers a convenient solution to the local-minimum traps [106]. The idea is that the move from one state to another always has a non-zero probability. Thus it is still possible for the optimiser to escape local minima to neighbouring states despite their higher values.

One of such techniques, simulated annealing [1] varies the probability P_{accept} of accepting a new state according to an improvement metric Δ, and a monotonically-decreasing non-negative scheduling parameter T. The probability function proposed in [1] is found to give unsatisfactory termination to the search due to its very low probability of accepting non-improving new states throughout the range of T. A new probability function is developed for these autocorrelation-based algorithms. Figure 32 shows this new function of P_{accept} against Δ and T as implemented in the simulation.

The mathematical formulae for the variation in Figure 32, and the relevant control

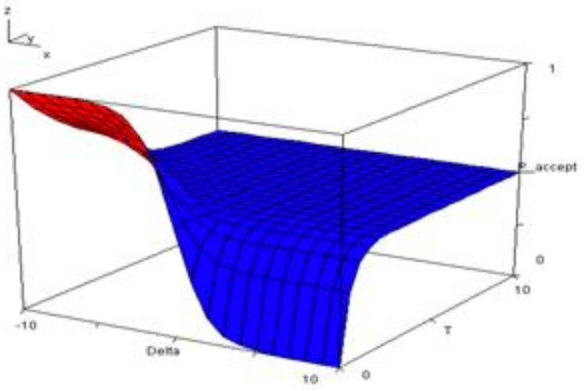

Figure 32. Variation of $\boldsymbol{P_{accept}}$ with Δ and $\boldsymbol{T}$ as used in the MATLAB simulation

values found through empirical adjustments are:

$$\begin{gathered}\Delta = e_n(\Psi) - e_{n-1}(\Psi) \\ T = 300\exp(-150\,n/N_0) \\ g_1(T) = \frac{1}{2} + \frac{1}{2}\exp(-10T)\,;\; g_2(T) = \frac{1}{2} - \frac{1}{2}\exp(-10T) \\ f(\Delta, n) = P_{accept}(\Delta, T) = \frac{g_2(T)\exp\left(\frac{\Delta}{T}\right) - g_1(T)\frac{1-2g_2(T)}{1-2g_1(T)}}{\exp\left(\frac{\Delta}{T}\right) - \frac{1-2g_2(T)}{1-2g_1(T)}}\end{gathered} \qquad \text{Eq.105}$$

Where: N_0: total number of iterations to perform in the operation; n: index of the current iteration; $e_n(\Psi)$: error value of the n^{th} iteration against the target distribution (*cf.* Chapter IV). The detailed derivation of Eq.105 can be found in Appendix A.

Once P_{accept} is calculated for the current iteration according to Eq.126, the hologram generator is faced with a probabilistic decision: it should only update the hologram to K_{proposed} with P_{accept} probability, whilst the hologram should remain unchanged with $\left(1 - P_{accept}\right)$ probability.

Towards the end of the simulation loop, the temperature T drops to a sufficiently low value that the probability P_{accept} becomes essentially 1 for negative Δ, and 0 for positive Δ (see Figure 32.) The optimisation now settles into a search for the local minimum in the vicinity of the current state, and terminates once this local minimum is found. The hologram corresponding to this local minimum is the output of the whole algorithm.

D. Time-complexity of the proposed algorithms

To evaluate the speed of execution of the proposed autocorrelation-based algorithms, a worst-case analysis is performed using the O-notation [107]. As can be seen from Eq.95 and Eq.104, the cost-function calculations for the ACF and the IMG algorithms both involve the autocorrelation function R_{KK} of the hologram K, differing only by a scaling with the Fourier transform $\tilde{I}$ of the known input intensity. Therefore, if assuming the scaling operation is computationally inexpensive and thus negligible, the two algorithms can be considered as identical in terms of complexity.

Table 2 shows the breakdowns of the expensive operations for the autocorrelation-based algorithms (both the ACF and the IMG) and for the direct binary search. These operations can

Phase	**Autocorrelation-based algorithms**	**Direct binary search**
Initialising (1 iteration)	- Calculate desired ACF from desired image (t_{forward}) - Calculate initial R_{KK} from initial K (t_{convol}) - Calculate initial value of cost function ($t_{\text{err\_calc\_acf}}$)	- Calculate initial replay field from initial K (t_{dir}) - Calculate initial value of cost function ($t_{\text{err\_calc\_dir}}$)
Optimising (N_0 iterations)	- Update R_{KK} from K (t_{convol}) - Update cost function ($t_{\text{err\_calc\_acf}}$) - Evaluate cost function (t_{eval})	- Update image from K (t_{dir}) - Update cost function ($t_{\text{err\_calc\_dir}}$) - Evaluate cost function (t_{eval})

Table 2. Computationally expensive operations of the autocorrelation-based algorithms and of the direct binary search

be grouped into the initialising phase, which are performed once, and the optimising phase, which consists of at maximum N_0 iterations. In this analysis, N_0 is taken as a multiple α of the number N of hologram pixels where $\alpha \geq 10$ to ensure good randomisation in the updating process (see Chapter V):

$$N_0 = \alpha N \qquad \text{Eq.106}$$

Scaling operations, *i.e.* multiplications and divisions, are also assumed to be computationally inexpensive.

For the autocorrelation-based algorithms, in the initialising phase, the target autocorrelation function R_{KK_d} is calculated from the target image using Eq.96. This step involves two Fourier Transforms and several scaling operations. Thus the time taken by this step is of the same order as that of the Fourier Transform—here the 2-dimensional Fast Fourier Transform (FFT2) implementation is used, whose complexity is [107]:

$$t_{\text{forward}} \cong t_{FFT2} = \mathrm{O}(N \log N) \qquad \text{Eq.107}$$

Using the Wiener-Khinchin theorem, the convolution to calculate the autocorrelation R_{KK} from the hologram K is a straightforward combination of 3 Fourier Transforms and 1 multiplication. Its time therefore is:

$$t_{\text{convol}} \cong 3t_{FFT2} = \mathrm{O}(N \log N) \qquad \text{Eq.108}$$

According to Eq.95 and Eq.104, the computation of the cost function using the current value R_{KK} of the autocorrelation function involves direct subtraction of functions, which has identical computational costs to the addition:

$$t_{\text{err\_calc\_acf}} \cong t_{sum2} = \mathrm{O}(N) \qquad \text{Eq.109}$$

From the analysis of the simulated-annealing iterating-structure (see Appendix A) the most expensive operation in evaluating the cost function for update acceptance is the several exponential functions. However, since these functions are calculated with only scalar variables, they are assumed to take negligible time compared with the multidimensional operations in the other steps. Thus for the purpose of this analysis:

$$t_{\text{eval}} \cong \text{O}(1) \qquad \text{Eq.110}$$

Therefore, the total time T_{ACF} taken by the autocorrelation-based algorithms, expressed in terms of the number of hologram pixels is:

$$\begin{aligned} T_{\text{ACF}}(N) &\cong t_{\text{forward}} + N_0 t_{\text{eval}} + (N_0+1)\left(t_{\text{convol}} + t_{\text{err}_{\text{calc}_{\text{acf}}}}\right) \\ &\cong t_{FFT2} + N_0 t_{\text{eval}} + (N_0+1)(3t_{FFT2} + t_{sum2}) \\ &= (3N_0+4)t_{FFT2} + (N_0+1)t_{sum2} + N_0 t_{\text{eval}} \\ &\cong (3N_0+4)\,\text{O}(N\log N) + (N_0+1)\,\text{O}(N) + N_0\,\text{O}(1) \\ &\cong \text{O}(N^2 \log N) \end{aligned} \qquad \text{Eq.111}$$

For direct binary search, the calculation of the image distribution from Eq.92 involves 1 convolution, 1 Fourier Transform and 1 multiplication, which equates to 4 Fourier Transforms and 2 multiplications. Again, assuming multiplications being inexpensive, the time taken for image simulation is:

$$t_{\text{dir}} \cong 4t_{FFT2} = \text{O}(N \log N) \qquad \text{Eq.112}$$

Using similar arguments as with the autocorrelation-based algorithm analysis, the cost-function calculation and evaluation times for direct binary search are:

$$\begin{aligned} t_{\text{err\_calc\_dir}} &\cong t_{sum2} = \text{O}(N) \\ t_{\text{eval}} &\cong \text{O}(1) \end{aligned} \qquad \text{Eq.113}$$

Consequently, the total time T_{DIR} taken by the direct binary search, expressed in terms of the number of hologram pixels is:

$$\begin{aligned} T_{\mathrm{DIR}}(N) &= (N_0+1)\left(t_{\mathrm{dir}} + t_{\mathrm{err}_{\mathrm{calc}_{\mathrm{dir}}}}\right) + N_0 t_{\mathrm{eval}} \\ &\cong (N_0+1)(4t_{FFT2} + t_{sum2}) + N_0 t_{\mathrm{eval}} \\ &= 4(N_0+1)t_{FFT2} + (N_0+1)t_{sum2} + N_0 t_{\mathrm{eval}} \\ &\cong 4(N_0+1)\,\mathrm{O}(N\log N) + (N_0+1)\,\mathrm{O}(N) + N_0\,\mathrm{O}(1) \\ &\cong \mathrm{O}(N^2\log N) \end{aligned} \qquad \text{Eq.114}$$

Eq.111 and Eq.114 show that this particular implementation of the direct binary search requires 1 Fourier Transform operation per iteration more than the autocorrelation-based algorithms, and thus asymptotically takes 33% longer to complete.

Should the algorithms be implemented as naïve forward propagations from the source, then the autocorrelation-based algorithms would have the forward propagation stop at the holographic plane, whilst the direct binary search would require another step of propagation to the image plane. As shown in Eq.1 to Eq.67, this would mean it would take twice as many basic operations for the direct binary search compared with the autocorrelation-based algorithms, and thus asymptotically twice as long to complete.

Note that both $T_{\mathrm{ACF}}(N)$ in Eq.111 and $T_{\mathrm{DIR}}(N)$ in Eq.114 are of the order $N\,\mathrm{O}(\mathrm{FFT})$ thus more efficient FFT algorithms will yield better time performance.

E. Conclusions

This chapter discusses the theoretical propagation of partially-coherent light through a hologram as a beam-steering technique to reduce overlapping of transmitter images and improve performance of MIMO-OWC systems. It is found that by using a two-lens configuration to parallelise and collect partially-coherent light at the source and the image respectively, a succinct mathematical relationship based on Fourier Transform can be established between three quantities: the source intensity distribution, the image intensity distribution, and the autocorrelation of the hologram.

This mathematical relationship has led to the development of two novel algorithms for computational holographic generation—the ACF and the IMG—based on the autocorrelation function to obtain a quantised hologram with the desired beam-steering capability, via a simulated-annealing process. These differ from commonly used hologram-generating algorithms in that their cost functions are all based on the autocorrelation function of the hologram, and the performance comparison is done at the hologram plane instead of the image plane. One of the advantages of these autocorrelation-based algorithms is that they likely take less time to generate the desired hologram.

To study the actual beam-steering performance of these algorithms, Chapter V will describe a simulation for the optical system developed in MATLAB. The two proposed algorithms will be individually run through the simulation to assess their viability as well as their performance, both in beam-steering capacity and in terms of the time taken. The results of such assessments are reported in the second part of Chapter V.

Chapter V. **System simulation and hologram generation**

In Chapter IV, the theoretical analysis of holographic propagation with partially-coherent light has led to the development of two computational algorithms—the ACF and the IMG—based on the autocorrelation function to obtain a quantised hologram with the desired beam-steering capability. To study the operation of these algorithms, a simulation for the optical system working with binary-phase holograms was developed in MATLAB, and is reported in this chapter. The two proposed algorithms are individually run through the simulation to assess their viability as well as their performance, both in beam-steering

capacity and in terms of the time taken. The results of such assessments are reported in the second part of this chapter.

A. MATLAB program for hologram generation and system simulation

1. Overview

To study the holographic performance of the algorithms proposed in Chapter IV, a program was developed in MATLAB. It serves as an implementation of the algorithms

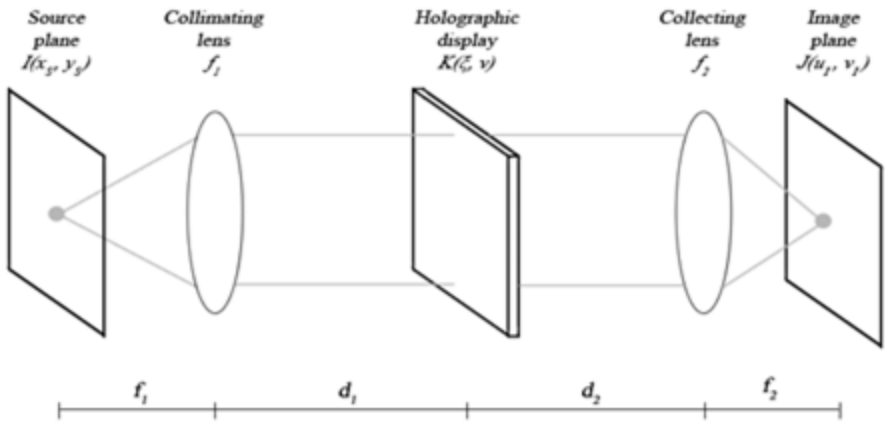

Figure 33. Schematic of the two-lens holographic system

proposed in Chapter IV, as well as to simulate a physical two-lens holographic system (*cf*. Chapter IV) through which partially-coherent light propagates and is modulated by the hologram.

Figure 33 depicts this two-lens holographic system. Partially-coherent light from the source propagates through the first lens, which parallelises the light beam onto the front side of the holographic display. The electric field of the light is modulated with the hologram placed on the display, and the modulated beam emerges at the back-plane of the display. This hologram-modulated beam then propagates to the collecting lens, and an image is created by

the lens onto the imaging screen. With a binary hologram, the image should ideally consist only of two target spots of the source placed symmetrically to either side of the unsteered source [56, 69].

Direct-binary-search algorithms work by iteratively improving the resemblance between the replay resultant from a hologram, and the desired image. Since digital displays only work with quantised holograms—the holograms are binary-phase in this simulation—whilst the ideal hologram may be continuous, there potentially are differences between the replay and the desired image. The performance of each hologram in steering the beam is judged by how closely this replay resembles the desired image for which the hologram is generated. The resemblance is assessed both by the positions of the target spots, and by the relative distribution of optical power within the replay. This straightforward criterion is the cost function implemented and optimised in direct binary search.

In the proposed autocorrelation-based algorithms, all comparisons are done at the hologram plane, where the ACF algorithm works to improve the resemblance towards an ideal hologram, and the IMG algorithm to improve the resemblance to the desired image back-propagated to the hologram plane. In other words, the desired image at the screen is projected by the collecting lens to the hologram plane, and this backward-propagated reference distribution is compared with the forward-propagated distribution from the source to the display back-plane.

Given that the only updateable element in the system is the hologram, the forward propagation from the source to the front-plane of the display can be calculated *a priori*. Consequently, the algorithms boil down to computationally looping between the front-plane distribution and the back-plane one, updating the hologram (or not) before each iteration and

comparing the distributions at the back-plane. This updating decision has been described in detail in Chapter IV.

2. Implementation

The MATLAB implementation of the algorithm includes the following operations:

1. The initial hologram K_{init} is chosen as a random 2-dimensional binary array since the simulated holographic display is binary-phase where one phase is 0 (corresponding to pixel value 1) whilst the other is π (pixel value -1).
2. The hologram proposal operates in a one-pixel-per-iteration basis and the pixel is chosen randomly for each iteration from the set of pixels not yet proposed.
3. The evaluation metric Δ is a signed difference between $\varepsilon_{\text{proposed}}$ and the error $\varepsilon_{\text{current}}$ resulting from the current hologram K_{current}. By using the relative improvement as the metric, the comparison has a quantitative result which can be used as input for acceptance evaluation. The relative improvement also helps reduce the memory load of the program as changes in variables are usually much smaller than the magnitude of the variables themselves.
4. The acceptance probability $f(\Delta, n)$ is calculated using a specific form of the simulated-annealing algorithm [1]. This optimisation algorithm affords the search a certain degree of flexibility in escaping local minima, especially at the beginning of the process.
5. The probabilistic decision is implemented such that its probabilistic element is all embodied in a random variable, and deterministic decisions are then applied on this variable. An implementation is to use a uniformly-distributed random variable X: by definition, $X \in [0, P_{accept}]$ with probability P_{accept}, whilst $X \in (P_{accept}, 1]$ with probability $(1 - P_{accept})$. Comparing X and P_{accept} therefore has the same

probability profile as required for the updating decision, and thus the updating decision can be translated into the said comparison.

These implementations are straightforward. Therefore, to help develop a program that can assess the performance of the different autocorrelation-based criteria and that will work for all cases, these implementations are used in the program's development.

B. Hologram performance metrics

To judge the performance of each algorithm, the beam-steering capability of the optimised hologram obtained from the algorithm must be assessed on two aspects: how close the steered image is to the target position, and how closely the intensity distribution of the steered image resembles that of the source.

Since the hologram is binary-phase, the replay contains duplicate copies of the target spots of interest symmetric about the unsteered source [69]. As discussed in [56], these symmetric target spots can both be exploited in communication routing, therefore both are used for performance assessment.

To extract these target spots, the image intensity distribution is run through a post-processing module, also built in MATLAB. This post-processing module performs the following operations in order:

1. First-order positions: The cross-correlation of the unsteered-source-suppressed image intensity distribution with the source intensity distribution is calculated. Since the target spots of a binary-quantised cosine [69] contain the highest power concentration, they should correspond to the highest peaks in the cross-correlation. Therefore, a simple peak search on the cross-correlation returns the pixel-positions of the centroids of the two target spots, which are given as ratios relative to the array dimensions (to account for the different pixelation.)
2. First-order power: In order to calculate the optical power contained within the target spots, they must first be extracted from the image intensity distribution which is achieved with a multiplicative mask created from shifting the unsteered source mask to the positions of the target spots. The optical power contained

within the two target spots is calculated by integrating the intensity distribution within the extracted images.

3. Optical SNR: The success of the hologram in concentrating the power into the target spots can be measured in two ways:

   - The ratio of the average intensity in the target spots to the average intensity of the rest of the field. This quantity, named Overall-SNR, is the classic optical signal-to-noise ratio (SNR) and can be straightforward to calculate from the intensity distribution $I(A)$ and the area A as:

$$SNR_{\text{Overall}} = \frac{\int_{spots} I(A).dA / \int_{spots} dA}{\int_{non-spots} I(A).dA / \int_{non-spots} dA} \qquad \text{Eq.115}$$

   - The ratio of the total power in the target spots to the total power contained in the second-most prominent features (*i.e.* the 2nd-orders). The calculation of this quantity, named Peaks-SNR, follows the same peak-extraction approach for the 2nd-orders and is defined as:

$$SNR_{\text{Peaks}} = \frac{\int_{spots} I(A).dA}{\int_{noise\ peaks} I(A).dA} \qquad \text{Eq.116}$$

   Peaks-SNR is of significance where the optical power is well concentrated into a few orders rather than spread across the image field, and is also important as a measurement of the potential cross-talk this source generates to other channels.

Thus the performance of each output hologram is measured by 6 metrics:

- Four positions: two for each target-spot in the horizontal and vertical dimensions;
- Two optical SNRs: one measured relative to the whole field (the Overall-SNR), the other relative to the next-most prominent peaks (the Peaks-SNR).

C. Initial simulation results

As a preliminary evaluation of the hologram-generating behaviour of the proposed algorithms, and to understand the operation of the MATLAB program in simulating the physical optical propagation, several holograms have been generated for each algorithm and their performance, measured with the metrics defined in Chapter V.B, is shown in this section. A full analysis, using a bigger set of holograms, of the beam-steering capability of the algorithms both in a simulated environment and in an experimental system will be presented in Chapter VI.

1. Simulation parameters

For each algorithm, square holograms of different sizes are generated using the program described in Chapter V.A. Table 3 shows the parameters used in this simulation.

System pixilation	Size of square arrays (pixel)	(ACF) 64, 128, 256, 512 (IMG) 64, 128, 256
	Desired image shift (pixel)	50 (horizontal) by 50 (vertical)
Generation loop (*cf.* Chapter IV.C.2)	Error tolerance	0
	Number of iterations	10 * (number of pixels)
	Cooling parameters	(see Eq.126)
Propagation constants (*cf.* Eq.92)	Intensity multiplier $\frac{1}{\bar{k}^6 f_2^2}$	1
	Source-plane scaling $\frac{f_1}{\bar{k}}$	1
	Image-plane scaling $\frac{f_2}{\bar{k}}$	1

Table 3. Parameters used in MATLAB simulation of the holographic system

In Table 3, since it is the relative distribution of intensity that is of interest, the intensity multiplier $1/\bar{k}^6 f_2^2$ is set at 1 for ease of computation. Also, as the Fourier Transforms in MATLAB are in different discrete domains where the spatial units are the cells of relevant arrays, these cells may represent differently-scaled physical units (*cf.* Appendix B). Consequently, the scaling factors $f_1/\bar{k}$ and $f_2/\bar{k}$ for the continuous domains in Eq.92 are unimportant, and thus set to 1.

In Figure 34, a representative source intensity distribution used in the simulation is

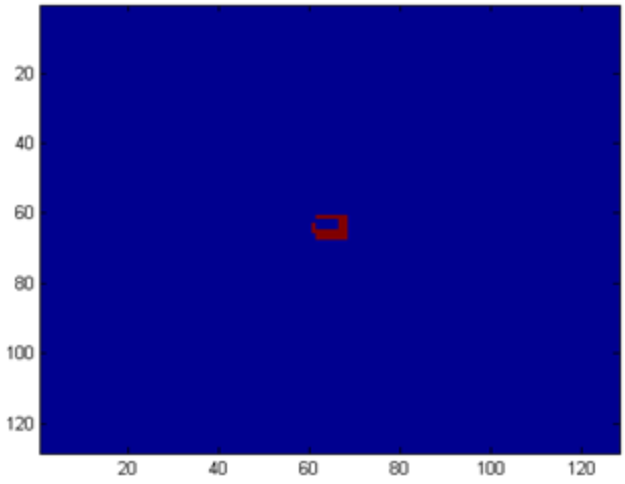

Figure 34. 128-by-128 input in MATLAB simulation: Red – LED, Blue – background

shown for a 128-by-128 discrete system. The emitting region of the source is denoted with the red pixels, whilst the blue area corresponds to zero-emission. The source coherence, directly related to its physical size, is described by the size of the emitting region relative to the hologram size.

2. ACF algorithm

Figure 35 shows the desired image intensity distribution used in the hologram generation. Figure 36 shows the replay simulated at the image plane for a hologram optimised by the ACF algorithm in order to steer the source depicted in Figure 34 by the distance given in Table 3.

It can be seen that the steered spots in Figure 36 are in good agreement with the desired

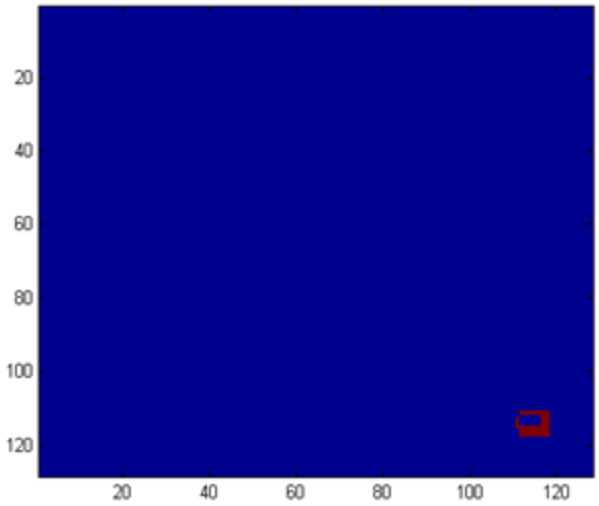

Figure 35. Desired image intensity: Red – image spots, blue – background

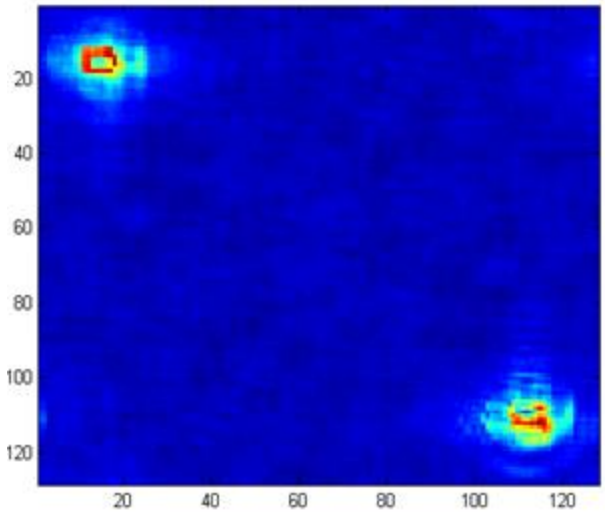

Figure 36. Simulated replay with an ACF hologram: Red – image spots, blue – background

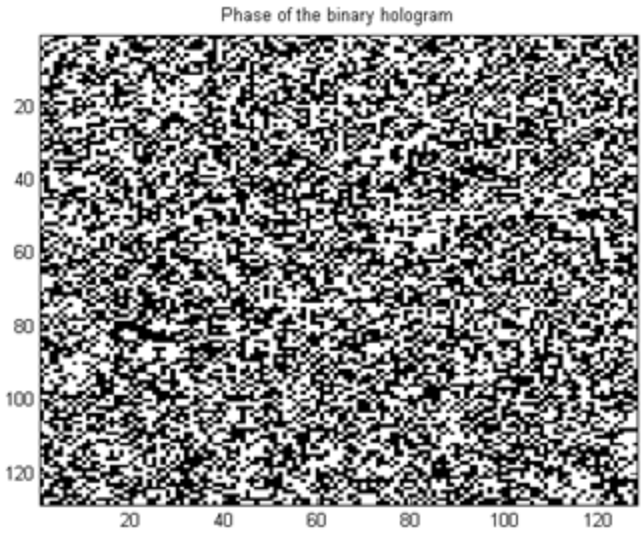

Figure 37. The corresponding hologram of the ACF simulated replay

target spot (red pixels) in Figure 35, up to a duplication resulting from the binary nature of the hologram (*cf*. Chapter V.B).

An interesting feature observed in Figure 36 is that the target spots are in point symmetry about the image centre, which is different from the geometric translation embodied in Eq.93. Whilst the translation relationship between the two target spots is intrinsic to any good beam-steering hologram as a result of Eq.93, it can be shown that point symmetry is not, *i.e*. another source distribution, when propagating through the same hologram, would not result in the same point symmetry. Therefore, the underlying hologram of this replay must have performed beam-shaping to a certain extent, and thus is not a pure beam-steerer as required.

Figure 37 shows the underlying hologram of the replay in Figure 36. This hologram contains a large amount of noise, with just a barely visible grating-like pattern to deflect the spots to the desired position. This noise can be explained by the fact that the algorithm has not terminated well, and there is still significant noise from the initial, randomised state present in the final hologram.

This remnant noise explains two features in Figure 36. The first is that a significant portion of the optical power is dispersed across the whole replay field, resulting in the randomly-noisy distribution for the whole replay. The second is that the noise dithers the grating-like pattern so much that the hologram is not a pure beam-steerer but also has some beam-shaping capacity, as already observed in the point symmetry in Figure 36.

The poor termination of the algorithm, which underlies the hologram noise, can be explained as follows: the ACF cost function essentially compares power spectra, thus the search can obtain holograms with broadly correct power-spectral envelopes—which, according to Eq.92, determine the spot positions—but has difficulty selecting the right phases for further optimisation. Consequently, the search struggles to terminate definitively, and the algorithm just randomly flips the pixels until the very end, resulting in the hologram noise.

Figure 38 shows how the error ε improves with the iterations. The big drop in the error indicates that the optical power is quickly concentrated into the correct spots. Then the increasingly gradual error-improvement means that the algorithm enters the inefficient phase to reproduce the spots. This asymptotic behaviour indicates that it may be difficult for the

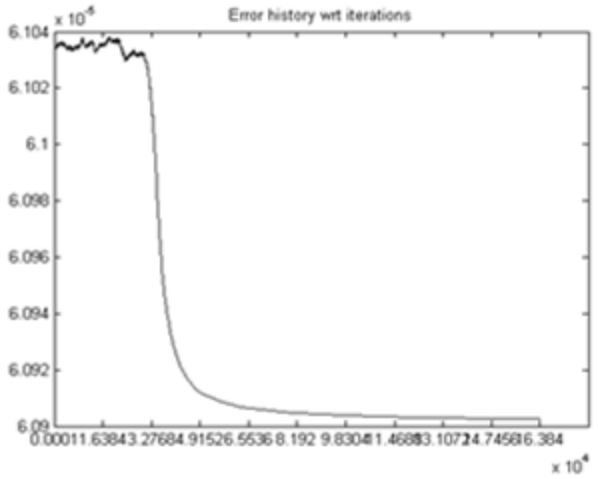

Figure 38. A search-error progress in the simulation of the ACF algorithm showing the values of the error against the iterations

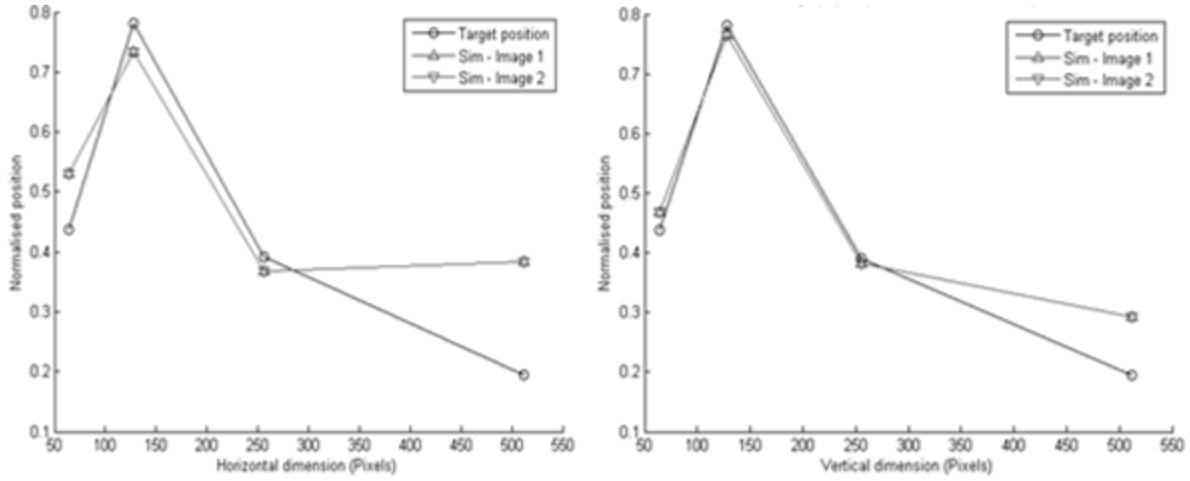

(a) (b)

Figure 39. Normalised positions of the two target-spot steered images for ACF-generated square holograms in (a) Horizontal direction; (b) Vertical direction

ACF to settle in the correct 'search path', and thus can often terminate with a wrong holographic pattern.

This behaviour of the ACF algorithm is observed for all array sizes in simulation. Figure 39 shows the positions of the centroids of the two target spots—denoted Image 1 and Image 2—given relative to the dimensions, against the hologram size. The perfect matching of the lines for Image 1 and Image 2 shows that the centroids of the target spots are in perfect symmetry about the image centre, as expected from the theory.

With the smaller holograms, the target spots track the desired position well. However, the lack of fine detail within the target spots means the simulated target-spot centroids are slightly displaced compared with the desired positions. This deviation is more pronounced in the horizontal direction than in the vertical, since the shape of the source (see Figure 34) means that its centroid is more stable vertically than horizontally when the shape is perturbed.

At the hologram size of 512-by-512 pixels, the differences between simulated target-spot centroids and the target positions become much bigger. This is because in a larger search

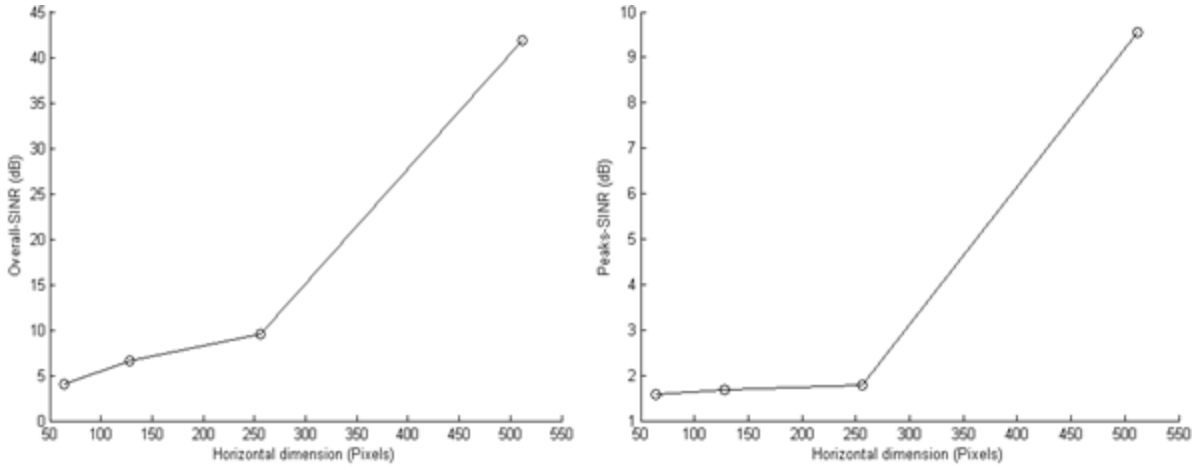

(a) (b)

Figure 40. SNR of the two target spots for ACF-generated square holograms: (a) Overall; (b) Against the most significant noise feature

space, the ACF algorithm can be trapped into a hologram which is far away from a good solution. Again, the vertical deviation is smaller than the horizontal one, due to the shape of the source. This particular case is investigated in more detail later in this section.

Figure 40 shows the two optical SNRs, as defined in Chapter V.B, for the different holograms generated with the ACF algorithm. For the smaller hologram sizes, both the Overall-SNRs and the Peaks-SNRs are small, especially the latter, due to the noisy fields which reduce both the optical power available in the target spots, as well as the relative prominence of the target spots. The increases of these SNRs with respect to the hologram size point to the efficiency of the algorithm to work with smaller sources, *i.e.* of higher degrees of coherence (and thus more plane-like wavefronts from the source arrive at the hologram.)

Figure 41 shows the replay for the case where the hologram is 512-by-512 pixels. It can be seen that the optical power is well concentrated into a few spots, leading to very high values of the Overall-SNR and Peaks-SNR in Figure 40. Figure 42 shows the underlying

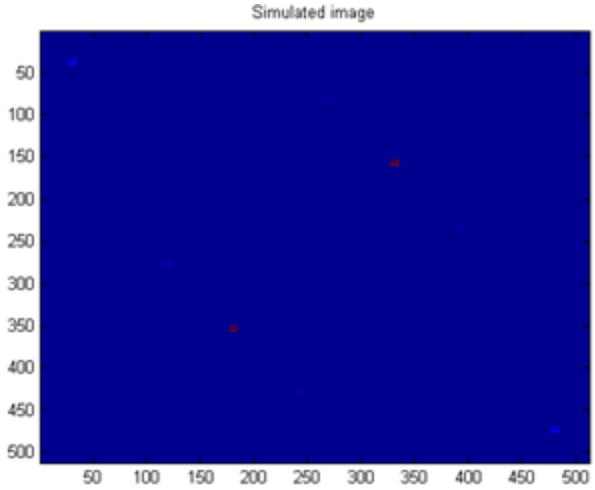

Figure 41. Simulated replay for ACF 512x512 hologram: Red – image spots, blue – background

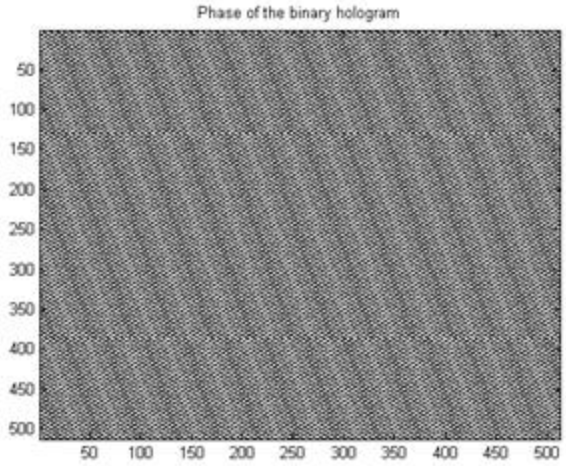

Figure 42. The corresponding ACF 512x512 hologram

hologram which has an almost perfect grating-like pattern, resulting in the expected translation geometry of the steered target spots in Figure 41.

For a 512-by-512 system, the source is almost like a point-source, thus the target autocorrelation and the ideal hologram are almost sinusoidal, and the quantised hologram a grating with regular spacing. The ACF algorithm's inefficiency causes it to settle with a

wrong holographic sinusoidal harmonic, in both horizontal and vertical directions, resulting in wrong positions of the target spots, as seen in both Figure 39 and Figure 41.

In this preliminary assessment, the ACF algorithm is shown to be most efficient at shaping the envelopes of the autocorrelation, but very inefficient at producing the finer details. As a result, it generates noisy correctly-steered images for bigger sources, whilst giving almost noiseless but wrongly-steered images for the smaller sources.

3. IMG algorithm

Figure 43 shows the desired image intensity distribution used in the hologram generation. Figure 44 shows the replay simulated at the image plane for a hologram optimised by the IMG algorithm in order to steer the source depicted in Figure 34 by the distance given in Table 3.

It can be seen that the replay and the desired image are in very good agreement—up to the quantisation-caused duplication—where the optical power is concentrated in well-detailed

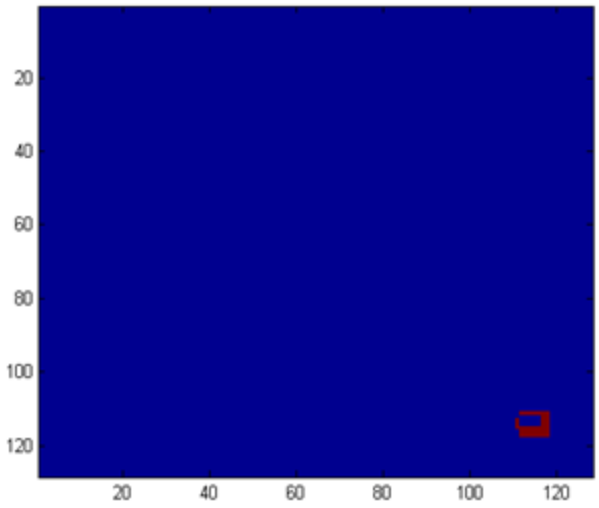

Figure 43. Desired image intensity: Red – image spots, blue – background

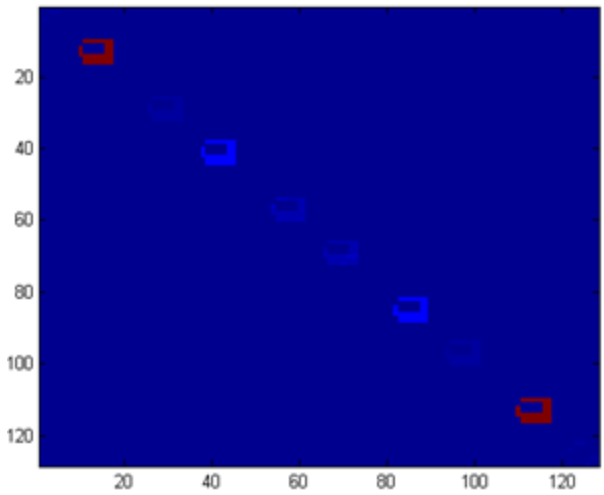

Figure 44. Simulated replay for an IMG hologram: Red – image spots, blue – background

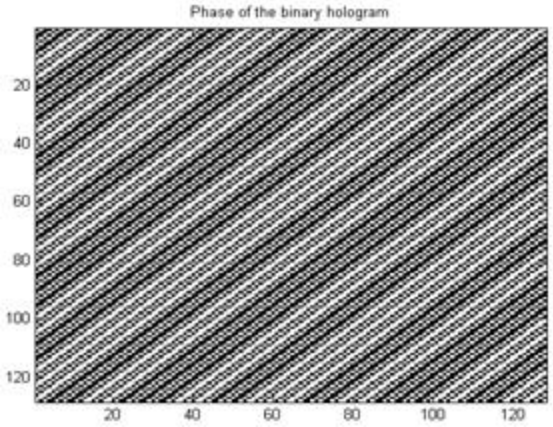

Figure 45. A resultant hologram from the simulation of the IMG algorithm

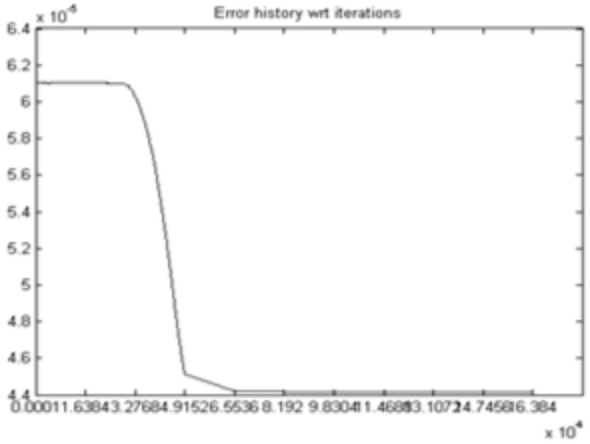

Figure 46. Search-error progress in the simulation of the IMG algorithm showing the values of the error against the iterations

target spots at the right positions, and a flat, nearly-zero background. The small noise peaks in Figure 44 result from the lower-orders of the hologram.

Figure 45 shows the hologram of this replay. This hologram has a grating-like pattern, with highly periodic, but irregular, spacing which distinguishes this hologram from those for beam-steering with coherent illumination (see [69], for example). The lowest frequency in this pattern steers the spot to the positions of the hologram's 1st orders.

Figure 46 shows the error history. It can be seen that after a large drop in the first part, the search very quickly settles into an optimised solution, as indicated by the flatness of the

second part, meaning no improvement can be made. This error history can be explained by the fact that with the IMG criterion comparing the image intensity distributions directly, the search seeks to improve both power concentration and image detail at the same time—both of which have equal weights. Thus when the fall occurs, improvements in both power concentration and image detail are almost exhausted, leaving little room for optimisation.

Figure 47 shows the relative positions of the centroids of the two target spots—denoted Image 1 and Image 2—against the hologram size. There is excellent agreement between the positions of these target spots and the desired positions across the simulation range.

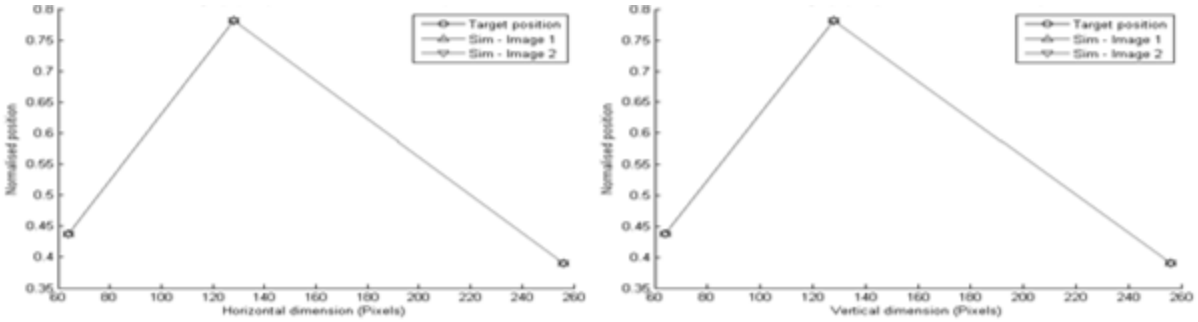

(a) (b)

Figure 47. Normalised positions of the two target spots for IMG-generated square holograms in (a) Horizontal direction; (b) Vertical direction

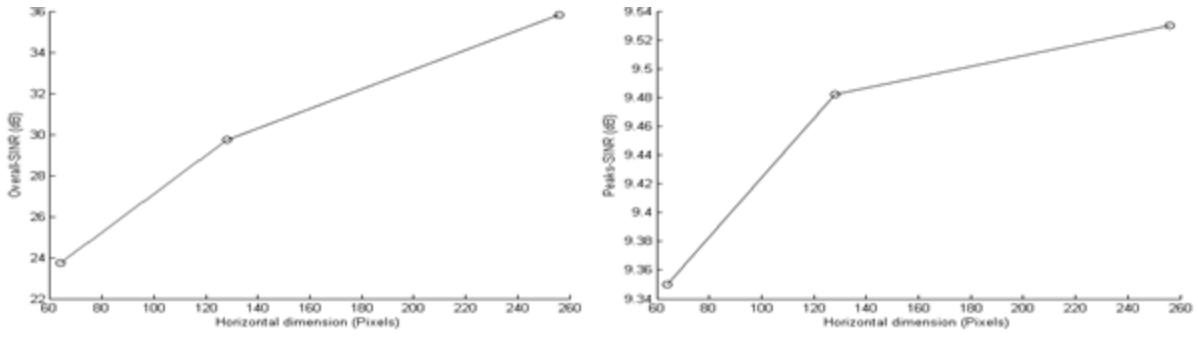

(a) (b)

Figure 48. SNR of the two target spots for IMG-generated square holograms: (a) Overall; (b) Against the most significant noise feature

Figure 48 shows the graphs of the optical SNRs against the hologram size. The Overall-SNR in Figure 48a is high and increases with respect to the hologram size. The Peaks-SNR in Figure 48b shows a small improvement of the order of 0.1dB. The essentially flat graph of the Peaks-SNR graph implies that the relative prominence of the peaks is almost unchanged even when the optimisation takes place over more iterations.

These initial results thus show that the IMG algorithm offers good and robust beam-steering capability, in both power concentration and target-spot positioning over a range of source sizes, with one aspect—the unwanted background noise—improving markedly with smaller sources.

4. MIXED algorithm – Mixture of the ACF and IMG criteria

The ACF and the IMG search-criteria for hologram search as preliminarily assessed in Chapter V.C.2 and Chapter V.C.3, respectively, have different performance characteristics, which can be summarised in Table 4. The ACF algorithm always generates beam-steering holograms with mixed performance, whilst the IMG-generated holograms offer good beam-steering performance for all cases.

However, as the IMG criterion essentially is the difference between the image intensities, it may mean that the IMG search can comparatively be less time-efficient as

Algorithm	Target-spot positioning	Target-spot power-concentration
ACF	Good (larger sources) Bad (smaller sources)	Bad (larger sources) Good (smaller sources)
IMG	Good	Good

Table 4. Summary of performance of the ACF and IMG algorithms

wrong search paths may not be avoided quickly, and thus in extreme cases it may be more prone to being trapped in local minima.

To take advantage of the strengths of both algorithms and avoiding their potential weaknesses, the two search algorithms are combined such that: for the first part of the search, the ACF criterion helps narrow down the set of possible holograms, and in the second part, the IMG criterion helps select the best holograms out of that narrowed set. The new search criterion is as follows:

$$e_{\mathrm{MIXED}}(R) = (1-k)e_{\mathrm{IMG}}(R) + k\gamma e_{\mathrm{ACF}}(R) \qquad \text{Eq.117}$$

Where: k is the mixing factor; γ is a constant to normalise the ACF and the IMG criteria to the same value-scale.

The normalising constant γ can be determined by taking the ratio of the initial value of e_{IMG} to the initial value of e_{ACF}.

The mixing factor k in Eq.117 evolves such that it is close to 1 when the search starts, and gradually tends towards 0 for a relatively significant portion of the search, in order that the set over which the IMG algorithm is applied is not too narrow. A simple formulation for this mixing factor can be the inverse exponential function as follows:

$$k = \exp(-\alpha n/N) \qquad \text{Eq.118}$$

Where: N is the total number of iterations to perform in the operation; n is the index of the current iteration; α is a constant to control the pace of replacement of ACF by IMG.

The criterion in Eq.117 is the basis for the third autocorrelation-based algorithm—the MIXED algorithm.

Figure 49 shows the desired image intensity distribution used in the hologram generation. Figure 50 shows the replay simulated at the image plane for a hologram optimised by the MIXED algorithm in order to steer the source depicted in Figure 34 by the distance given in Table 3.

It can be seen that the replay is of excellent agreement with the desired image. The replay in Figure 50 is very similar to that of the IMG in Figure 44, *i.e.* the well-detailed target spots in translation geometry and no field noises, whilst being much better than those by the ACF. The two differences between these two replays are that Figure 50 has slightly less crisp target spots and much less pronounced noise peaks than Figure 44.

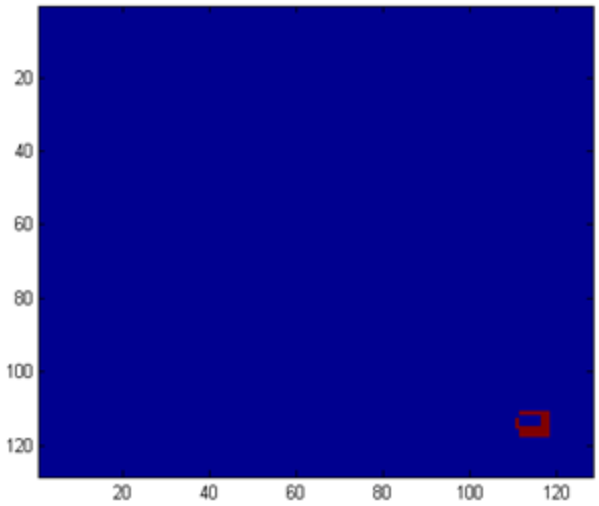

Figure 49. Desired image intensity: Red – image spots, blue – background

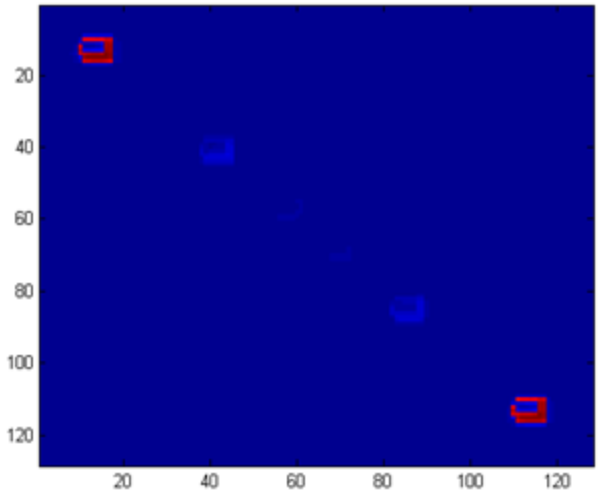

Figure 50. Simulated replay for an IMG hologram: Red – image spots, blue – background

Figure 51 shows the hologram generated by the MIXED algorithm. It can be seen that the hologram displays a dithered grating-like pattern. Two features can be observed from the dithering of this hologram. The first type is along the edges of the grating-like strips which helps suppress the cross-correlation terms in the coherence function of the illumination.

The second type is more irregular, especially near the borders of the hologram. These irregular spots destroy the higher frequencies in the hologram, thus suppressing the noise

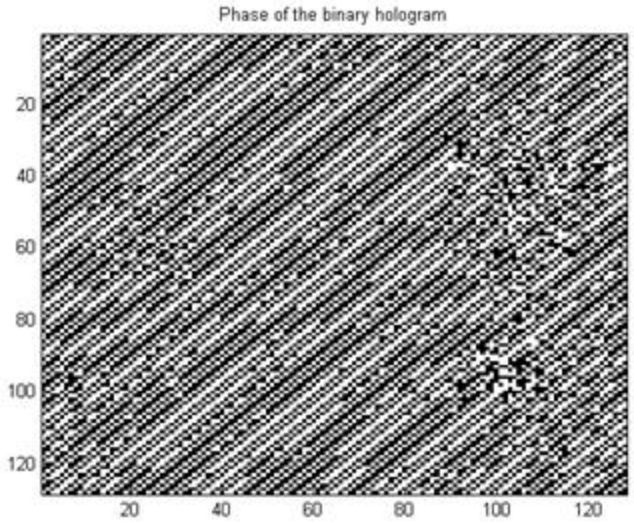

Figure 51. A resultant hologram from the simulation of the MIXED algorithm

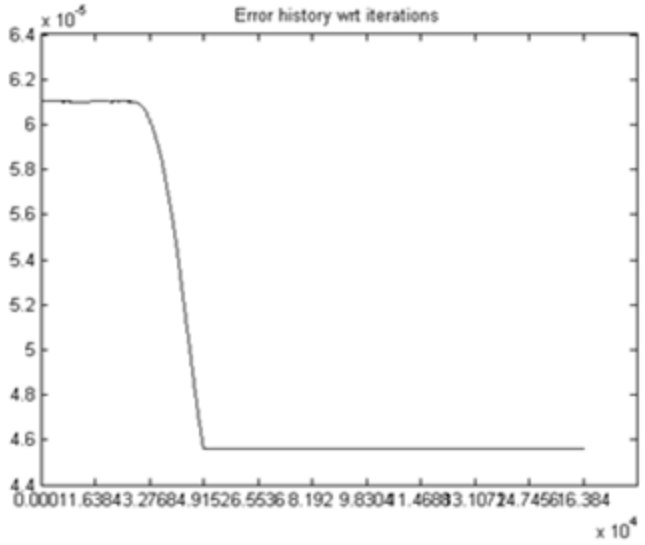

Figure 52. A search-error progress in the simulation of the MIXED algorithm showing the values of the error against the iterations

peaks caused by the quantisation high-orders, and concentrating the optical power into the target spots.

Figure 52 shows the error history for this MIXED-algorithm search. As expected from the definition of this algorithm, the first part of the graph shows resemblance to that of the ACF algorithm whilst the second part is similar to the IMG error history, with a horizontal

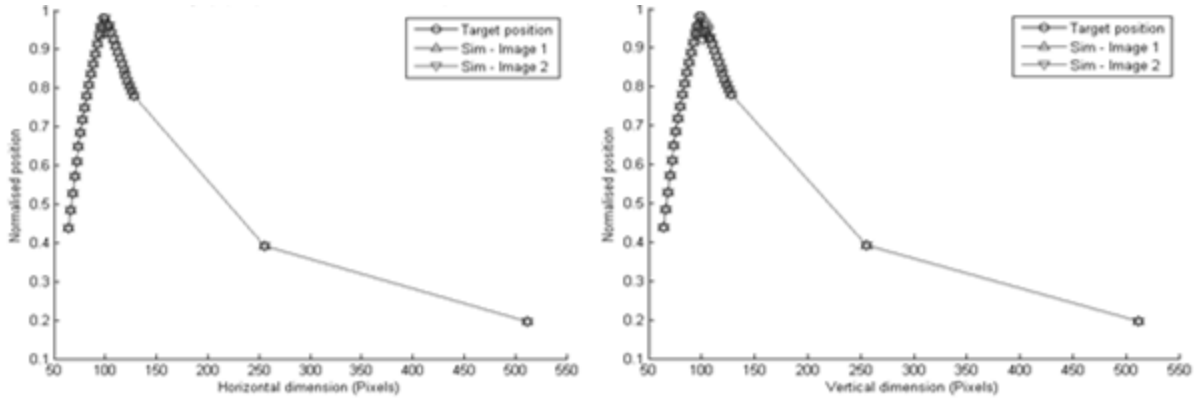

(a) (b)

Figure 53. Normalised positions of the two target spots for MIXED-generated square holograms in (a) Horizontal direction; (b) Vertical direction

line indicating that the optimised hologram has been found well before the search terminates. How early this optimised hologram is found is the topic of analysis in the next section.

Figure 53 shows the relative positions of the centroids of the two target spots—Image 1 and Image 2—against a range of hologram sizes. There is an excellent agreement between the positions of the two target spots and the desired position.

Where the normalised positions are close to 1, the target spots and the desired positions do not agree. In these cases, the target spots are steered to the very edge of the steerable region, and there is aliasing with higher diffraction orders which causes the calculation of the centroids to become imprecise.

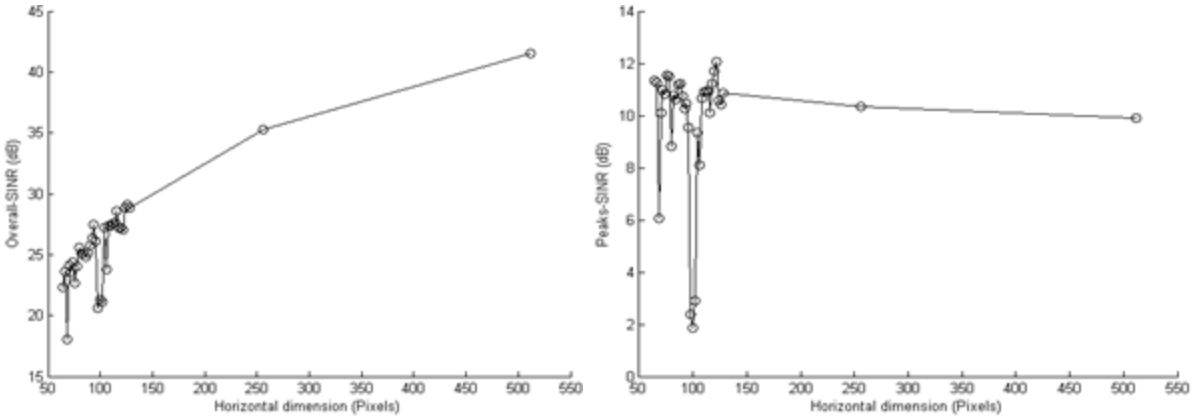

(a) (b)

Figure 54. SNR of the two target spots for MIXED-generated square holograms: (a) Overall; (b) Against the most significant noise feature

Figure 54 shows the Overall-SNR and Peaks-SNR for the MIXED algorithm against the hologram size. For the cases where the target spots are well within the steerable region, Figure 54 shows that the SNRs possess the same properties as those of the IMG algorithm: relatively constant Peaks-SNRs, with high Overall-SNRs which increase as the holograms become bigger (*i.e.* the source becomes smaller and more coherent.)

In both Figure 54a and b, the SNRs dip significantly where the hologram size is around 96-by-96 pixels. With the fixed target displacement of (50, 50), these cases correspond to when the target spots are steered to the edge of the steerable region, and higher-order aliasing starts to happen, causing imprecision in calculating target-spot centroids and thus target-spot powers, which directly lower both the Overall- and Peaks-SNRs.

This preliminary assessment thus shows that, in terms of beam-steering, the MIXED algorithm offers high and nearly identical performance to the IMG algorithm: good target-spot positioning, and good target-spot power-concentration.

5. Search time for the different algorithms

To compare the time performance of the different algorithms, two times are measured for each hologram: the total time the program takes to complete its run, and the time it takes to reach the optimised solution, denoted as 'effective' time in the graphs.

This effective time can be used to determine *a priori* a point at which the search can be safely terminated without affecting the final results. It is calculated by: firstly the average

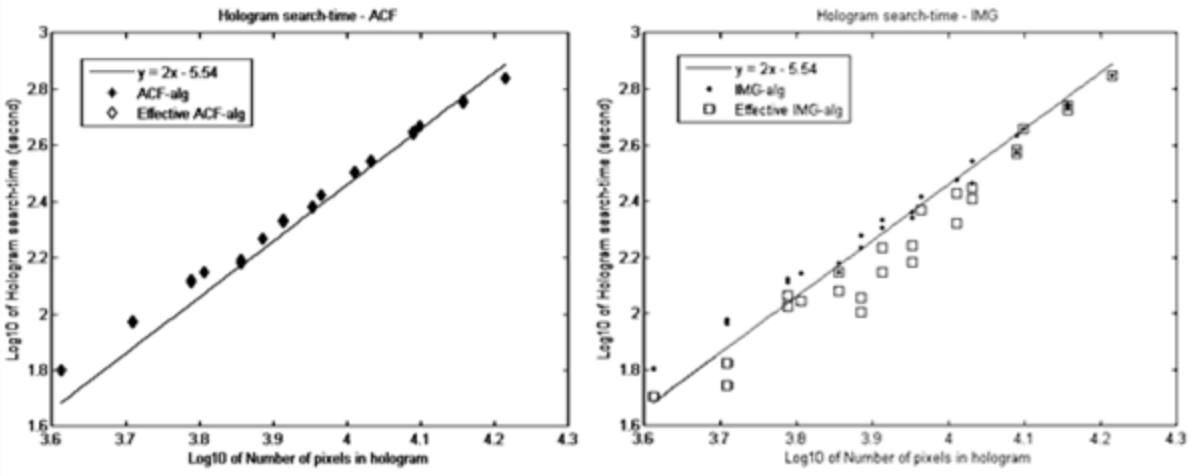

(a) (b)

Figure 55. Hologram search-time against number of pixels for: (a) ACF; (b) IMG

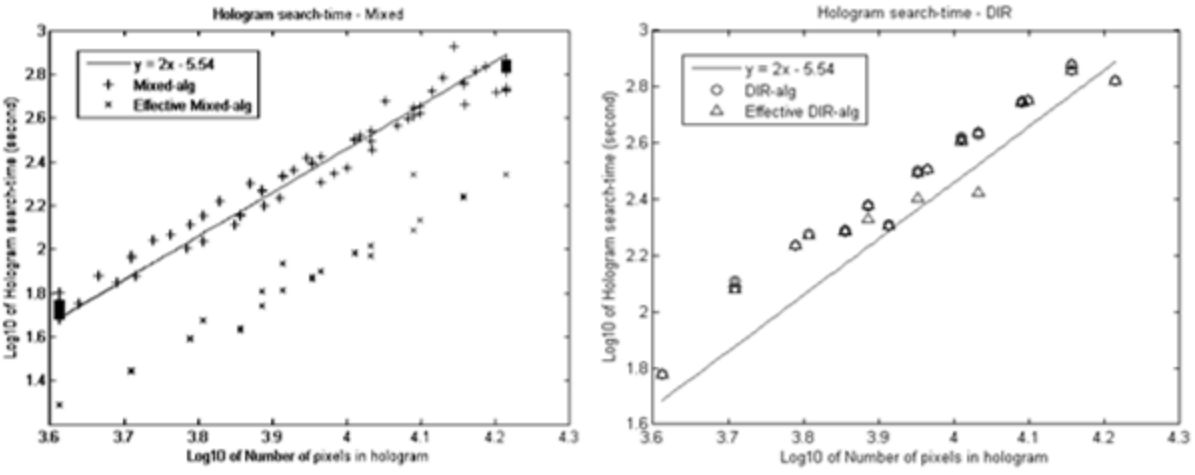

(a) (b)

Figure 56. Hologram search-time against number of pixels for: (a) MIXED; (b) DIR

time for a single iteration is calculated from the total time and the total number of iterations; then the number of iterations it takes the algorithm to reach the minimum error is found from the error history; finally the time taken to reach the minimum error, *i.e.* the optimised hologram, is found by multiplying these two numbers.

Figure 55a, b and Figure 56a, b show the generation times against the number of hologram pixels, for the ACF, IMG and MIXED algorithm and for direct binary search, respectively. It can be seen in all four graphs that the time taken is very large for larger holograms. This indicates that hologram generation with these algorithms is time consuming.

From the graphs in Figure 55 and Figure 56, the total-time trendlines show that the four algorithms all have time complexity of the order $O(N^2 \log N)$ as expected from Chapter IV.D.

Figure 55 and Figure 56 shows the MIXED effective times are up to 33% smaller than the corresponding times of the ACF and IMG algorithms, and up to 50% smaller than those of direct binary search. Therefore, the MIXED algorithm has by far the best time performance of the four algorithms.

Figure 56b shows that the total times of direct binary search are ~25% larger than those of the autocorrelation-based algorithms, as expected from Chapter IV.D. Also, the effective times are almost always the same as the total times, indicating the possibility of incomplete search when using direct binary search. Direct binary search is thus more time consuming whilst not as effective in generating holograms as the autocorrelation-based algorithms[§§].

In Figure 55a, the total times and the effective times of the ACF are equal in all cases, indicating that the ACF seach is incomplete as discussed in Chapter V.C.2.

[§§] The steering accuracy of the direct-dinary-search algorithm is not compared with, since as can be seen in Chapter V.C.4, the MIXED algorithm can achieve a very high steering-accuracy already, leaving very little room for improvement, if at all, by the direct-binary-search. Furthermore, the fact that direct-binary-search can be incomplete as inferred from the generation times also points to the possibility of its steering accuracy being not as high.

In Figure 55b, the effective times of the IMG algorithm are smaller than its total times for smaller holograms. With larger holograms, the similarity between the total and effective times points to the possibility that the algorithm is trapped in an unwanted search branch and causes the search to be incomplete.

These time-performance graphs thus show that the autocorrelation-based algorithms are faster than direct binary search, with the MIXED algorithm outperforming it by up to 50%. The MIXED algorithm is also the most effective at completing the hologram search.

D. Conclusions

In this chapter, a MATLAB program generates binary-phase holograms according to the autocorrelation-based algorithms, ACF and IMG, proposed in Chapter IV. Initial simulation results show that the obtained holograms perform well in steering the first-order images of the source to the desired positions for various source sizes.

However, the ACF-generated holograms have poor performance in terms of concentrating the optical power into the first-orders, due to the ACF criterion's inability to decide on phases. The IMG algorithm, thanks to its use of the image distribution, gives concentration of optical power resembling that of the source.

Since the ACF is faster than the IMG in steering the first-orders' positions, a third algorithm, MIXED, was proposed as a mixture of the ACF and IMG algorithms where the first part resembles the ACF algorithm whilst it shifts to resembling the IMG towards the end of the optimisation. This new algorithm is shown consistently to perform well in both aspects of beam steering whilst generally taking much less time compared with both the autocorrelation-based algorithms and the direct binary-search.

Chapter VI will describe an experiment to confirm the beam-steering performance of the holograms generated by these algorithms.

Chapter VI. **Experimental results & Simulated MIMO steering**

This chapter describes an experiment where the holograms generated with the three algorithms are tested using experimental devices. Holograms are displayed by a liquid-crystal spatial-light simulator (SLM) and this steers partially-coherent light from a quasi-monochromatic red light-emitting diode (LED) to a digital camera which records the replay plane. The experimental performance of the holograms is then compared with the desired targets.

A. Experimental set-up

1. Layout of the experiment

To exhaustively analyse the performance of the proposed algorithms, an experiment is carried out so that beam-steering metrics can be compared for each and every hologram in both simulation and experiment.

Figure 57 shows the schematic of the experiment with its control system. The source in this system is a light-emitting diode (LED) driven by an external current source whose output is modulated by a voltage source to allow strobed illumination. Light from the LED passes through a parallelising lens and a polariser onto a spatial light modulator (SLM.) On this SLM,

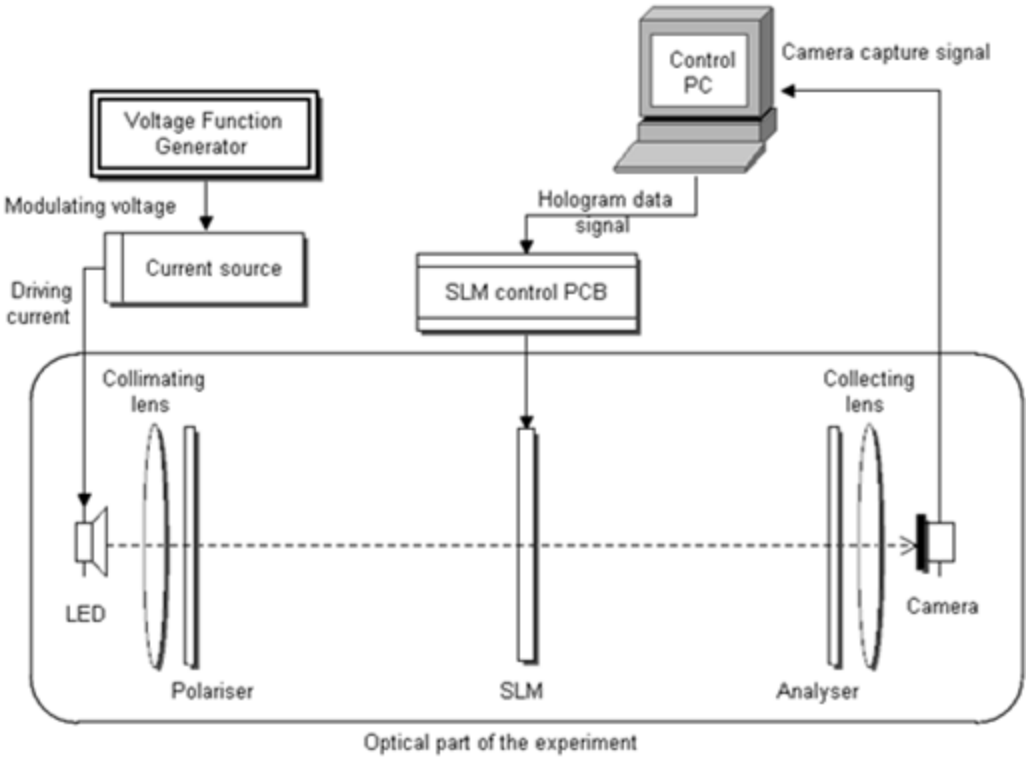

Figure 57. Schematic of the experiment and its control system

a pre-generated hologram to steer the light is loaded by the controlling computer, via a dedicated control PCB. After the SLM, the light passes through an analyser and is focused by another lens onto a camera, whose frames are captured by the control PC.

Figure 58 shows the experimental set-up. Although for simplicity, the optical path in the schematic is shown as if the SLM was transmissive, in the experiment a reflective liquid-crystal SLM is used as the holographic display.

Table 5 shows the dimensions used in the experiment. Light is incident on the SLM at an angle of 30° to the SLM's normal.

The experiment as laid out in both Figure 57 and Figure 58 includes an extra pair of polariser and analyser compared with the two-lens configuration analysed in Chapter IV. This arrangement helps improve the optical performance of the liquid crystals in the SLM in

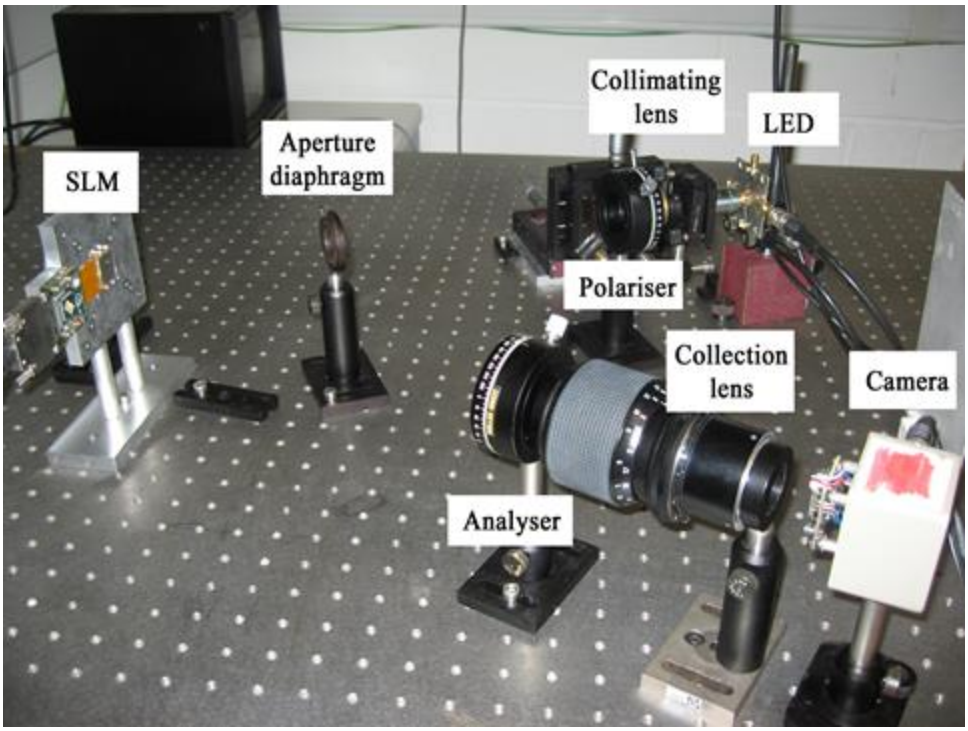

Figure 58. Photograph of the physical layout of the optical part of the experiment: transmission arm in the back, collection arm in the front

Transmission arm		Collection arm	
Distance	*Measurement (mm)*	*Distance*	*Measurement (mm)*
LED—Lens entrance	4	SLM—Analyser	315
Lens tube-length	30	Analyser—Lens entrance	38
Lens exit—Polariser	35	Lens length	100
Polariser dimension	30	Lens exit—Camera	52
Polariser—Iris diaphragm	220		
Iris diaphragm—SLM	160		
Total	479	*Total*	505

Table 5. Distances (in mm) along the optical path of the experiment

steering light [53, 56]. In addition, the iris diaphragm in front of the SLM in the transmission arm (see Figure 58) helps limit the diameter of the parallelised beam, so that the area outside the SLM's active cell is not illuminated in order to reduce the unwanted light reflected into the camera which would be collected into the unsteered spot.

2. Equipment

The optical devices used in this experiment, as shown in Figure 58, are:

1. Partially-coherent source: a custom-made resonant-cavity LED (RCLED) system is used as the source of quasi-monochromatic partially-coherent illumination for the experiment. The device has the size of ~30μm and emits wavelengths of ~650nm (red) with the half-angle beam-divergence of 30° [108].
2. Parallelising lens: a microscope-objective lens X40/.65 manufactured by Ealing is used to parallelise the light from the RCLED onto the SLM. With the tube length of 160mm and magnification of 40, its focal length is $f_1 = 160/40 = 4$mm.
3. Polariser-Analyser pair: a simple Glan-Thompson prism is used to polarise the parallelised light beam from the RCLED to the SLM, whilst a plastic polaroid sheet acting in the visible spectrum works as the associated analyser for the light reflected from the SLM.
4. Spatial light modulator: a reflective SXGA micro-display based on the ferro-electric liquid-crystal on silicon (FLCOS) technology manufactured by CRL Opto [109] is used as the SLM for the experiment. This device, driven by its own PCB, has a resolution of 1280 pixels by 1024 pixels and is set up so that it acts as the second monitor of the control PC (see Figure 57.) Consequently the hologram can be displayed by the control PC simply as a computer image on this second monitor.
5. Collecting lens: to focus the reflected light from the SLM to the camera, a Tamron MF Zoom lens model 158A is used as the collecting lens, with these specifications: entrance diameter 52mm, focal length 70-210mm, and maximum f-number 1:4-5.6.

To this lens, the object is at infinity due to the light parallelisation, so the f-number is set at $1/32$ and the focal length at $f_2 = 70\text{mm}$[***].

6. Camera: an analogue CCD camera is set at the focal plane of the collecting lens to capture the intensity distribution in the image plane. This camera outputs monochrome voltage signals (linear to the incident optical power) using the CCIR standard [110]. The CCD imager of this camera has the dimensions of 0.4-by-0.3 inches, resolution of 768-by-576 pixels, and pixel aspect ratio of 1:1.
7. Frame-grabber: (not shown in Figure 58) video signals from the camera are captured by the control PC with the card PCI-1407 made by National Instrument. The analogue signals are normalised with black- and white-level voltages then quantised into monochrome frames at 8 bits per pixel [111]. Device calibration gives the following voltage references: Black level: 55mV; White level: 650mV.

The detailed configurations of the SLM and of the LED are in the following subsections.

[***] This value puts the 1st-order region (defined in Chapter VI.B.1.b) well within the active area of the camera—see 0 for detailed calculations.

a. Spatial light modulator

Figure 59 shows the front view of the SLM described in Chapter VI.A.2. This FLCOS SLM consists of an array of pixels (the grey rectangle on the mount in Figure 59) which can be independently and electrically addressed [109]. Each pixel is a cell of ferroelectric liquid-crystals (FELC) and has a pair of planar electrodes set along its optical axis which, when having an appropriate voltage applied on, changes the crystal alignment, hence changing the crystals' dipole directions. This change in dipole moments in turn changes the polarisation of the electric field of the incident light, and therefore modulates the phase of the light for each pixel, which underlies the propagation analysis in Chapter IV. For a fuller treatment of this technology, see [53, 57, 60, 68, 112].

As discussed in Chapter V, the size of the SLM pixel dictates the extent of the steerable region in the image plane, whilst the total dimension of the SLM's array (*i.e.* its active area)

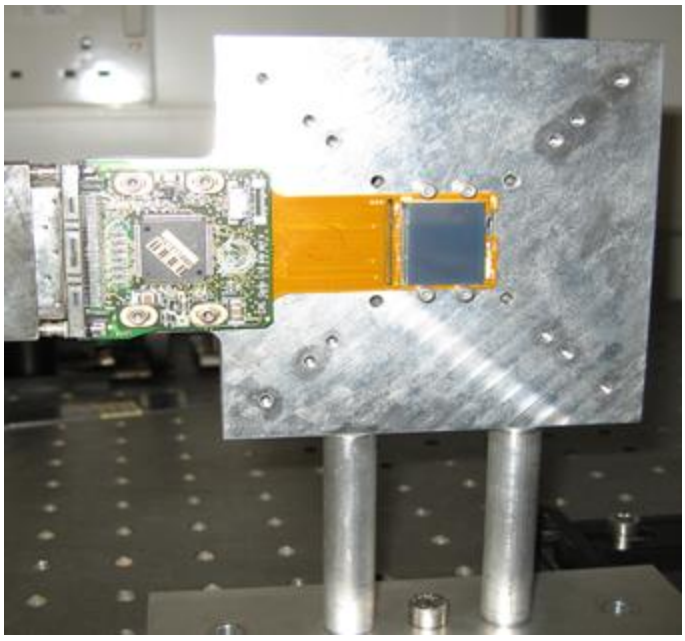

Figure 59. Front view of the spatial-light modulator, its drive-board and mount.

Hologram plane		Image plane		
Resolution	(μm)	Extent	(mm)	(% cam. CCD)
- Horizontal	13.62	- Horizontal	6.68	65.7
- Vertical	13.62	- Vertical	6.68	87.7
Extent	(mm)	Resolution	(μm)	(% cam. pixel)
- Horizontal	17.43	- Horizontal	5.22	70.2
- Vertical	13.95	- Vertical	6.52	87.6

Table 6. Extents and resolutions in the hologram and image planes

determines the image resolution. Using the relationship in Eq.92 between the distances in the hologram and image planes, with $f_2 = 70\text{mm}$ and $\bar{\lambda} = 650\text{nm}$, and the dimensions of the SLM in [109], the extent the steerable region[†††] and the resolution in the image plane can be calculated in absolute values and as fractions of the camera CCD and pixel, respectively. In Table 6, it can be seen that the steerable region falls well within the camera capture area, whilst the finest image detail would be well represented by a camera pixel.

The SLM active area has the dimensions of 1280x1024 pixels, which are much bigger than the holograms generated (between 64-by-64 pixels and 512-by-512 pixels.) The holograms are tiled across the SLM in a repetitive manner. As a result, a parallelised beam bigger than the displayed hologram, when incident on any part of the SLM, will still 'hit' a full copy of the hologram and be modulated due to the fact that autocorrelation is invariant with respect to translation of the underlying function, if periodic. In this case, the hologram-generation program is implemented so that the autocorrelation is calculated with circular convolution of the hologram, to simulate the periodicity.

[†††] The extent is twice the maximum deflection.

The SLM has a built-in DC balancing algorithm to ensure that, when displaying still frames, the average voltage across each pixel is zero so that no performance degradation occurs. This algorithm works by alternately displaying the hologram and its inverse at a frequency of ~60Hz [109]. To make sure that the SLM is illuminated only when the hologram itself is displayed, the light from the LED is strobed at the same frequency as the SLM's refreshing rate.

b. Source LED

As mentioned in Chapter VI.A.2, a resonant-cavity red LED custom-made by Imperial College London is used as the partially-coherent illumination source for the experiment. To avoid saturating the camera, empirical calibration based on [108] gives an average input current of ~2mA which sets total optical output at ~20μW.

Since the LED's illumination must be strobed to match the DC balancing of the SLM, the driving current has to have a frequency ~30Hz. To achieve this, a current source ThorLabs LDC 205C [113] receives the voltage output of the pulse generator HP 8112A [114]—set at 30Hz—as its controlling signal (see Figure 57.) The output of the current source thus has a square waveform at ~30Hz and alternates between 0 and 4mA, matching the LED's illuminating with the SLM's refreshing rate whilst avoiding camera saturation.

B. Experimental procedure

1. Calibration data

The initial stage of the experiment is to collect data about imperfections in the imaging system for correction in the later stages so that the evaluation of the captured image intensity distributions would yield only the beam-steering performance of the holograms. There are two sets of such imperfections: the intrinsic defects of the camera, and the deformation of the images at the camera plane due to the geometry of the experiment.

a. Dead-pixel identification and Black-level noise

The camera used in the experiment has two major defects which would affect the captured image intensity: dead pixels and black-level noise. To identify these intrinsic camera defects, the LED source is turned off so that there is no illumination on the camera, then 60 successive frames are captured from the camera into MATLAB.

Dead pixels in the camera's charge-coupled device (CCD) cause the values for these pixels always to stay fixed at high levels regardless of the physical optical intensity, and thus would adversely affect all integration calculations (see Chapter VI.B.3.) With the assumption that any pixels whose values stay fixed across all 60 frames are ‘dead’, comparison of the captured frames returns a list of these dead pixels with positions and values where they are ‘dead’ at. This list is stored for later corrections, which subtract these dead-pixels from the captured frames and use interpolation to estimate their correct values in the captured frames.

The black-level noise is the electrical noise of the CCD which causes the camera to return some readings even when there is no illumination, resulting undervaluation of the power-concentrating capability of the hologram by increasing the background noise. Using

the 60 frames corrected for dead pixels, assuming that the noises in the camera pixels are of independent and identical distributions, the mean noise level is calculated as the average value across all the pixels of the 60 corrected frames. As this noise is equivalent to optical intensity, to correct the optical power only the mean of the noise is needed.

b. Frame deformation

The misalignment of the camera and the rest of the system (chiefly, the SLM) about the optical axis means that the frame captured by the camera is a deformed version, by rules of geometrical transformation, of the image intensity distribution the camera should have captured. There are three possible types of deformations:

- Shift: The camera is off the optical axis such that the unsteered spot does not fall on the centre of the camera frame.
- Rotation: The camera is rotated relative to the SLM about the optical axis so that the coordinate system of the camera frame is also rotated relative to the coordinate system of the image intensity distribution (see Chapter IV.B.)
- Skew: The camera is rotated about an axis orthogonal to the optical axis, causing the frame to capture a projection of the image intensity distribution.

Two 128-by-128 holograms are used to assess the extent of these deformations in the experiment. The two holograms are such that the target spots in their intensity distributions when combined are located at the 4 corners of a quadrilateral. As each binary hologram generates 2 symmetric target spots, each of these calibration holograms will generate 2 opposing corners of the quadrilateral. These holograms themselves are generated with direct binary search whose holograms have verified beam-steering performance [32, 38, 54, 58, 59, 61, 63, 65]. The steps used in calculating the deformation-correction data are as follows:

1. Frame capture and composition: The frames corresponding to the two calibration holograms are captured following the procedure laid out in Chapter VI.B.2. These frames are then corrected for dead pixels, and combined to a single frame with 4 first-order images.
2. Calculation of the image positions: Using the cross-correlation method described in Chapter V.B, the coordinates of the 4 first-orders in the camera's own coordinate system are calculated. The position of the unsteered spot is calculated from the reference frame captured in step 1.
3. Skew assessment: when the camera and the SLM are perfectly aligned, the 4 first-orders should form 4 corners of a rectangle whose centre is the unsteered spot, which itself should stay fixed. Measurements show that, skew is non-existent and no correction is needed for this type of deformation.
4. Rotation angle: The angle between the sides of the rectangle formed by the target spots and the sides of the compound frame is the angle by which the camera is rotated relative to the SLM. This angle is calculated by straightforward geometry.
5. Steerable region: As the size of the SLM pixel is finite, the extent to which the image can be steered is also finite[‡‡‡]. This region is called the steerable region to denote the maximum extent to which the target spots to can be moved, and it corresponds to the array representing the image plane.

[‡‡‡] This is the direct consequence of the fact that, in a two-lens configuration, the hologram plane is the Fourier plane of the image plane and the pixel size is the spectral resolution of the image intensity distribution. With a finite spectral resolution, the distribution is periodic beyond (spectral resolution)$^{-1}$.

The camera captures frames which are bigger than this steerable region, therefore trimming must be done on the frames, by calculating the positions of the 4 corners of this region.

First, the images of the calibration holograms, calculated using Eq.92, are combined. Then by cross-correlation with the reference frame, the positions of their target spots relative to the image array-size are found. As these relative positions are also the ratios of the target-spot positions, relative to the unsteered spot, in the combined frame to the frame size, the corners of the steerable region in the frame can be straightforwardly calculated.

The calibration parameters calculated in this stage of the experiment are then applied to the frames collected in the later stages both to correct for geometrical misalignments and to trim the frame to only the steerable region which is the area of interest.

2. Frame collection

The LED is on and strobed as described in Chapter VI.A, and a MATLAB-based software controller extracts a hologram from the data file and proceeds through the following steps to collect the necessary data for post-processing before moving on to the next hologram:

1. Reference frame: the SLM first displays a blank hologram (*i.e.* all pixels are set to the same value) which in effect turns the reflective SLM into a mirror. The image intensity distribution at the camera plane is identical to the source intensity distribution. Several frames are captured by the camera, and the frame with the largest total optical power (calculated with integration) is selected as the reference frame for the hologram of interest to account for the interlacing of the camera signals[§§§].
2. Hologram displaying: The beam-steering hologram as extracted from the data file in all experimental cases is much smaller than the SLM itself (*cf*. Chapter VI.A). To ensure the displayed image covers the whole SLM area, the hologram is repeated cyclically [101] which gives the same beam-steering performance as a hologram whose autocorrelation is calculated with circular convolution—see Chapter V.A. This repeated hologram is displayed by the SLM until the operation with the next hologram.
3. Captured multi-frames: As mentioned in Chapter VI.A, the SLM has a built-in DC balancing which alternately displays the hologram and its inverse, passing through a short period of all-0 pixels. At the camera plane, this sequence corresponds to an alternating series of intended steered images, steered images

[§§§] In principle, this reference frame needs to be captured once as the source intensity distribution does not change. However, the experiment was found to take long time, and thus to account for potential variations with time in optical output of the LED, a reference frame was captured for each hologram.

with reduced intensity, and un-steered images. To avoid the potential mis-synchronisation between the LED strobing and the SLM balancing, instead of capturing only one frame, a set of 60 consecutive frames is captured, which should include the frame with the intensity distribution of interest.

4. Frame selection: As the LED strobing is slightly out of sync with the SLM DC-balancing sequence, the frame that has the correct intensity distribution has to be singled out:

   First, a multiplicative mask created from the reference frame is applied to all 60 captured frames such that the unsteered spot is all masked out.

   Subsequently, the optical power within each frame is calculated by integration. Since the inverse hologram causes a reduction in image intensity whilst the un-steered images should have the lowest power of all due to the unsteered spot being masked out, the frame of interest should have the highest power of all the 60. Therefore, a simple search should return the desired frame.

Following the aforementioned 4 steps of frame collection, the data for each hologram now contains 3 MATLAB arrays: the non-padded hologram itself, the reference frame, and the frame selected from step 4 that contains the intensity distribution associated with the hologram. These frames are used in the post-processing stage to evaluate the beam-steering performance of the hologram.

3. Performance-metrics calculation

The experimental beam-steering capability of a hologram is assessed by the same metrics used in simulation evaluation: how close the steered image is to the target position, and how closely the intensity distribution of the steered image resembles that of the source. Since the hologram is binary-phase, as discussed in Chapter V, both target spots are again used in the evaluation. The assessment criteria are therefore the positions of these target spots within the captured frame, and the amount of optical power they contain in comparison with the rest of the frame.

To extract these target spots, the captured frame, obtained as described in Chapter VI.B.2, corresponding with the hologram of interest is run through a MATLAB-based post-processing module. This module follows the following steps:

1. Frame calibration: Before any position-based processing can be done, the captured frame must be calibrated to ensure that any geometrical deformations are corrected for. Using the calibration data obtained as in Chapter VI.B.1, the frame is first corrected for dead pixels. It is then rotated to account for relative rotation around the optical axis between the SLM and the camera[****]. Lastly, the frame is trimmed to only the steerable region, which also has the effect of setting the unsteered spot as the frame's centre (*cf*. Chapter VI.B.1). The frame is now ready for processing to extract target spots and calculating the metrics.
2. Zeroth-order suppression The unsteered spot is suppressed from the image intensity distribution by using a multiplicative mask based on the known source intensity distribution.

[****] As noted in Chapter VI.B.1, no skewing was detected in the calibration frames, therefore no transformation was applied for skew correction.

3. First-order positions (similar to that in Chapter V.B).
4. First-order power (similar to that in Chapter V.B).
5. Optical SNRs: Overall-SNR and Peaks-SNR are again used as figures-of-merit to measure the success of the hologram in concentrating target-spot power. Firstly, the optical powers in the regions of interest are calculated by pure integration of the intensity. These powers are then corrected for black-level noises by subtracting the noise mean obtained from calibration (*cf*. Chapter VI.B.1). Overall-SNR and Peaks-SNR are then calculated as in Chapter V.B.

Thus the experimental performance of each hologram is also measured by 6 metrics:

- Four positions: two for each target spot for the horizontal and vertical dimensions;
- Two optical SNRs: Overall-SNR and Peaks-SNR.

C. Experimental results

1. Initial results

This section shows the initial results of the experiment, where the frames captured by the camera are compared with the corresponding simulated replays for the same holograms which are analysed in the initial simulation assessment in Chapter V.

Figure 60a and b show the simulated replay and the image captured in experiment, respectively, with a hologram optimised by the ACF algorithm in order to steer the source depicted in Figure 34 by the distance given in Table 3.

It can be seen that, except for the spot at the centre of Figure 60b which will be explained later, the replay and the captured image are in agreement. In both, there are two areas of relatively higher optical-power concentration at the same positions at the top-left and bottom-right corners which represent the target spots already seen in Chapter V.C.2. Both also have very noisy backgrounds—so noisy that the target spots in Figure 60b, already plotted as

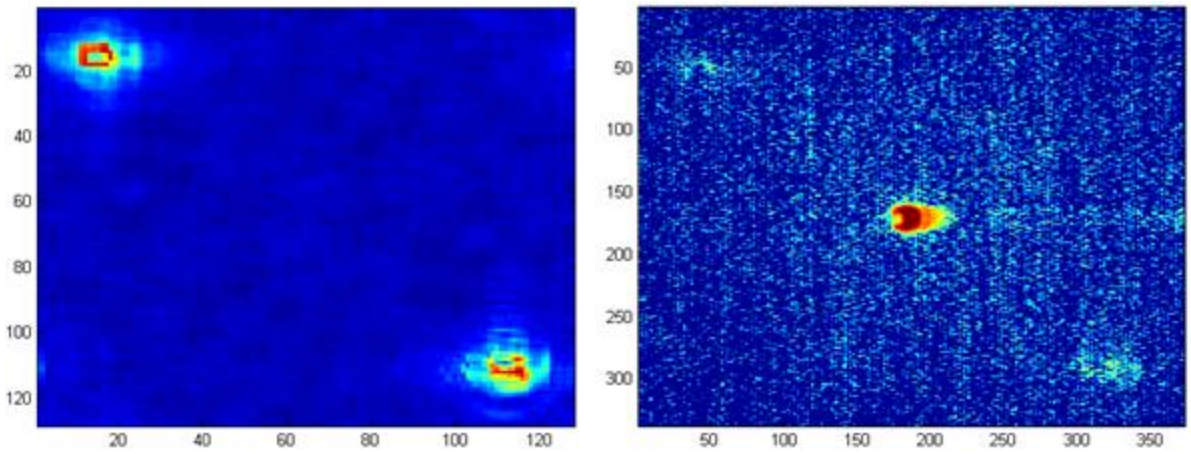

(a) (b)

Figure 60. (a) Simulated replay of an ACF hologram; (b) Log-intensity of experimentally captured image

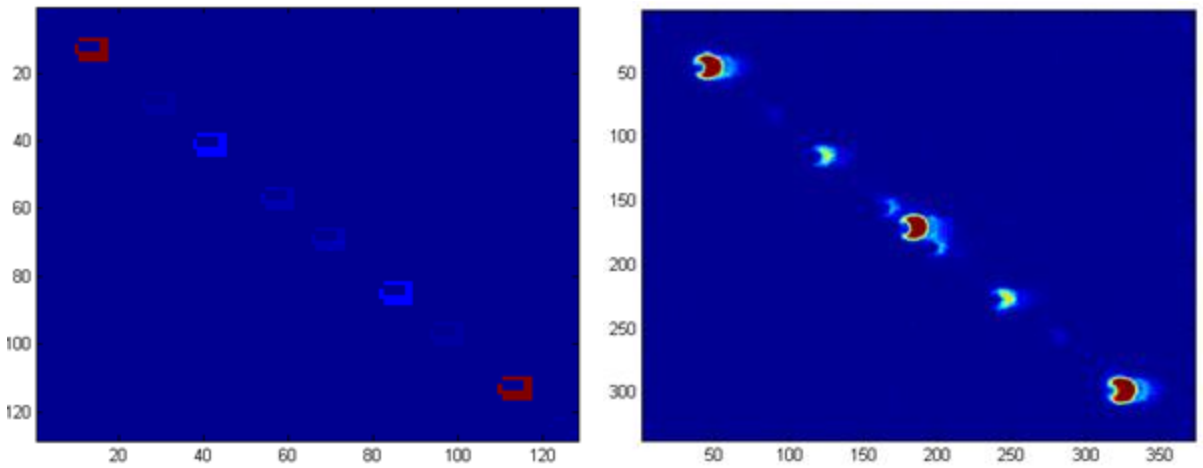

(a) (b)

Figure 61. (a) Simulated replay of an IMG hologram; (b) Experimentally captured image

log-intensity, are nearly indistinguishable.

Figure 61a and b show the simulated replay and the experimentally captured image, respectively, with a hologram by the IMG algorithm to steer the source in Figure 34 by the distance in Table 3. It can be seen that the replay and the experimental image are in excellent agreement. The only difference is in the shapes of steered target spots, as expected, since these are the source distributions which differ between the simulation (*cf*. Figure 34) and the experiment (where the LED source has a moon-shaped distribution.)

Figure 62a and b show the simulated replay and the experimentally captured image, respectively, with a hologram by the MIXED algorithm to steer the source in Figure 34 by the distance in Table 3. It can be seen that there is also excellent agreement between simulation and experiment, up to the shape difference.

In the experimentally captured images in Figure 60b, Figure 61b, and Figure 62b, the central spots are highly prominent, whilst totally absent in the simulated image. These spots represent the specular images formed by the non-steering parts of the holographic display, and possibly also by the incoherent component of the incident light. They are ignored for the

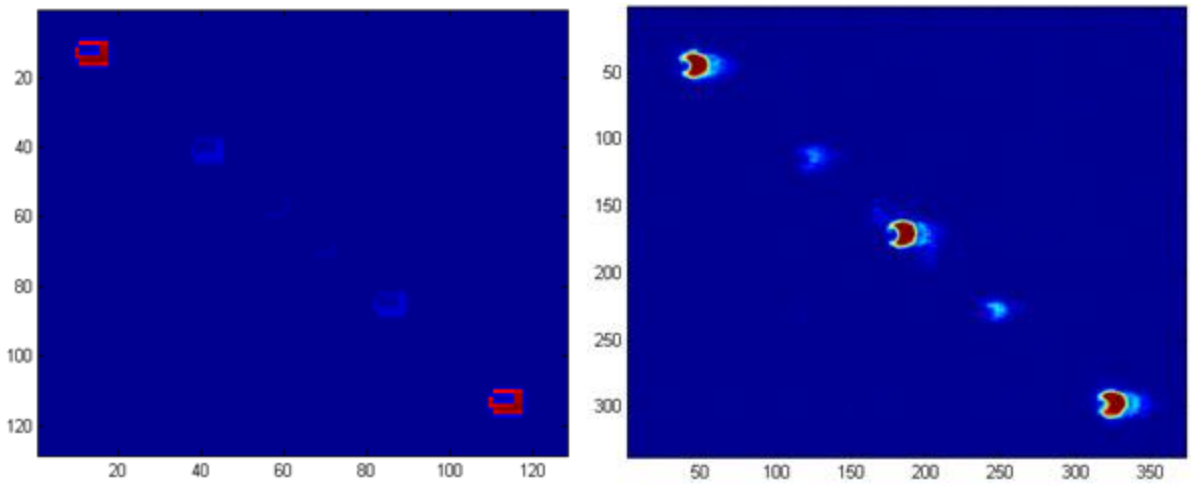

(a) (b)

Figure 62. (a) Simulated replay of a MIXED hologram; (b) Experimentally captured image

purpose of comparing holograms' performance in simulation and experiment, in this and all subsequent sections.

Comparisons using Figure 60, Figure 61, and Figure 62 for the three autocorrelation-based algorithms thus show that there is excellent agreement between the simulation, described in Chapter V, and the experiment. The only differences are the shapes of the spots and the presence of the specular spots at the centres of the experimental images, both of which can be ignored in the next analyses.

2. Experiment 1 – Holograms with variable dimensions

The first experiment tests the ability of the autocorrelation-based algorithms, *i.e.* ACF, IMG and MIXED, in coping with two degrees of freedom, *i.e.* two dimensions independently vary. For all three algorithms, the generated holograms are of a range of horizontal and vertical sizes and have the general rectangular shapes, rather than just square as in Chapter V.

For these rectangular holograms, the target positions are fixed at +50 pixels horizontally and +50 pixels vertically compared with the unsteered spot, same as in Chapter V. With the smaller sizes which would have put these targets outside the images, a circular shift is performed and the target is 'circled' to the other half of the image (*cf.* MATLAB's circshift function [115].)

Apart from sizes, the holograms are generated with the program and parameters described in Chapter V. The source-array is set to have a fixed-size emitting area, whilst the size of the non-emitting area is changed according to the size of the system pixelation, thus representing sources of different sizes (*cf.* Chapter V) and accordingly of different degrees of coherence. In the experiment, the source size is fixed by the physical size of the LED.

For each algorithm, the results are shown for both in simulation and in experiment. This is to provide exhaustive analyses for both simulated and experimental performance. The simulation metrics are shown for the full image-arrays, whilst the experimental metrics are calculated for the steerable regions only.

For both simulation and experimental results, the two target spots are separately identified as Image 1 and Image 2, whilst the SNRs for both target spots are combined as discussed in Chapter V.

a. ACF algorithm

Figure 63a and b show the horizontal and vertical positions of the target spots relative to the hologram dimensions, respectively, for the holograms generated with the ACF algorithm.

In both graphs, it can be seen that the surfaces for 'Sim – Image 1' and 'Sim – Image 2' follow closely the surface 'Target position' which describes the desired position. Thus, the simulated target spots track the desired positions well for all hologram sizes.

In Figure 63a and b, it can be seen that the gaps between the simulation-result surfaces and the desired-position surface gradually widens as the normalised positions become smaller than 1. This means that, the absolute positioning errors become larger as the desired positions move closer to the image centre and that the ACF algorithm is less efficient at steering the target spots by small distances.

In Figure 63a, the grid-lines of the 'Sim – Image 1' and 'Sim – Image 2' surfaces are almost straight and parallel with the 'Vertical dimension' axis. In Figure 63b, the straight grid-lines are parallel with the 'Horizontal dimension' axis. This shows that the horizontal and

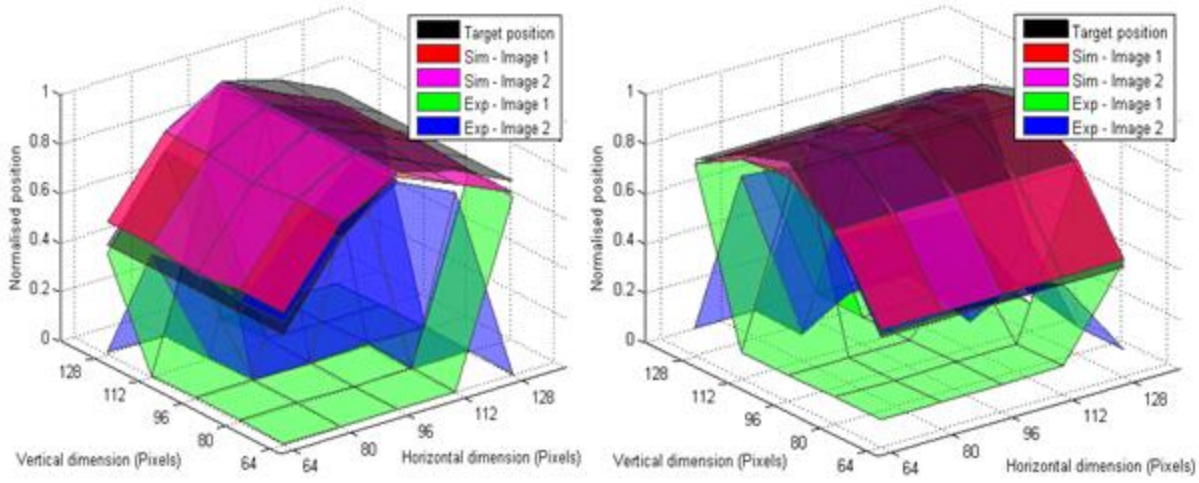

Figure 63. Expt 1 - Normalised (a) Horizontal and (b) Vertical positions of the two target spots for ACF-generated rectangular holograms

vertical steering of the simulated target spots are independent from each other, showing the algorithm works well with 2 degrees of freedom.

In Figure 63a, when the holograms have the vertical dimension of 96 pixels, the simulated horizontal positions are slightly closer to the image centre than at other vertical dimensions. At this hologram size, the desired positions are right at the borders of the steerable region, causing high-order aliasing and thus distorting the target-spot shapes so that the positions are not calculated correctly. This effect is not observed in Figure 63b due to the simulated source shape (*cf*. Figure 34) which makes the miscalculations much less pronounced in the vertical direction.

In both Figure 63a and b, for the smaller hologram sizes, the 'Exp – Image 2' surfaces follow quite closely the simulation surfaces, indicating the good agreement between simulation and experiment; whilst the corresponding parts of the 'Exp – Image 1' surfaces have the value of 0. At the larger hologram sizes (each dimension larger than 96 pixels), the reverse is observed: 'Exp – Image 2' is now at 0, and 'Exp – Image 1' is in good agreement with the simulation.

These observations are explained by the internal misalignment of the collection lens, which favours light from one half-space (divided by the meridional plane) more than the other, resulting in reduced optical power concentrated in one half of the image plane. With the large background noise, as seen in Figure 60, the target spots in this dimmed half-plane are not detected successfully, and thus it is the remnant of the removed unsteered spot that is detected instead, resulting in the value of 0.

In the favoured half-plane, the target spots are detected successfully. The swapping of the dimmed-bright states between the two experimental target spots is explained by the circular shifting of the desired position when the hologram sizes are small.

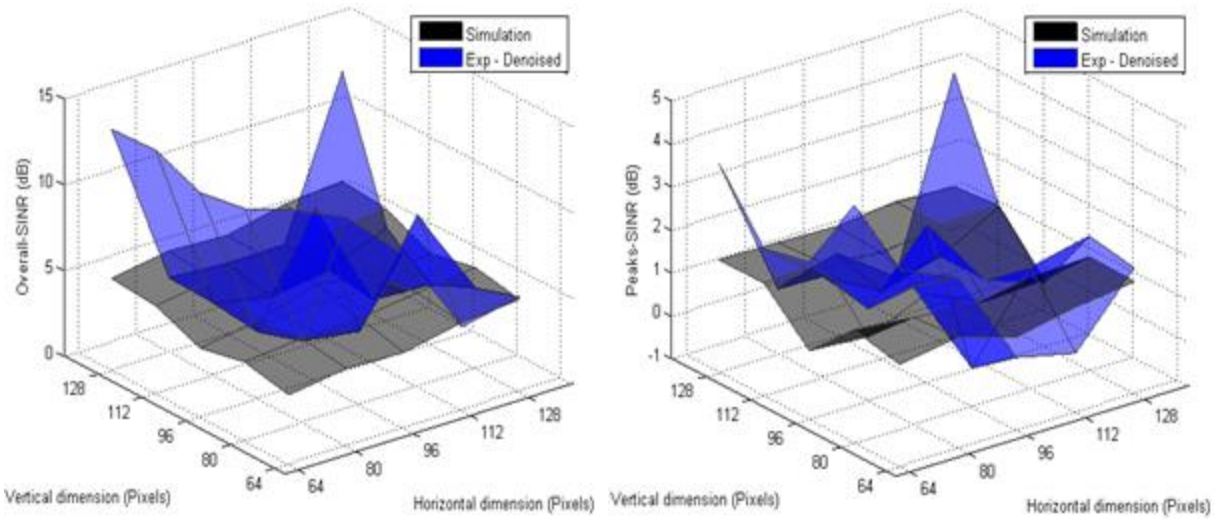

(a) (b)

Figure 64. Expt 1 - (a) Overall-SNR and (b) Peaks-SNR of the two target spots for ACF-generated rectangular holograms

Figure 64a and b show the Overall-SNRs and Peaks-SNRs for the target spots. The simulation SNRs are low for all cases, since the images have a very dominant background noise caused by the holograms—see Chapter VI.C.2.a. For the experimental SNRs, as expected from the non-detectability of the target spots, the Peaks-SNRs are very low, whilst the acceptably higher Overall-SNRs can be explained as the strong remnants of the removed unsteered spot that distort the results.

From both the simulation and the experimental results, it can be concluded that the ACF algorithm has acceptable spot-positioning capability, but is less efficient with small deflections. It has poor power-concentrating performance in both simulation and experiment, especially the latter since the noise image generated by the ACF algorithm, when added with the experimental noises, makes the algorithm impossible to employ in practice. These conclusions reinforce the points observed from the initial simulation results in Chapter V.

b. IMG algorithm

Figure 65a and b show the horizontal and vertical positions of the target spots relative to the hologram dimensions, respectively, for the holograms generated with the IMG algorithm. In both graphs, it can be seen that there is excellent agreement between the simulation results, the experimental results, and the desired positions.

As can be seen in Figure 65a and b, the differences between the experimental positions and the desired / simulation positions stay almost constant across the range of hologram dimensions. This shows that they are caused by imperfect calibration in determining the extent of the steerable region in the captured frames (*cf*. Chapter VI.B.1)

With the relative simulated source-size changes for the different array sizes, the excellent target-positioning performance of the IMG-generated holograms shows that the algorithm works well for both smaller and larger sources. Since smaller sources would provide more spatial coherence in the illumination, whilst the larger sources emit less coherent light, the results imply that the IMG algorithm is effective with sources of various

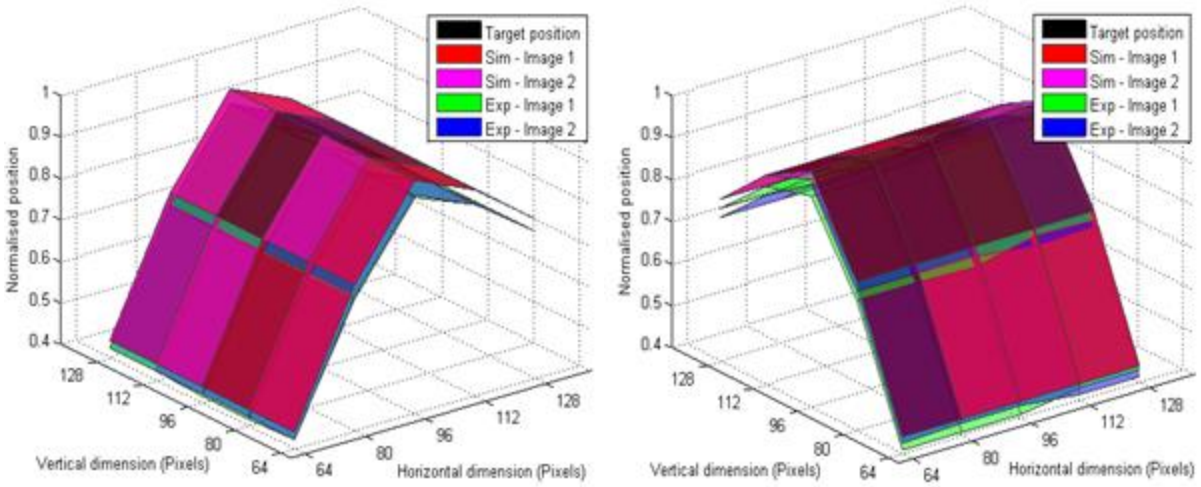

Figure 65. Expt 1 - Normalised (a) Horizontal and (b) Vertical positions of the two target spots for IMG-generated rectangular holograms

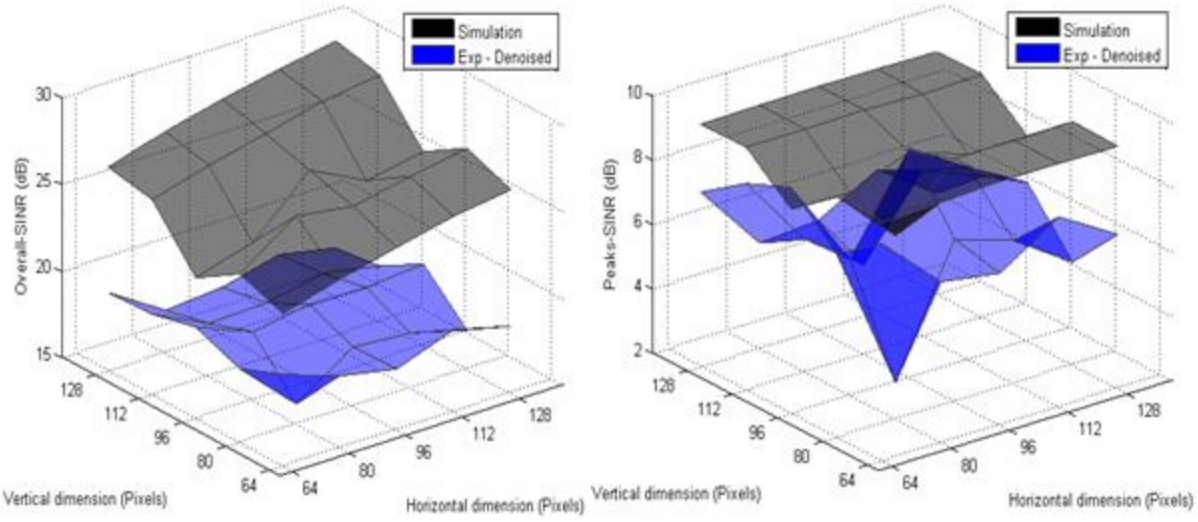

(a) (b)

Figure 66. Expt 1 - (a) Overall-SNR and (b) Peaks-SNR of the two target spots for IMG-generated rectangular holograms

degrees of coherence.

Since the source size (*i.e.* LED size) in the experiment is constant whilst the size of the source used in generating the holograms changes, the good experimental performance of the holograms thus shows that once generated, the holograms can be used to steer different sources with various intensity distributions.

Figure 66a and b show the Overall-SNRs and Peaks-SNRs for the target spots steered by the IMG-generated holograms.

The simulation Overall-SNRs in Figure 66a display the characteristic increase with respect to the hologram sizes which is caused by relative ease of the holograms in gathering optical power for smaller sources. The dip at the vertical dimension of 96 pixels is explained by the distortion in target-spot shapes caused by high-order aliasing at the border of the steerable region. Thus when the mask is applied for SNR calculation, large parts of these distorted target spots are masked out, thus lowering the SNR. This dip does not appear when

the horizontal dimension is 96 pixels. This can be explained by the shape of the simulation source, which penalises vertical distortions more.

The experimental Overall-SNRs in Figure 66a have values of about 20dB. The captured frames have 8-bit resolutions and thus a maximum SNR of 24dB, this 20dB thus means an average field noise of 2 (arbitrary) units against an average target-spot intensity of the maximum 256. Therefore, this is very high performance of the IMG-generated holograms in gathering the optical power into the target spots.

The experimental Overall-SNR remains relatively flat across the hologram sizes and does not exhibit the increase with the hologram size as the simulation one does. The reason may be that the CCD noise of the camera is greater than the hologram noise, so improvements cannot be seen.

Figure 66b shows the Peaks-SNRs for the target spots against the 2^{nd}-orders. It can be seen that the simulation and the experimental values are almost in excellent agreement, with the experimental Peaks-SNRs about 2dB lower in most cases due to the CCD noise. The uncharacteristic dip at the 80-by-80 hologram is due to the fact that this particular hologram gathers all the hologram noise into two noise peaks, and thus lowers the Peaks-SNR.

The results for simulation and experiment in this section show the IMG algorithm performs beam-steering well across a range of hologram dimensions and for different source sizes, *i.e.* different degrees of coherence in the illumination.

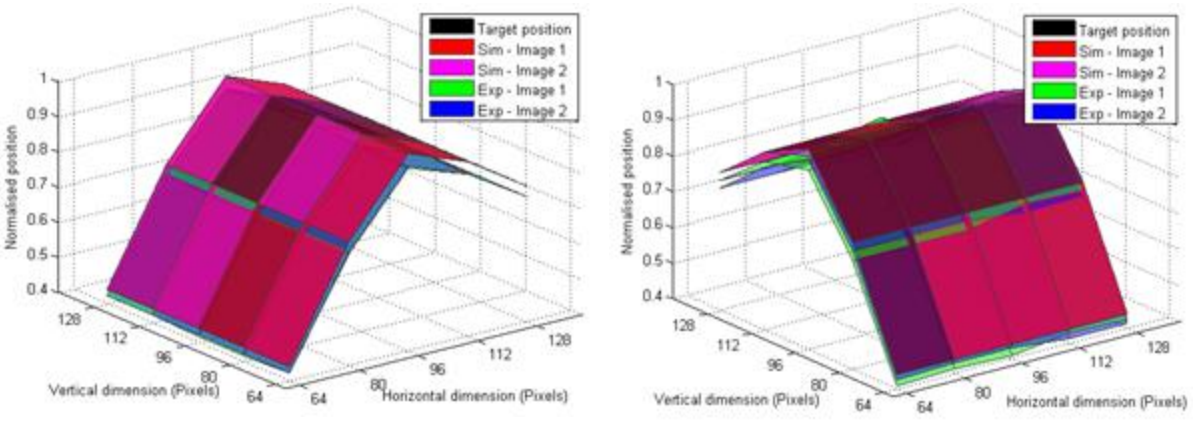

(a) (b)

Figure 67. Expt 1 - Normalised (a) Horizontal and (b) Vertical positions of the two target spots for MIXED-generated rectangular holograms

c. MIXED algorithm

Figure 67a and b show the horizontal and vertical positions of the target spots relative to the hologram dimensions, respectively, for the holograms generated with the MIXED algorithm as described in Chapter V. Figure 68a and b show the Overall-SNRs and Peaks-SNRs for the target spots steered by these MIXED-generated holograms

It can be seen that Figure 67 and Figure 68 are almost identical to Figure 65 and Figure

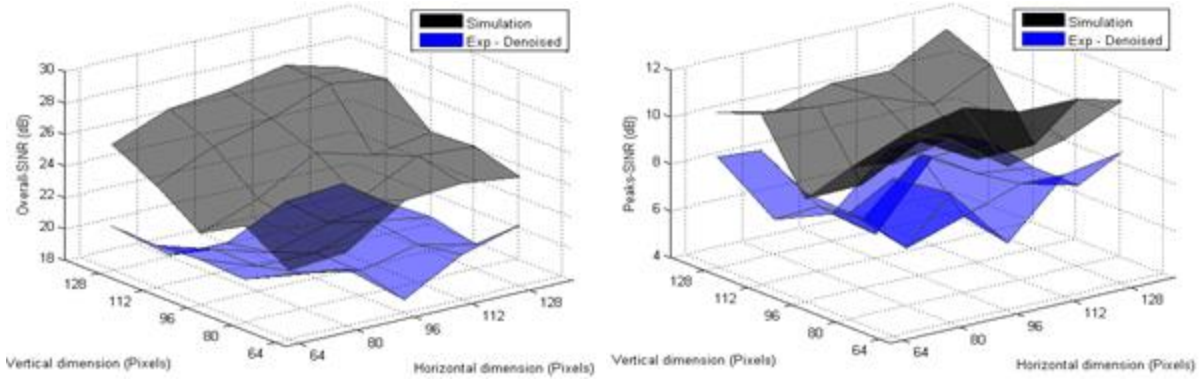

(a) (b)

Figure 68. Expt 1 - (a) Overall-SNR and (b) Peaks-SNR of the two target spots for MIXED-generated rectangular holograms

66 for the IMG algorithm, respectively. This agreement shows that the MIXED algorithm gives similarly high performance in beam-steering as the IMG does. This is because the IMG element in the MIXED criterion dominates the second part of the search, where the fine details of the intensity distribution are optimised.

Thus the MIXED algorithm can also be concluded as being highly effective in generating beam-steering holograms across a range of hologram dimensions and for different degrees of coherence of the source.

3. Experiment 2 – Variable target positions

A second experiment is conducted to investigate the ability of the holograms to steer the target spots to different positions in the image plane. The holograms are generated with the MIXED algorithm only, as this algorithm is shown to offer the best beam-steering performance and fastest generation time. The holograms are of the same dimensions, fixed at 128-by-128 pixels. The target positions are changed incrementally by 10 pixels from hologram to hologram, in either the horizontal or vertical direction.

Figure 69a and b show the horizontal and vertical positions of the target spots relative to the hologram dimensions, respectively. It can be seen that there is excellent agreement between the simulation results, the experimental results and the desired positions.

Figure 70a and b show the Overall-SNRs and Peaks-SNRs for the target spots. In Figure 70a, the relative flatness of both the simulation SNRs and the experimental SNRs indicates that the power performance of the MIXED-generated holograms is consistent and robust

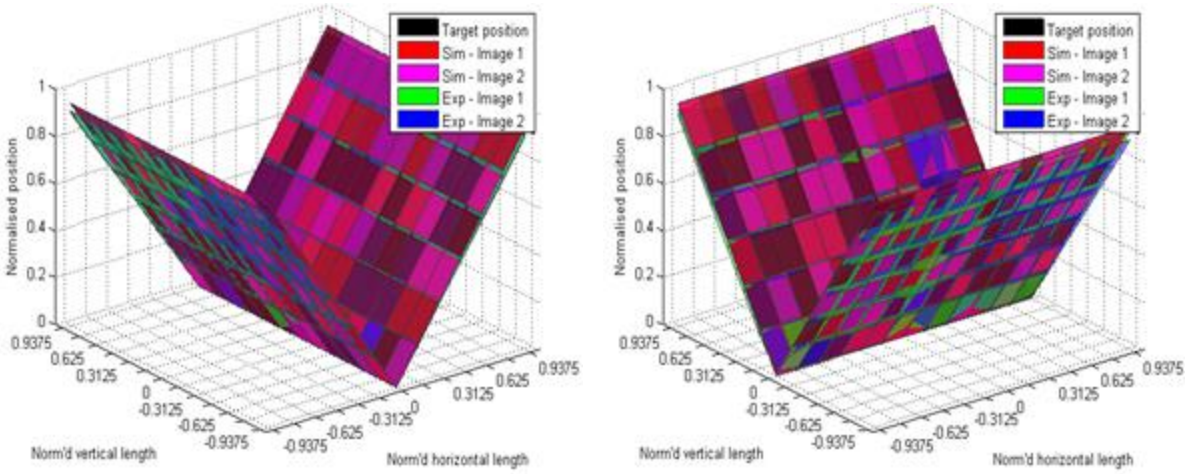

Figure 69. Expt 2 - Normalised (a) Horizontal and (b) Vertical positions of the two target spots for MIXED-generated square holograms

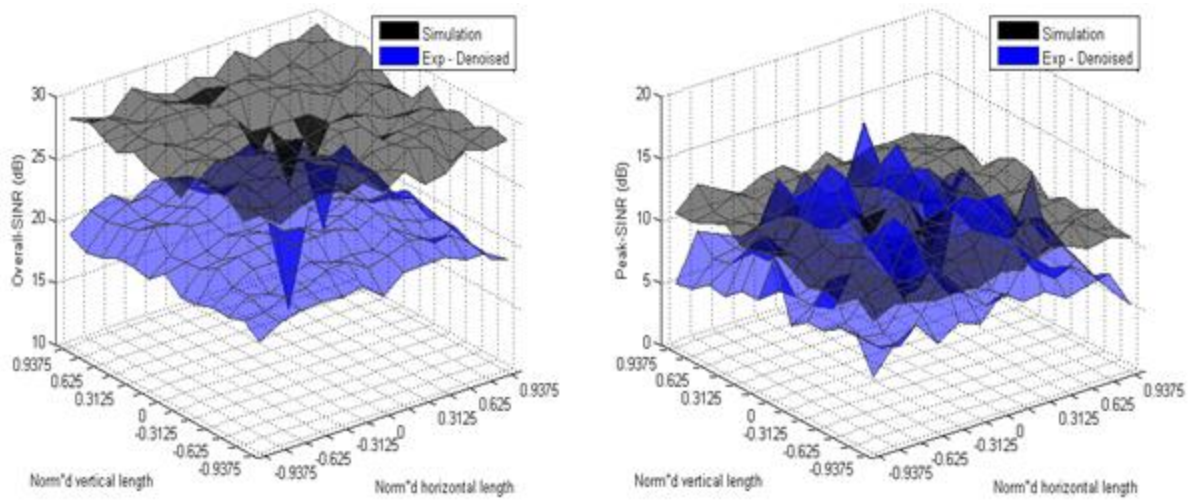

(a) (b)

Figure 70. Expt 2 - (a) Overall-SNR and (b) Peaks-SNR of the two target spots for MIXED-generated square holograms

across the whole range of target positions. The experimental SNRs are ~20dB which as discussed are very good values with the 8-bit quantisation.

The two significant dips in the experimental SNRs occur at two locations: when the target position is the unsteered spot (zero-order) which is subsequently masked out (*cf*. Chapter VI.B.3) hence the low SNR; and at the position where the noise peaks cluster densely near the target spots, causing wrong calculation of target-spot power.

In Figure 70b, the flat 10-dB simulation Peaks-SNRs surface indicates that the relative power distribution within the image is stable for all target-spot positions across the image-plane. This is also reflected in the experimental Peaks-SNR results, except for near the borders of the steerable region where the Peaks-SNR drops by 3-5 dB, likely due to this being the steering limit by the SLM thus having lower efficiency.

The results in this section thus show that the MIXED algorithm is able to steer the target spots to any position within the image-plane with good and consistent power performance.

D. Simulated MIMO steering demonstration

In the previous sections, both simulation and experimental results have shown that in the single-source system, the autocorrelation-based algorithms can steer image spots with excellent positioning and power-concentrating performance. To demonstrate the use of beam-steering to alter the channel matrix ***H*** in MIMO-OWC, a MATLAB simulation of beam-steering is conducted for an imaging MIMO configuration.

In addition, to assess the channel-design with holograms when there is a scatterer present in the optical path, the simulation is set up with a phase screen representing a scattering phase distribution.

1. Simulation set-up

a. Overview

Figure 71 shows a schematic of the MIMO beam-steering simulation. Light from the 2

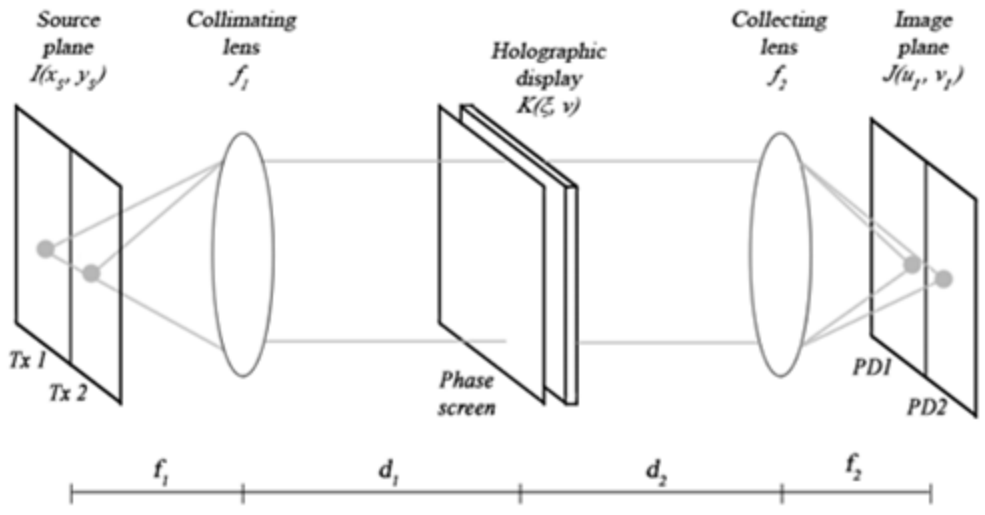

Figure 71. Schematic of beam-steering for a 2-Tx 2-Rx imaging MIMO system

identical Tx on the source plane is parallelised by a lens, and propagated to a phase screen, then to a hologram placed immediately behind the screen. The holographically-modulated light is then collected by another lens and focused onto two photo-detectors (PDs) acting as Rx on the image plane. The individual optical link between each pair of Tx-Rx sets an element in the channel matrix $\underline{\boldsymbol{H}}$ of the system.

Each beam-steering hologram displaces both Tx images by the same amount in the image plane, and generates a corresponding 2-by-2 channel matrix $\underline{\boldsymbol{H}}$. Each of these channel matrices is then input to the MIMO-OWC simulator in Chapter III (in place of the ZEMAX-simulated matrix) which then runs and outputs the system BER as the performance of the corresponding channel as designed by the corresponding hologram.

b. Simulation procedure

To steer the Tx images to different positions in the image plane using holograms, the following procedure is executed:

1. For each position, a target displacement of how much the Tx images should be steered by is input to the hologram generator.
2. A beam-steering hologram is generated by the MIXED algorithm (shown to offer the best hologram-design performance).
3. Replays of this hologram are simulated with each Tx enabled in turn. From each replay, the PD outputs are calculated and used as a column in $\underline{\boldsymbol{H}}$. These columns are then combined to give the channel matrix corresponding to the hologram.
4. The resulting $\underline{\boldsymbol{H}}$ is input into the MIMO-OWC simulator in Chapter III and this simulator is run to get the system BER.

c. Simulation parameters

For the target positions, the whole replay field is divided into a 128-by-128 array each pixel of which then becomes a target position. The hologram size is fixed correspondingly at 128-by-128 pixels. Table 7 shows the parameters used in this simulation.

System pixilation	Target positions (pixel)	Horizontal	-64 to +64
		Vertical	-64 to +64
	Hologram size (pixel)		128 by 128
Generation loop (*cf.* Chapter IV.C.2)	Error tolerance		0
	Number of iterations		10 * (number of pixels)
	Cooling parameters		(see Eq.126)
Propagation constants (*cf.* Eq.92)	Intensity multiplier $\frac{1}{\bar{k}^6 f_2^2}$		1
	Source-plane scaling $\frac{f_1}{\bar{k}}$		1
	Image-plane scaling $\frac{f_2}{\bar{k}}$		1
Data stream	Symbol length		Stream for each Tx is 50 repetitions of 1000 pseudo-random symbols
	Modulation scheme		Full-depth NRZ-OOK
Rx processing	Sampling		20 samples per symbol
	Analogue-to-Digital simulation	Amplitude	0.0001
		Resolution	16 bits per sample
	AWGN power		10^{-16}.(mod.amp)^2

Table 7. Parameters used in the MIMO beam-steering simulation

2. Simulation results

Following the procedure in the previous section, three simulations are carried out:

In the first, the MIMO channel design without a scatterer is simulated by setting the screen to all 0-phase.

In the second, it is assumed that the phase distribution of the scatterer is unknown. This is simulated by using different phase screens for Step 2 and Step 3 in Chapter VI.D.1.b. In Step 2, the holograms are generated with a 0-phase screen, and with a screen whose random phases are uniformly distributed between $-\pi$ and π. Step 3 uses a screen with random phases following a Gaussian distribution with mean 0 and standard deviation $\pi/2$.

In the third, the situation where the phases of the scatterer can be known correctly is simulated by using the same phase screen in the hologram generation (Step 2) and in the channel-matrix calculation (Step 3). The random phases of the screen are uniformly distributed between $-\pi$ and π.

Figure 72 shows the image-plane intensity distribution for the case of no steering, with

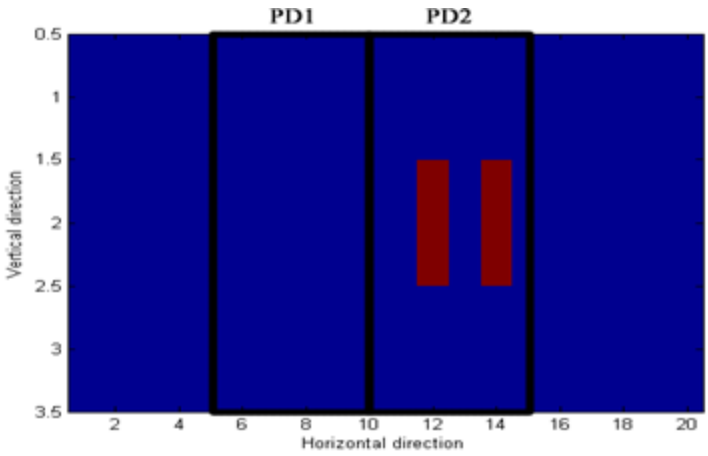

Figure 72. Simulated unsteered replay marked with the photo-detectors: Red—Tx image, Blue—Background

the areas covered by the 2 PDs marked in black. It can be seen that the two independent Tx both fall on PD2, whilst PD1 receives no optical power. Thus MIMO-OWC does not work for this reference case.

a. No scatterer

Figure 73a and b shows the variations of the condition number $\mathrm{cond}(\underline{\boldsymbol{H}})$ of the channel matrix and of the system BER, respectively, with respect to the target displacements when no scatterer is present. It can be seen that there is virtually no change when the Tx images are displaced vertically, as expected from the orientation of the PDs in Figure 72.

In the horizontal direction, the system performance is worst when no steering occurs, as expected. As the Tx images are displaced horizontally, the performance goes through alternate phases of improvements and deterioration.

With the Tx images displaced such that the two Tx fall on 2 PDs, the overlap is reduced, resulting in improved system BER. When the Tx images are displaced by too large a horizontal distance, they start to overlap onto the same PD again (moving to the negative

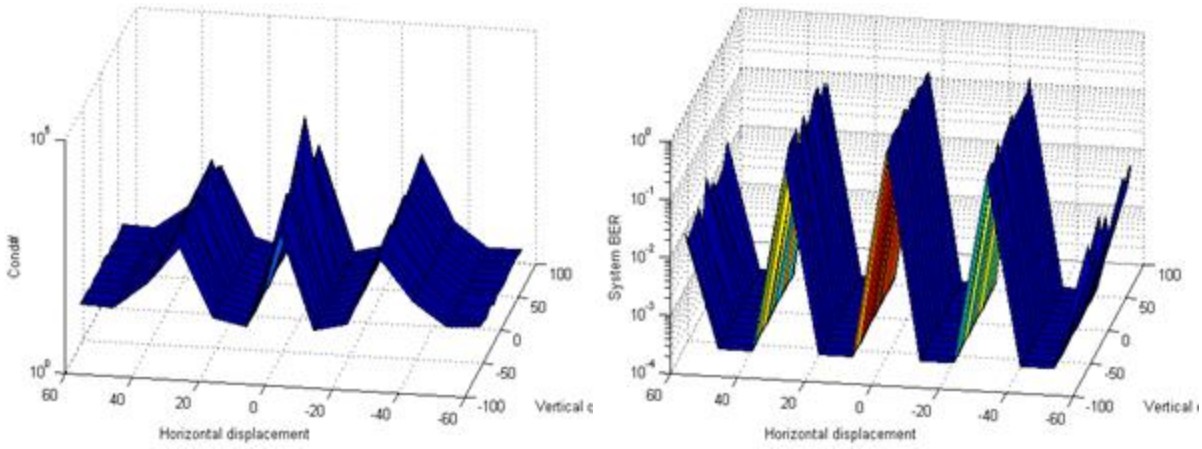

(a) (b)

Figure 73. (a) $\mathbf{cond}(\underline{\boldsymbol{H}})$ and (b) simulated system BER versus displacement steps by beam-steering without phase screens in hologram-generation or propagation

direction) or out of the PD array altogether (moving to the positive direction.) The increased overlap results in increases in the system BER increases.

It is interesting to note that: beyond certain horizontal displacements, the performance again improves. This is explained by the fact that the noise peaks caused by the hologram in the replay (*cf*. Figure 62) act as the secondary spots for the Tx images, thus reducing the overlap level and improving the performance.

The clear BER improvements achieved with beam-steering thus shows that holograms can be used to design the channel matrix in order to reduce Tx-image overlaps and improve MIMO system performance. The simulation results also show that the noise peaks caused by the holograms are desirable as they can act as secondary images to help reduce overlaps.

b. Unknown phases of the scatterer

Figure 74a and b shows the condition number $\mathrm{cond}(\underline{\boldsymbol{H}})$ of the channel matrix and the system BER, respectively, with respect to the target displacements when holograms generated without scatterers are used with a Gaussian-phase screen in Step 3. It can be seen that the performance trend similar to that in Figure 73 can still be observed.

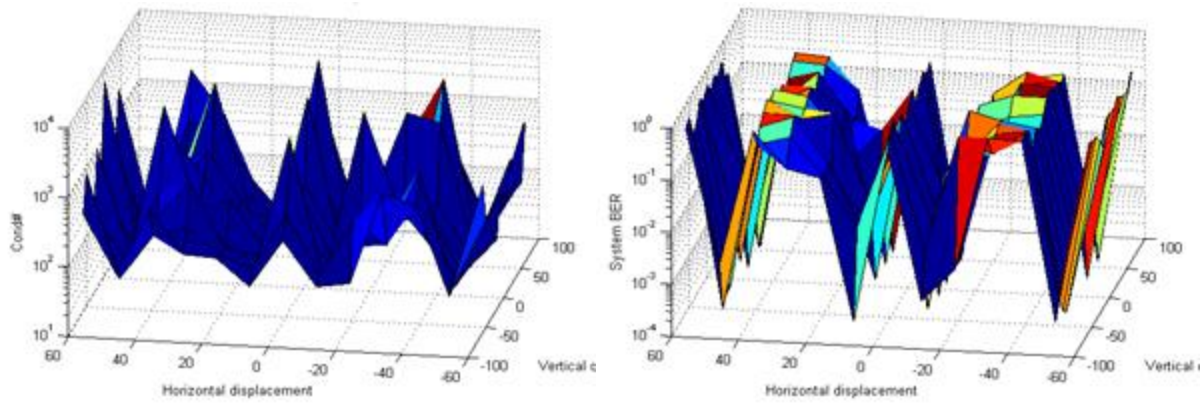

(a) (b)

Figure 74. (a) $\mathbf{cond}(\underline{\boldsymbol{H}})$ and (b) simulated system BER versus displacement steps by beam-steering through a random phase-screen by holograms designed with no phase screen

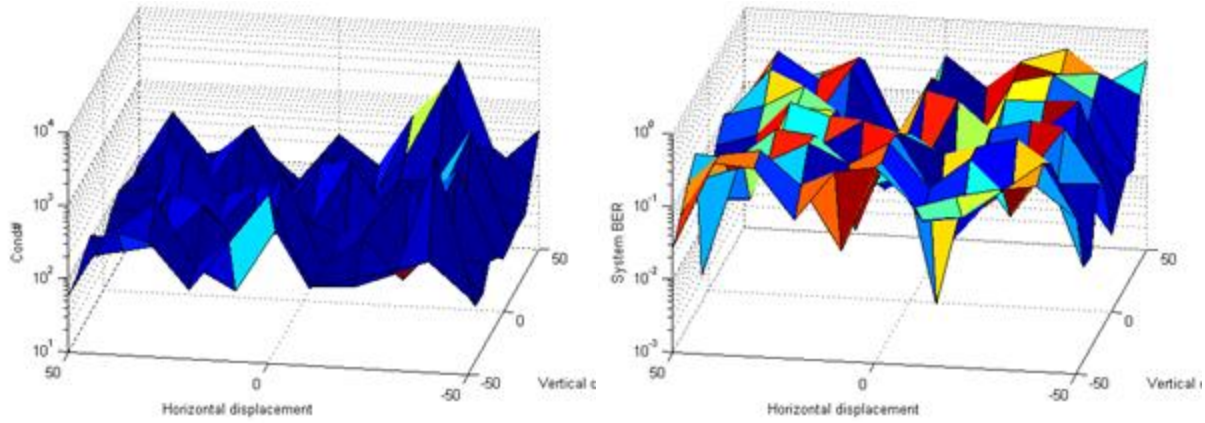

(a) (b)

Figure 75. (a) $\mathbf{cond}(\underline{\boldsymbol{H}})$ and (b) simulated system BER versus displacement steps by beam-steering through a random phase-screen by holograms designed for a different screen

However, the broad crests and narrow troughs of the system BER in Figure 74b show that the overlap is high over larger ranges of horizontal displacements, and the overlap is low for smaller ranges. This is explained by the mismatch between the expected phases used in Step 2 (*i.e.* no scatterer) and the phase distribution of the scatterer in the propagation steps.

Figure 75 shows the same variations, when Step 2 uses a phase screen with random uniformly-distributed phases and Step 3 uses a Gaussian-phase scatterer. It can be seen that the system BER is high, with no improvement across the displacement range. This poor performance is explained by the fact that the holograms are so optimised for one scatterer that another scatterer will cause the replays to become highly noisy, causing similar overlaps in both PDs, highly ill-conditioned $\underline{H}$ and poor system-BER.

It thus shows that with unknown phase distributions of the scatterer, beam-steering with holograms generated without a scatterer can still offer a reasonable performance in channel design.

c. Known phases of the scatterer

Figure 76a and b show cond($\underline{\boldsymbol{H}}$) and the system BER, respectively, with respect to the target displacements when the known phase distribution of the scatterer is used in hologram generation. The clear BER improvement similar to that achieved in the case of no scatterer thus shows that hologram beam-steering can correct for known scattering phases[††††].

The low performance beyond the crest in the positive direction in both graphs in Figure 76 can be explained by the fact that the scattering phases disrupt the secondary images caused by noise peaks. With the primary Tx images already out of the PD array, this lack of secondary images means no link is established, resulting in the high BER.

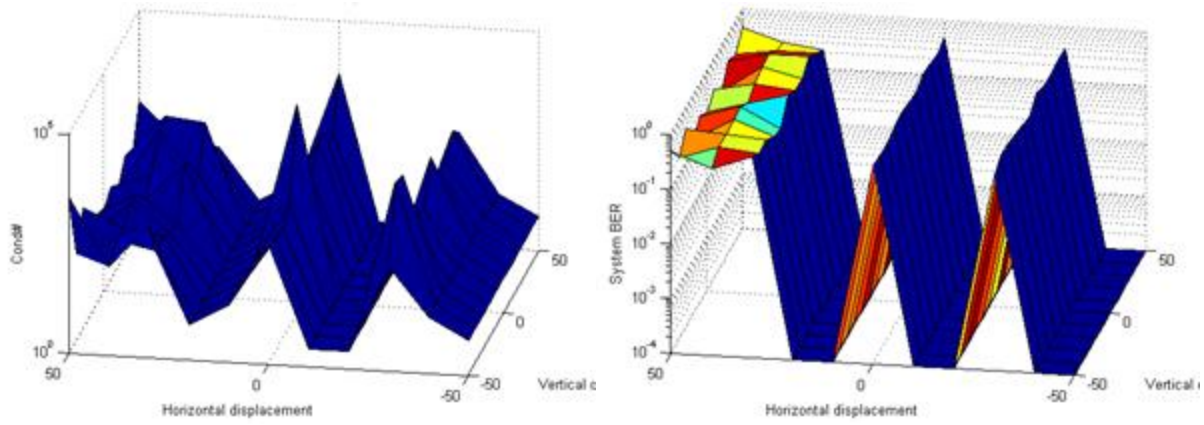

(a) (b)

Figure 76. (a) **cond**($\underline{\boldsymbol{H}}$) and (b) simulated system BER versus displacement steps by beam-steering with the same random phase screens in hologram-generation and propagation

[††††] The difficulty of estimating the phase distribution with large photo-detectors is treated in Appendix B.

E. Conclusions

The experimental performance of the holograms generated with the autocorrelation-based algorithms are described and compared with the simulation results. Table 8 shows the summary of the performance of the three algorithms, as verified experimentally.

Algorithm	Target-spot positioning	Target-spot power-concentration	Generation time
ACF	Bad due to large background noise	Bad due to large background noise	Slower
IMG	Good	Good	Slower
MIXED	Good	Good	Faster

Table 8. Summary of performance of the ACF, IMG and MIXED algorithms

Simulation with a 2-Tx 2-Rx MIMO system demonstrates that holographic beam-steering can be used to design the channel matrix in order to reduce Tx-image overlaps and improve the system performance, even with unknown scattering phases. The results also show that if the scattering phases are known, the holograms can be highly optimised for these phases to offer excellent overlap-reduction performance.

Chapter VII. **Conclusions and Future work**

A. Conclusions

MIMO-OWC is a promising technology likely to complement or replace RF-based systems in future WLANs [11]. The strength of the MIMO technique lies in its channel diversity, which allows data-rates many times higher than possible with SISO. An experiment by the author and colleagues has shown that a lab-based MIMO-OWC system using only 2 Tx was able to achieve 200 Megabits/s throughput [96], and a 4-Tx 9-Rx system could achieve in excess of 1 Gigabits/s [116].

Unlike a SISO system where optical-power constraint is the most important limiting factor, in a MIMO system, MIMO-detection methods play a more important role than power by reducing cross-talks between channels. Amongst the several MIMO-detection methods reported in Chapter II.B, MMSE is found to be the preferred algorithm for implementation due to its robustness in high-overlap scenarios where the channel matrix is ill-conditioned. And the effects of symbol detection on MIMO detection dictate that for the Rx processing, the detection should be performed after MIMO-detection. A corollary is that ZF-based detectors are more suitable for amplitude-keying modulation schemes, whilst MMSE would require modulation schemes where the signals are approximately white Gaussian noise such as OFDM.

To implement such MIMO-detection methods, the channel matrix $\underline{\boldsymbol{H}}$ as input data must be known. Based on the model described in Chapter II.A of a line-of-sight MIMO-OWC system, Chapter II.C presents an analytical channel-matrix model for the MIMO systems, and introduces a simple deterministic estimation algorithm for $\underline{\boldsymbol{H}}$, which is found to be effective in both simulation and experiments.

To measure the performance of a particular geometry for MIMO communications, three metrics have been proposed: the condition number, the Signal-to-Interference-and-Noise Ratio (SINR) and the SISO-equivalent Signal-to-Noise Ratio (SNR^{SISO}.) These metrics are all based on the channel matrix, and independent of the signals. Simulated transmission through the MIMO-OWC system using a MATLAB-based program shows that the channel SINR is the most appropriate metric for geometry performance as it correlates well with the ultimate transmission metric of BER. The simulation also illustrates that the condition number of the channel matrix, although not possessing a well-defined relationship with the system performance, can also be used as a rough predictor of the performance.

Also, from the investigation in Chapter III.A.1 of the formula for system Bit-Error-Rate (BER), it has been predicted that the overall performance of a MIMO system is mostly dominated by its worst channel. This theoretical prediction has been subsequently confirmed with the data obtained from simulation. Combined with the insights on the channel SINR, this result is significant in that: to improve the overall system performance, the most effective way is to maximise the SINR of the worst channel.

As the channel SINRs are functions of the channel matrix, which in turn is a representation of the level of overlaps of the different transmitter images over the receiving photo-detectors, one of the possible solutions to improving the SINRs is to steer the transmitter images such that their distributions over the photo-detectors reduces the overlaps. In a MIMO-OWC system using visible light sources such as light-emitting diodes, this requires a means of beam steering for partially-coherent light.

Through a theoretical analysis of using holograms for beam steering with partially-coherent light, it is found in Chapter IV.B that by using a two-lens configuration to parallelise and collect partially-coherent light at the source and the image respectively, a mathematical

relationship is established between three quantities: the source and image intensity distributions, and the autocorrelation of the hologram.

This mathematical relationship leads to the development of two computational hologram-design algorithms—the ACF and the IMG algorithms—to obtain a quantised hologram with the desired beam-steering capability. To take advantage of the strengths of both ACF and IMG, a third algorithm, MIXED, is also proposed as a mixture of the ACF and IMG algorithms. These algorithms differ from the commonly used hologram-generating algorithms in that their cost functions are all based on the autocorrelation of the hologram, and the performance comparison is done at the hologram plane instead of the image plane.

This has significant speed advantage. Specifically, the MIXED algorithm is shown to be 33-50% faster than alternative methods.

To assess the proposed algorithms' performance in beam-steering, a simulation-based study in Chapter V and a corresponding experiment in Chapter VI have been carried out.

The MIXED algorithm is effective in generating beam-steering holograms across a range of hologram dimensions and for different degrees of coherence in the illumination. This algorithm is also able to steer the 1^{st}-orders to any position within the image-plane with good and consistent power performance, thus allowing reasonable expectations of the power distribution for positions not yet simulated.

Thus when also considering its superior search-time performance, the MIXED algorithm is the best of the three autocorrelation-based hologram-generation algorithms.

Simulation with a 2-Tx 2-Rx MIMO system demonstrates that holographic beam-steering can be used to design the channel matrix in order to reduce Tx-image overlaps and improve the system performance, even in the presence of a phase scatterer of unknown distribution.

Combining these findings, a strategy can be devised to optimise the throughput of an imaging MIMO-OWC system for a given transmitted power. Firstly the transmitter images on the receiver array would be modelled theoretically using the hybrid geometric-optic model proposed. Then the channel matrix would be optimised for the different possible placements of the transmitter images to reduce the overlaps. Subsequently, the placement associated with the optimised channel matrix would act as the target position and allow a hologram to be pre-generated with the autocorrelation-based MIXED algorithm. This hologram, when loaded onto an SLM, would steer the transmitter images to the desired position, thus improving the channel matrix and the system performance.

In conclusion, it is hoped that the research described in this thesis has yielded useful insights in optimising MIMO-OWC systems to improve their already-impressive performance.

B. Future work

This thesis has been about using linear models to understand the MIMO geometry, and applying active beam-steering on the transmitter images as a collective whole to improve the system performance. Future research may further advance the MIMO-OWC performance by examining the following aspects:

a. System geometry with adaptive MIMO-detection techniques

The recursive processing of adaptive techniques, such as V-BLAST, allows the information acquired in the processing of one channel, *e.g.* signal power, to be available to the processing of the other channels. This makes the acquired knowledge better utilised for the signal recovery than with the linear MIMO-detection techniques reported in this thesis [82, 83]. However, adaptive techniques do not allow easy algebraic manipulations, consequently making optimisation difficult due to lack of prior models. By studying the geometrical implications of these adaptive MIMO-detection techniques, the desired form of the system geometry could be understood, thus allowing optimisation of the channel matrix in order to maximise the MIMO-OWC performance.

b. Independent holographic beam-steering for multiple Tx

In beam-steering with space-invariant holograms (such as in this thesis), the relative positions between the transmitter images are preserved since the same linear translation is applied to every point within the group. Therefore, depending on these relative positions, image overlaps may be reduced but not totally eliminated.

For better geometry optimisation, there should be a degree of freedom in steering the individual images. The simplest solution might make use of space-variant holograms which would operate differently for the different transmitters [55].

Alternatively, a wavelength-division multiplexing scheme could be employed so that the same physical hologram would have different effective spacing under different frequencies. This can be seen in Eq.92 where different values of the wave-number k would give differently scaled images.

c. Holographic beam-shaping for channel-matrix improvement

The formula in Eq.92 shows that partially-coherent beam-shaping can be also performed with holograms, and has been shown experimentally in [70]. In the context of MIMO-OWC improvement, this capability can be used to alter the shapes of the transmitter images such that an image would more likely to 'fit' wholly within the area of a photo-detector, thus reducing overlaps which in turn increases the channel matrix's SINRs.

d. Algorithm speed

As noted in Chapter V, despite significant speed improvements over the common direct-binary-search, the autocorrelation-based algorithms still take too much time to run, although much faster than the direct-binary-search. Although beam-steering can use pre-generated holograms, the speed of the algorithm still has to be improved through finding better convolution calculations so that bigger holograms do not take days to generate. This is currently the case with the complexity $\mathrm{O}(N^2 \log N)$ of the autocorrelation-based algorithms.

e. Possible changes to the algorithm implementation

For each of the operations described above, there are multiple other forms which can be implemented, usually independent of the rest of the program thanks to its modularity. Although not implemented in this simulation due to their complexity, for future research, those alternative implementations have the following advantages:

1. If the (continuously-valued) desired hologram is known to be very close to a certain quantised hologram and if the pixel can have more than 2 binary values, a more deterministic distribution than random initialisation can be chosen as K_{init} in order to make the initial state as close as possible to the desired hologram. One example is that when the desired hologram is known to be real and non-negative, K_{init} can be set as a quantised distribution of $\left|\sqrt{\tilde{R}_d}\right|$.
2. In the proposal step, the random selection of a pixel from the set of not proposed ones equates to having a binary distribution of proposal probability over all the hologram pixels. If the hologram performance is known to possess some certain kind of monotonicity with regards to the pixel values, then a different statistical distribution can be devised so that a pixel whose update is more likely to lead to improvement is correspondingly more likely to be proposed. Also, there may be some distributions of performance where having two or more pixels proposed per iteration can offer better improvement than updating a single pixel.
3. For the evaluation step, if some prior knowledge of the performance distribution can be had, a more directional or deterministic optimisation algorithm can be implemented instead of simulated annealing which has the tendency to 'jump over' minima, local or global, near the beginning of the search. As an example, if the error

distribution was known to be polynomial, a conjugate-gradient search would return the global minimum in no more than N steps, greatly reducing the search time.

4. Depending on the optimisation algorithm chosen as discussed in point (3) above, a different formula for the evaluation metric can be used: for example, should the search be conjugate-gradient, the evaluation metric can be the search error ε itself.

All these alternative forms are conditional on the desired search performance, as well as on some prior knowledge of the hologram-performance distribution.

Appendices

A. Acceptance probability in simulated annealing

Deterministic gradient-based optimisation suffers from the impossibility to escape local minima and thus works only with convex functions. For a function whose convexity is not guaranteed (either theoretically or empirically) probabilistic optimisation offers a convenient solution to the local-minima problem. The basis of probabilistic optimisation is that the move from one state to another has a non-zero probability. Thus it is possible for the optimiser to escape local minima to neighbouring states despite their higher values.

Simulated annealing [1] is one of such probabilistic-search techniques. It varies the acceptance probability P_{accept} of a new state according to a variable Δ measuring the improvements made between states, and a decreasing, non-negative 'temperature' T acting as a scheduler for the search to make sure that it will be increasingly difficult for the optimiser to jump to higher-valued neighbouring states, and eventually the search will terminate at some minimum. The variable Δ is positive when the new state is worse than the current state, and negative when the new state is better. Its magnitude represents the amount of improvement.

$$P_{accept} = f(\Delta, T) \qquad \text{Eq.119}$$

In simulated annealing, the algorithm starts off only slightly favouring the better state over the worse state. As the operation progresses, the improved state is increasingly favoured, and its acceptance becomes more probable. Simulation shows that the probability function proposed in [1] does not give satisfactory termination to the autocorrelation-based algorithms due to its rigid non-accepting of the worse-off states towards the end of the search.

The analysis to follow develops a new probability function that gives more control to the acceptance toward the end. The definition of simulated annealing is:

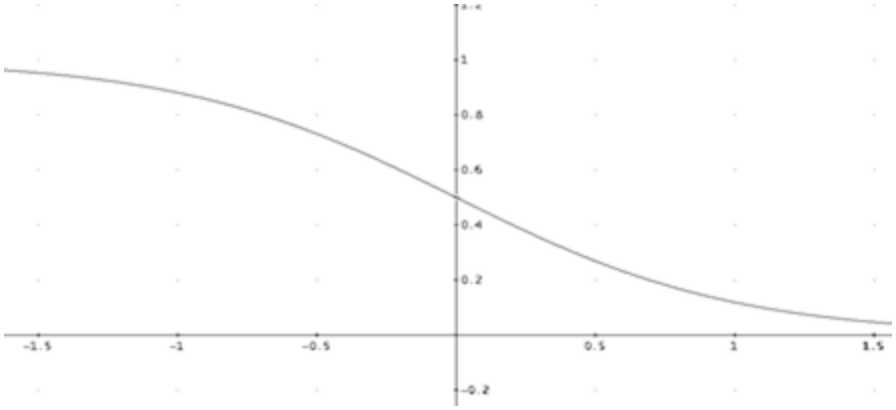

Figure 77. Plot of the hyperbolic $\mathbf{tanh}(-x)$ function

$$P_{accept} \to 0.5, \qquad T \to +\infty$$
$$\begin{cases} P_{accept} \to 0, & \Delta \to +\infty \\ P_{accept} \to 1, & \Delta \to -\infty \end{cases}, \quad T \to 0 \qquad \text{Eq.120}$$

Eq.120 can be rearranged into the following form:

$$\lim_{\Delta \to -\infty} P_{accept} = \lim_{\Delta \to -\infty} f(\Delta, T) = g_1(T): \begin{cases} g_1(0) = 1 \\ g_1(+\infty) = 0.5 \end{cases}$$
$$\lim_{\Delta \to +\infty} P_{accept} = \lim_{\Delta \to +\infty} f(\Delta, T) = g_2(T): \begin{cases} g_2(0) = 0 \\ g_2(+\infty) = 0.5 \end{cases} \qquad \text{Eq.121}$$
$$\lim_{\Delta \to 0} P_{accept} = f(0, T) = 0.5$$

Where the univariate boundary-functions $g_1(T)$ and $g_2(T)$ are monotonically decreasing and monotonically increasing, respectively.

From Eq.121, it can be seen that at any given T, $g_1(T) \geq 0.5 \geq g_2(T)$ with equality at $T = +\infty$. Since $P_{accept} \in [0,1]$, is continuous, and has to satisfy the boundary conditions in Eq.121, its plot versus Δ for a fixed $T = T_0$ should have a form similar to that in Figure 77, which is that of the hyperbolic $\tanh(-x)$ function. It can thus be immediately seen that a

function[‡‡‡‡] with the analytical form similar to that of $\tanh(-x)$ would satisfy the boundary conditions:

$$f(\Delta,T_0) = \frac{ae^{\Delta} + be^{-\Delta}}{ce^{\Delta} + de^{-\Delta}} \qquad \text{Eq.122}$$

Substitute Eq.122 into Eq.123:

$$\begin{gathered}\lim_{\Delta\to-\infty} f(\Delta,T_0) = g_1(T_0) = \frac{b}{d} \\ \lim_{\Delta\to+\infty} f(\Delta,T_0) = g_2(T_0) = \frac{a}{c} \\ f(0,T_0) = 0.5 = \frac{a+b}{c+d}\end{gathered} \qquad \text{Eq.123}$$

Solving Eq.123 for the factors a, b, c, and d, the function $f(\Delta,T)$ becomes:

$$f(\Delta,T) = \frac{g_2(T)e^{2\Delta} - g_1(T)\dfrac{1-2g_2(T)}{1-2g_1(T)}}{e^{2\Delta} - \dfrac{1-2g_2(T)}{1-2g_1(T)}} \qquad \text{Eq.124}$$

It is obvious that $f(\Delta,T)$ as given in Eq.124 satisfies all boundary conditions in Eq.121. The gradient of $f(\Delta,T)$ at $\Delta = 0$ is:

$$\frac{\partial}{\partial\Delta} f(\Delta,T)\Big|_{\Delta=0} = 2\frac{1-2g_2(T)}{2g_1(T)-1}\frac{g_2(T)-g_1(T)}{\left(1+\dfrac{1-2g_2(T)}{2g_1(T)-1}\right)^2} \qquad \text{Eq.125}$$

It can be seen that the magnitude of this gradient depends on the factor $\gamma = 2$ which is the gradient at $\Delta = 0$ of $e^{2\Delta}$. When this factor increases, the gradient magnitude increases for any given T, and P_{accept} becomes more sensitive to changes in Δ. To make P_{accept} increasingly sensitive to Δ as the operation progresses, the factor γ can be an inversely-varying function of the decreasing temperature T, such as $\gamma = {}^{1}/_{T}$.

[‡‡‡‡] There are of course infinitely many functions whose plots satisfy the conditions in Eq.121.

From Eq.121 to Eq.124, it can be seen that $g_1(T)$ and $g_2(T)$ are independent boundary functions which only have to satisfy their own asymptotic conditions as in Eq.121. The larger their rates of approaching the asymptotic value of 0.5 (with respect to T), the bigger the range of T in which $P_{accept} \cong 0.5$. In other words, as T decreases with progress of the operation, larger rates of asymptotic approach mean that the more-or-less random acceptance of new states takes place over more iterations, as seen in Figure 78 with $g_1(T)$ and $g_2(T)$ taking exponential forms with respect to T.

As the operation progresses and the temperature T decreases, if the approach rate to the asymptotic value 0.5 of either boundary functions increases, the random-acceptance period is extended for the relevant sign of Δ. Therefore, the difference between the decrease rate of T (the 'cooling rate' of simulated annealing) and the increase rate of asymptotic approach of the boundary functions controls the termination of the random-acceptance period. Notably, if the latter is larger than the cooling rate, the random acceptance extends to the whole operation.

Figure 79a shows the visualisation of the dependence of P_{accept} on Δ and T, according to Eq.124. In this plot, $g_1(T)$ and $g_2(T)$ take exponential forms and have different asymptotic

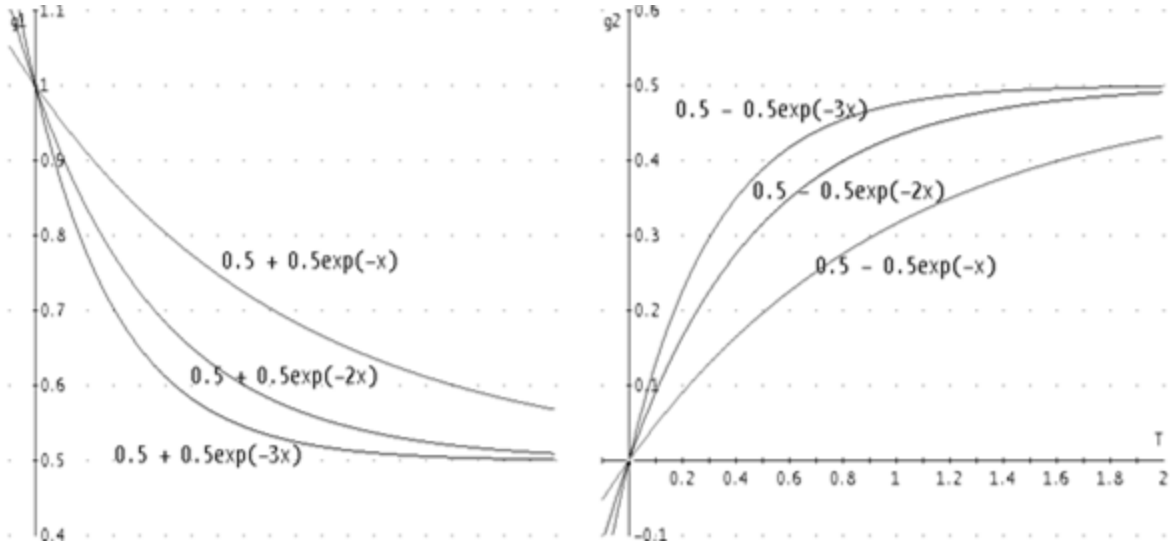

(a) (b)

Figure 78. Exponential forms with respect to $\boldsymbol{T}$ of (a) $\boldsymbol{g1}(\boldsymbol{T})$; (b) $\boldsymbol{g2}(\boldsymbol{T})$

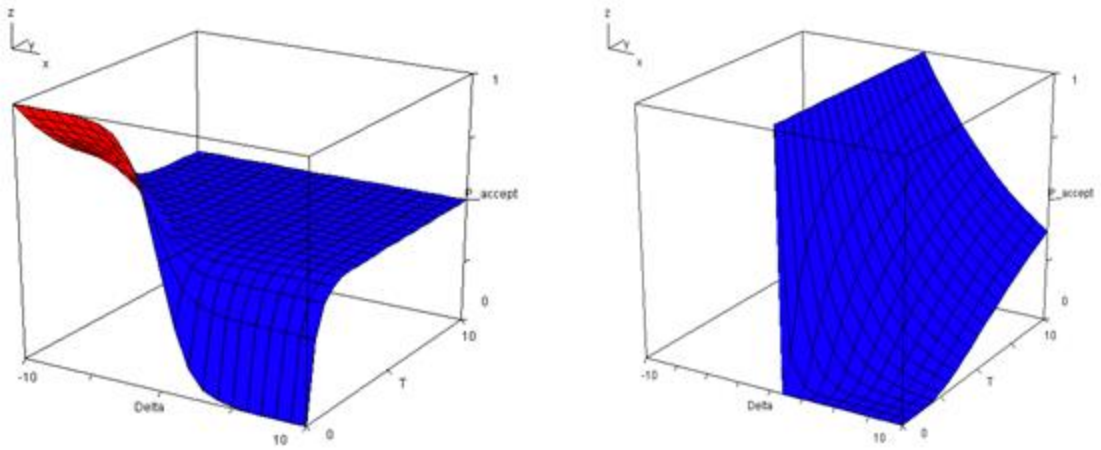

(a) (b)

Figure 79. Plot of $\boldsymbol{P_{accept}}$ with respect to Δ and $\boldsymbol{T}$ according to (a) Eq.124; (b) [1]

approach rates as demonstration of their independence from each other. Compared with the Boltzmannian formula of P_{accept} [1] visualised in Figure 79b, the formula in Eq.124 is less sensitive to values of Δ at high T, but much more sensitive at low T. This means that early on in the operation, Eq.124 behaves more like random acceptance and less like a gradient search than that in [1]. But as the operation progresses, its pronounced *tanh*-like form at low T (see Figure 79a) provides the flexibility to escape local minima, which the Boltzmannian formula cannot afford due to its tending to the infinite-well shape (evident at $T \to 0$ in Figure 79b).

One of the solutions to the random-acceptance issue is to control the schedule of the decreasing temperature T so that the random acceptance terminates relatively early on in the operation. As can be seen from Figure 79, this early termination implies that the temperature T must drop significantly over a relatively few iterations, whilst over the rest of the operation, it decays slowly, corresponding with P_{accept} being more sensitive to Δ. Conceptually, this variation is analogous to an exponential-decay function, thus hinting that T can take the form of $a\exp(-bx)$ where x is a variable representing the iteration progress.

As discussed before, the termination of the random acceptance can also be controlled by choosing appropriate decay rates for the boundary functions $g_1(T)$ and $g_2(T)$. These rates

can also be functions of T as an adaptive means of controlling the asymptotic approaches. However, simulations show that fixed values perform well.

The probability of accepting a new state which is neither better nor worse than the current state is assumed to be 0.5 in this analysis (*cf.* Eq.121 and Eq.123). This probability, however, can be changed to a different value, $1/\mu$, to reflect 'encouragement' or 'discouragement' of moving to a performance-wise identical state. The results obtained with such a probability would be identical in formulation to those presented in this section, with $\big(1-2g_2(T)\big)/\big(1-2g_1(T)\big)$ replaced with $\big(1-\mu g_2(T)\big)/\big(1-\mu g_1(T)\big)$.

In the hologram-generation operation, the following formulas and values are used, as found through empirical adjustments:

$$\begin{gathered}\Delta = e_n(\Psi) - e_{n-1}(\Psi) \\ T = 300\exp(-150n/N) \\ g_1(T) = \frac{1}{2} + \frac{1}{2}\exp(-10T) \\ g_2(T) = \frac{1}{2} - \frac{1}{2}\exp(-10T) \\ P_{accept}(\Delta,T) = \frac{g_2(T)\exp\left(\frac{\Delta}{T}\right) - g_1(T)\frac{1-2g_2(T)}{1-2g_1(T)}}{\exp\left(\frac{\Delta}{T}\right) - \frac{1-2g_2(T)}{1-2g_1(T)}}\end{gathered} \qquad \text{Eq.126}$$

With:

N: total number of iterations to perform in the operation;

n: index of the current iteration;

$e_n(\Psi)$: error value of the n^{th} iteration, calculated for the cost function Ψ, with respect to the corresponding target function.

B. Influence of direct-detection on the hologram search

The formula developed in Chapter IV has the intensity distribution at the image plane as a wide-field continuous function whose evaluation requires infinity-bounded integrations, or at least over the whole of various Fourier-periodic expanses. In real systems, two constraints limit the application of such formula:

- The capture device in reality can have relatively limited fields of views, thus the integration may not be carried out over the required expanses.

- Except for the cases of capture devices with very high resolutions where the intensity distribution can be considered as approximately continuous, for a normal photodiode array acting as the capture device, the intensity field available as the receiver's output is at best a coarsely-sampled discrete function.

Therefore the continuous intensity-distribution formula as developed in Chapter IV must be modified, especially to accommodate the coarse sampling of realistic photo-detector arrays. As seen in Chapter IV, the hologram search depends strongly on the exact formulation of the intensity distribution, so any changes likely affect the hologram-design strategy.

The extent-limited discrete intensity distribution $J_w(\mathrm{I})$ can be expressed as a sampling function of the physical continuous unbounded function $J(\mathrm{I})$:

$$J_w(\mathrm{I}) = \mathcal{Q}\big(J(\mathrm{I})\big) = \sum_n f_n \delta(\mathrm{I} - \mathrm{I}_n) = f(\mathrm{I}) \sum_n \delta(\mathrm{I} - \mathrm{I}_n) \qquad \text{Eq.127}$$

Where f_n are the discrete values for the sampling points I_n in the image plane, $\delta(\cdot)$ the Kronecker delta function, and $f(\mathrm{I})$ a continuous function whose delta-sampling gives f_n.

In the direct-detection architecture of the receiver, each of the photodiodes acts as a spatial photon integrator which integrates all photons incident within its collection area in the image plane. The effective intensity to each of these photodiodes can thus be expressed as:

$$J_w(\mathrm{I}_n) = f_n = \int_{I'} J(\mathrm{I}')W_n(\mathrm{I}')\,d\mathrm{I}' \qquad \text{Eq.128}$$

Where $W_n(\mathrm{I})$ is windowing function for the photodiode at the sampling point I_n.

Using the assumption that the apertures of the photodiodes are identical, $W_n(\mathrm{I})$ can be expressed in terms of the base windowing function $W(\mathrm{I})$ as:

$$W_n(\mathrm{I}) = W(\mathrm{I} - \mathrm{I}_n) \qquad \text{Eq.129}$$

Substituting Eq.129 into Eq.128, the effective intensity becomes:

$$J_w(\mathrm{I}_n) = \alpha_n = \int_{I'} J(\mathrm{I}')W(\mathrm{I}' - \mathrm{I}_n)\,d\mathrm{I}' \qquad \text{Eq.130}$$

Since both the continuous intensity $J(\mathrm{I})$ and the windowing function $W(\mathrm{I})$ are real, it can be seen that $J_w(\mathrm{I}_n)$ is exactly the cross-correlation $R_{JW}(\mathrm{I}_n)$ between $J(\mathrm{I})$ and $W(\mathrm{I})$ with the spatial lag of I_n. Therefore, $f(\mathrm{I})$ in Eq.127 also takes the form of the cross-correlation $R_{JW}(\mathrm{I})$. The spatially-sampled intensity $J_w(\mathrm{I}_n)$ thus becomes:

$$J_w(\mathrm{I}) = R_{JW}(\mathrm{I}) \sum_n \delta(\mathrm{I} - \mathrm{I}_n) \qquad \text{Eq.131}$$

From Chapter IV, the expression for the continuous intensity distribution is:

$$\mathcal{J}(\mathrm{Z}) = \frac{f_2^2}{\bar{k}^6 f_1^4} \mathcal{I}\left(-\frac{f_2}{f_1}\alpha, -\frac{f_2}{f_1}\beta\right) R_{KK}\left(-\frac{f_2}{\bar{k}}\alpha, -\frac{f_2}{\bar{k}}\beta\right) \qquad \text{Eq.132}$$

From Eq.103 and the cross-correlation definition, the Fourier-domain function $\tilde{R}_{JW}(\mathrm{Z})$ can be expressed as:

$$\tilde{R}_{JW}(\mathrm{Z}) = \mathcal{J}(\mathrm{Z})\widetilde{W}(\mathrm{Z}) = \frac{f_2^2}{\bar{k}^6 f_1^4}\left(\mathcal{I}\left(-\frac{f_2}{f_1}\mathrm{Z}\right)\widetilde{W}(\mathrm{Z})\right) R_{KK}\left(-\frac{f_2}{\bar{k}}\mathrm{Z}\right) \qquad \text{Eq.133}$$

The optical power collected by the photodiode at point I_n is thus:

$$J_w(\mathrm{I}_n) = R_{JW}(\mathrm{I}_n) = \frac{f_2^2}{\bar{k}^6 f_1^4}\mathcal{F}_{\mathrm{I}_n}^{-1}\left\{\left(\check{I}\left(-\frac{f_2}{f_1}\mathrm{Z}\right)\widetilde{W}(\mathrm{Z})\right)R_{KK}\left(-\frac{f_2}{\bar{k}}\mathrm{Z}\right)\right\} \qquad \text{Eq.134}$$

Eq.134 is effectively the multiplicative point-sampling of an Inverse Fourier Transform, thus its mathematical evaluation must follow a strict order due to the non-associativity between convolution and multiplication. As a result, the optical power collected by the photodiode at a specific point I_n for a source of non-Dirac intensity distribution cannot be decomposed into a point-source response and the non-Dirac source distribution. The direct consequence of this is that coarse-sampling in the image plane renders the backward-propagation to the hologram plane ineffective, and thus the autocorrelation-based algorithms cannot be used.

A solution to this problem can be that: Beam steering can be perceived as an operation to increase the power at the desired location whilst reducing that at the other locations. From Eq.134, the ratio of the optical power collected by the photodiode at point I_n to the total non-windowed power in the image plane is:

$$\frac{J_w(\mathrm{I}_n)}{\int_{\mathrm{I}} J(\mathrm{I})\,d\mathrm{I}} = \frac{\mathcal{F}_{\mathrm{I}_n}^{-1}\left\{\left(\check{I}\left(-\frac{f_2}{f_1}\mathrm{Z}\right)\widetilde{W}(\mathrm{Z})\right)R_{KK}\left(-\frac{f_2}{\bar{k}}\mathrm{Z}\right)\right\}}{\check{I}(0,0)R_{KK}(0,0)} \qquad \text{Eq.135}$$

Steering the optical beam to I_n is equivalent to increasing the ratio in Eq.135 to as close to 1 as possible. It can be seen that this ratio can be calculated entirely at the hologram plane for a known source distribution, thus allowing some types of autocorrelation-based criteria.

References

[1] S. Kirkpatrick, C. D. Gelatt, Jr., and M. P. Vecchi, "Optimization by simulated annealing," *Science,* vol. 220, pp. 671-80, May 13 1983.

[2] U. Varshney, "The status and future of 802.11-based WLANs," *Computer,* vol. 36, pp. 102-105, Jun 2003.

[3] IEEE Computer Society, "IEEE Standard for Information Technology - Telecommunications and Information Exchange Between Systems - Local and Metropolitan Area Networks - Specific Requirements - Part 11: Wireless LAN Medium Access Control (MAC) and Physical Layer (PHY) Specifications," in *IEEE Std 802.11-2007 (Revision of IEEE Std 802.11-1999),* ed, 2007, pp. 1-1076.

[4] Office of Communications (Ofcom). (2010, 19 Sep 2012). *United Kingdom Frequency allocation table 2010 - Issue 16*. Available: http://stakeholders.ofcom.org.uk/binaries/spectrum/spectrum-policy-area/spectrum-management/ukfat2010.pdf

[5] Roke Manor Research. (2007, 25 Sep 2012). *The UK frequency allocations*. Available: www.roke.co.uk/download/datasheets/uk-frequency-allocations.pdf

[6] K.-J. Park, D. M. Shrestha, Y.-B. Ko, N. H. Vaidya, and L. Sha, "IEEE 802.11 WLAN for medical-grade QoS," presented at the Proceedings of the 1st ACM international workshop on Medical-grade wireless networks, New Orleans, Louisiana, USA, 2009.

[7] J. R. Barry, J. M. Kahn, W. J. Krause, E. A. Lee, and D. G. Messerschmitt, "Simulation of Multipath Impulse-Response for Indoor Wireless Optical Channels," *IEEE Journal on Selected Areas in Communications,* vol. 11, pp. 367-379, Apr 1993.

[8] G. W. Marsh and J. M. Kahn, "50-Mb/s diffuse infrared free-space link using on-off keying with decision-feedback equalization," *IEEE Photonics Technology Letters,* vol. 6, pp. 1268-1270, 1994.

[9] K. Samaras, "Performance analysis of wireless infrared communication systems," Doctor of Philosophy Thesis, Department of Engineering Science, University of Oxford, Oxford, UK, 1998.

[10] F. Parand, "Cellular optical wireless communications systems," Doctor of Philosophy Thesis, Department of Engineering Science, University of Oxford, Oxford, UK, 2002.

[11] D. C. O'Brien, L. B. Zeng, H. Le Minh, G. Faulkner, J. W. Walewski, and S. Randel, "Visible light communications: Challenges and possibilities," in *Personal, Indoor and Mobile Radio Communications, 2008. PIMRC 2008. IEEE 19th International Symposium on*, 2008, pp. 1-5.

[12] J. M. Kahn and J. R. Barry, "Wireless infrared communications," *Proceedings of the IEEE,* vol. 85, pp. 265-298, 1997.

[13] J. G. Proakis and M. Salehi, *Digital Communications*, 5th ed. London: McGraw-Hill, 2008.

[14] J. M. Kahn, R. You, P. Djahani, A. G. Weisbin, B. K. Teik, and A. Tang, "Imaging diversity receivers for high-speed infrared wireless communication," *IEEE Communications Magazine,* vol. 36, pp. 88-94, Dec 1998.

[15] D. A. Steigerwald, J. C. Bhat, D. Collins, R. M. Fletcher, M. O. Holcomb, M. J. Ludowise, *et al.*, "Illumination with solid state lighting technology," *IEEE Journal of Selected Topics in Quantum Electronics,* vol. 8, pp. 310-320, Mar-Apr 2002.

[16] EU-commissioned projects: Organic LEDs for ICT and lighting applications (OLLA - www.olla-project.org); OLED100.EU (www.oled100.eu) (both last accessed: 19 Sep 2012).

[17] P. Visser. (2009, 29 Sep 2012). *The OLLA project: Final activity report 2009*. Available: www.hitech-projects.com/euprojects/olla/external%20deliverables/PUBLIC%20OLLA_FINAL_ACTIVITY_REPORT_V3.0.pdf

[18] S. P. Grabowski. (2009, 29 Sep 2012). *OLED100.EU Report: Three aesthetical perception case studies 2009*. Available: http://www.oled100.eu/pdf/D5_2_Three_aesthetical_perception_PUBLIC.pdf

[19] International Commission on Non-Ionizing Radiation Protection (ICNIRP), "Guidelines on limits of exposure to broad-band incoherent optical radiation (0.38 to 3µm)," *Health Physics,* vol. 73, pp. 539-554, 1997.

[20] International Commission on Non-Ionizing Radiation Protection (ICNIRP), "Guidelines on limits of exposure to laser radiation of wavelengths between 180 nm and 1 mm," *Health Physics,* vol. 71, pp. 804-819, 1996.

[21] International Commission on Non-Ionizing Radiation Protection (ICNIRP), "Revision of the Guidelines on Limits of Exposure to Laser radiation of wavelengths between 400nm and 1.4µm," *Health Physics,* vol. 79, pp. 431-440, 2000.

[22] Fraunhofer Heinrich Hertz Institute. (15-May-2013). *Photonic Networks and Systems: Optical Wireless Communication*. Available: www.hhi.fraunhofer.de/fields-of-competence/photonic-networks-and-systems/research-topics/optical-indoor-networks/optical-wireless-communication.html

[23] PureVLC Ltd. (15-May-2013). *What is Li-Fi? - Video: Li-Fire* Available: http://purevlc.com/what-is-li-fi/video-li-fire/

[24] IEEE Computer Society, "IEEE Standard for Local and Metropolitan Area Networks - Part 15.7: Short-Range Wireless Optical Communication Using Visible Light," in *IEEE Std 802.15.7-2011*, ed, 2011, pp. 1-309.

[25] L. B. Zeng, D. O'Brien, H. Le-Minh, K. W. Lee, D. K. Jung, and Y. J. Oh, "Improvement of Date Rate by using Equalization in an Indoor Visible Light Communication System," in *Circuits and Systems for Communications, 2008. ICCSC 2008. 4th IEEE International Conference on*, 2008, pp. 678-682.

[26] H. Le Minh, D. O'Brien, G. Faulkner, L. Zeng, K. Lee, D. Jung, *et al.*, "High-Speed Visible Light Communications Using Multiple-Resonant Equalization," *IEEE Photonics Technology Letters,* vol. 20, pp. 1243-1245, 2008.

[27] L. B. Zeng, H. Le Minh, D. O'Brien, G. Faulkner, K. W. Lee, D. K. Jung, *et al.*, "Equalisation for high-speed Visible Light Communications using white-LEDs," in *Communication Systems, Networks and Digital Signal Processing, 2008. CNSDSP 2008. 6th International Symposium on*, 2008, pp. 170-173.

[28] H. Le Minh, D. O'Brien, G. Faulkner, L. B. Zeng, K. W. Lee, D. K. Jung, *et al.*, "100-Mb/s NRZ Visible Light Communications Using a Postequalized White LED," *IEEE Photonics Technology Letters,* vol. 21, pp. 1063-1065, 2009.

[29] M. D. A. Mohamed and S. Hranilovic, "Optical Impulse Modulation for Indoor Diffuse Wireless Communications," *IEEE Transactions on Communications,* vol. 57, pp. 499-508, Feb 2009.

[30] S. Jivkova, B. A. Hristov, and M. Kavehrad, "Power-efficient multispot-diffuse multiple-input-multiple-output approach to broad-band optical wireless communications," *IEEE Transactions on Vehicular Technology,* vol. 53, pp. 882-889, May 2004.

[31] S. Hranilovic and F. R. Kschischang, "A pixelated MIMO wireless optical communication system," *IEEE Journal of Selected Topics in Quantum Electronics*, vol. 12, pp. 859-874, Jul-Aug 2006.

[32] M. D. A. Mohamed and S. Hranilovic, "Two-dimensional binary halftoned optical intensity channels," *IET Communications*, vol. 2, pp. 11-17, Jan 2008.

[33] L. B. Zeng, D. C. O'Brien, H. Le Minh, G. E. Faulkner, K. Lee, D. Jung, *et al.*, "High Data Rate Multiple Input Multiple Output (MIMO) Optical Wireless Communications Using White LED Lighting," *IEEE Journal on Selected Areas in Communications*, vol. 27, pp. 1654-1662, Dec 2009.

[34] D. C. O'Brien, J. J. Liu, G. E. Faulkner, S. Sivathasan, W. W. Yuan, S. Collins, *et al.*, "Design and Implementation of Optical Wireless Communications with Optically Powered Smart Dust Motes," *IEEE Journal on Selected Areas in Communications*, vol. 27, pp. 1646-1653, Dec 2009.

[35] E. Hecht, *Optics*, 4th ed. London: Addison-Wesley, 2002.

[36] K. Hirabayashi, T. Yamamoto, S. Hino, Y. Kohama, and K. Tateno, "Optical beam direction compensating system for board-to-board free space optical interconnection in high-capacity ATM switch," *Journal of Lightwave Technology*, vol. 15, pp. 874-882, May 1997.

[37] N. Bokor and N. Davidson, "Beam shaping with diffuse light by use of a single reflection," *Applied Optics*, vol. 40, pp. 2132-2137, May 1 2001.

[38] B. B. Chhetri, Y. Shiyuan, and T. Shimomura, "Design of binary Fourier holograms using DBS for reduced-speckle-reconstruction," in *Lasers and Electro-Optics, 2001. CLEO/Pacific Rim 2001. The 4th Pacific Rim Conference on*, 2001, pp. II-698-II-699 vol.2.

[39] H. Shi, K. Liang, S. J. Sheard, D. C. O'Brien, G. E. Faulkner, and J. C. Ricklin, "Two-dimensional wavelength routing for transparent optical wireless networking," *Free Space Laser Communications V*, vol. 5892, pp. 58920Z-58920Z-12, 2005.

[40] Texas Instruments Inc, "Using Lasers with DLP DMD technology " TI DN 2509927, 13-Jun-2013 2013.

[41] B. Lofving and S. Hard, "Beam steering with two ferroelectric liquid-crystal spatial light modulators," *Optics Letters*, vol. 23, pp. 1541-3, Oct 1 1998.

[42] Texas Instruments Inc, "DMD 101: Introduction to Digital Micromirror Device (DMD) Technology," DLPA008, 14-Dec-2009 2009.

[43] Fraunhofer Institute for Photonic Microsystems IPMS. (15-May-2013). *MEMS Scanners*. Available: http://www.ipms.fraunhofer.de/en/applications/mems-scanners.html

[44] Fraunhofer Institute for Photonic Microsystems IPMS, "Spatial light modulators (SLM)," ed.

[45] A. Akatay and H. Urey, "Design and optimization of microlens array based high resolution beam steering system," *Optics Express*, vol. 15, pp. 4523-9, Apr 16 2007.

[46] K. Liang, H. Shi, S. J. Sheard, and D. C. O'Brien, "Transparent optical wireless hubs using wavelength space division multiplexing," *Free Space Laser Communications IV*, vol. 5550, pp. 80-87, 2004.

[47] S. Serati and J. Stockley, "Advanced liquid crystal on silicon optical phased arrays," in *Aerospace Conference Proceedings, 2002. IEEE*, 2002, pp. 3-1395-3-1402 vol.3.

[48] S. R. Davis, G. Farca, S. D. Rommel, A. W. Martin, and M. H. Anderson, "Analog, non-mechanical beam-steerer with 80 degree field of regard," *Acquisition, Tracking, Pointing, and Laser Systems Technologies XXII,* vol. 6971, pp. G9710-G9710, 2008.

[49] B. Apter, E. Bahat-Treidel, and U. Efron, "Continuously controllable, wide-angle liquid crystal beam deflector based on the transversal field effect in a three-electrode cell," *Optical Engineering,* vol. 44, pp. 054001-054001, May 2005.

[50] Y. M. Lee, J. S. Gwag, Y. Choi, K. H. Lee, C. J. Yu, and J. H. Ki, "Fast switching characteristics of a microlens array using the electroclinic effect of SmA* liquid crystals," *Applied Optics,* vol. 48, pp. 3737-3741, Jul 1 2009.

[51] N. R. Smith, D. C. Abeysinghe, J. W. Haus, and J. Heikenfeld, "Agile wide-angle beam steering with electrowetting microprisms," *Optics Express,* vol. 14, pp. 6557-63, Jul 10 2006.

[52] A. W. Sarto, R. T. Weverka, and K. Wagner, "Beam-Steering and Jammer-Nulling Photorefractive Phased-Array Radar Processor," *Optoelectronic Signal Processing for Phased-Array Antennas Iv,* vol. 2155, pp. 378-388, 1994.

[53] N. A. Clark, M. A. Handschy, and S. T. Lagerwall, "Ferroelectric Liquid Crystal Electro-Optics Using the Surface Stabilized Structure," *Molecular Crystals and Liquid Crystals,* vol. 94, pp. 213-233, 1983.

[54] M. A. Seldowitz, J. P. Allebach, and D. W. Sweeney, "Synthesis of digital holograms by direct binary search," *Applied Optics,* vol. 26, pp. 2788-98, Jul 15 1987.

[55] J. Schwider, W. Stork, N. Streibl, and R. Volkel, "Possibilities and limitations of space-variant holographic optical elements for switching networks and general interconnects," *Applied Optics,* vol. 31, pp. 7403-10, Dec 10 1992.

[56] D. C. O'Brien, "Dynamic holograms for optical interconnection," Doctor of Philosophy Thesis, Department of Engineering, University of Cambridge, Cambridge, UK, 1993.

[57] D. C. O'Brien, R. J. Mears, T. D. Wilkinson, and W. A. Crossland, "Dynamic holographic interconnects that use ferroelectric liquid-crystal spatial light modulators," *Applied Optics,* vol. 33, pp. 2795-2803, 05/10 1994.

[58] B. B. Chhetri, S. Yang, and T. Shimomura, "Stochastic approach in the efficient design of the direct-binary-search algorithm for hologram synthesis," *Applied Optics,* vol. 39, pp. 5956-64, Nov 10 2000.

[59] W. Yu, K. Takahara, T. Konishi, T. Yotsuya, and Y. Ichioka, "Fabrication of multilevel phase computer-generated hologram elements based on effective medium theory," *Applied Optics,* vol. 39, pp. 3531-6, Jul 10 2000.

[60] C. A. T. H. Tee, W. A. Crossland, T. D. Wilkinson, and A. A. Davey, "Binary phase modulation using electrically addressed transmissive and silicon backplane spatial light modulators," *Optical Engineering,* vol. 39, pp. 2527-2534, Sep 2000.

[61] M. Keren, I. Richter, and P. Fiala, "Iterative Fourier transform algorithm: comparison of various approaches," *Journal of Modern Optics,* vol. 49, pp. 1851-1870, 2002/09/01 2002.

[62] M. Meister and R. J. Winfield, "Novel approaches to direct search algorithms for the design of diffractive optical elements," *Optics Communications,* vol. 203, pp. 39-49, Mar 1 2002.

[63] D. Abookasis, A. Batikoff, H. Famini, and J. Rosen, "Performance comparison of iterative algorithms for generating digital correlation holograms used in optical security systems," *Applied Optics,* vol. 45, pp. 4617-4624, Jul 1 2006.

[64] G. Milewski, D. Engstrom, and J. Bengtsson, "Diffractive optical elements designed for highly precise far-field generation in the presence of artifacts typical for pixelated spatial light modulators," *Applied Optics,* vol. 46, pp. 95-105, Jan 1 2007.

[65] S. Zwick, T. Haist, M. Warber, and W. Osten, "Dynamic holography using pixelated light modulators," *Applied Optics,* vol. 49, pp. F47-F58, Sep 1 2010.

[66] C. Oh, S. Isikman, and A. Ozcan, "Lensfree polarization microscopy on a chip using incoherent digital holography," in *Lasers and Electro-Optics (CLEO) and Quantum Electronics and Laser Science Conference (QELS), 2010 Conference on*, 2010, pp. 1-2.

[67] H. Tamura and Y. Torii, "Enhancement of the Lohmann-type computer-generated hologram encoded by direct multilevel search algorithm," *Optical Review,* vol. 19, pp. 131-141, May 2012.

[68] W. A. Crossland and A. B. Davey, "Addressing requirements for chiral smectic liquid crystal active backplane spatial light modulators," *Ferroelectrics,* vol. 149, pp. 361-374, 1993/12/01 1993.

[69] P. Vachiramon, "Free-space optical communications with retro-reflecting acquisition and turbulence compensation," Doctor of Philosophy Thesis, Department of Engineering Science, University of Oxford, Oxford, UK, 2009.

[70] O. Katz, E. Small, and Y. Silberberg, "Looking around corners and through thin turbid layers in real time with scattered incoherent light," *Nature Photonics,* vol. 6, pp. 549-553, Aug 2012.

[71] P. Vachiramon, G. E. Faulkner, and D. C. O'Brien, "Direct current balancing algorithm for FLCOS binary phase holograms," *Optics Letters,* vol. 32, pp. 3275-3277, 15 Nov 2007.

[72] J. S. Liu, A. J. Caley, and M. R. Taghizadeh, "Diffractive optical elements for beam shaping of monochromatic spatially incoherent light," *Applied Optics,* vol. 45, pp. 8440-7, Nov 20 2006.

[73] P. H. van Cittert, "Die Wahrscheinliche Schwingungsverteilung in Einer von Einer Lichtquelle Direkt Oder Mittels Einer Linse Beleuchteten Ebene," *Physica,* vol. 1, pp. 201-210, 1934.

[74] F. Zernike, "The concept of degree of coherence and its application to optical problems," *Physica,* vol. 5, pp. 785-795, 1938.

[75] M. Born and E. Wolf, *Principles of optics: Electromagnetic theory of propagation, interference and diffraction of light*, 7th ed. Cambridge: Cambridge University Press, 1999.

[76] J. W. Goodman, *Introduction to Fourier Optics*, 2nd ed. Singapore: McGraw-Hill, 1996.

[77] V. Jungnickel, V. Pohl, S. Nonnig, and C. von Helmolt, "A physical model of the wireless infrared communication channel," *IEEE Journal on Selected Areas in Communications,* vol. 20, pp. 631-640, Apr 2002.

[78] G. J. Foschini, "Layered space-time architecture for wireless communication in a fading environment when using multi-element antennas," *Bell Labs Technical Journal,* vol. 1, pp. 41-59, 2002.

[79] G. J. Foschini and M. J. Gans, "On Limits of Wireless Communications in a Fading Environment when UsingMultiple Antennas," *Wireless Personal Communications,* vol. 6, pp. 311-335, 1998.

[80] E. Telatar, "Capacity of multi-antenna Gaussian channels," *European Transactions on Telecommunications,* vol. 10, pp. 585-595, Nov-Dec 1999.

[81] A. C. Boucouvalas, "IEC 825-1 eye safety classification of some consumer electronic products," in *Optical Free Space Communication Links, IEE Colloquium on*, 1996, pp. 13/1-13/6.

[82] J. M. Wang and B. Daneshrad, "A comparative study of MIMO detection algorithms for wideband spatial multiplexing systems," in *Wireless Communications and Networking Conference, 2005 IEEE*, 2005, pp. 408-413 Vol. 1.

[83] H. Yao and G. W. Wornell, "Lattice-reduction-aided detectors for MIMO communication systems," in *Global Telecommunications Conference, 2002. GLOBECOM '02. IEEE*, 2002, pp. 424-428 vol.1.

[84] P. W. Wolniansky, G. J. Foschini, G. D. Golden, and R. A. Valenzuela, "V-BLAST: an architecture for realizing very high data rates over the rich-scattering wireless channel," in *Signals, Systems, and Electronics, 1998. ISSSE 98. 1998 URSI International Symposium on*, 1998, pp. 295-300.

[85] R. Penrose, "A generalized inverse for matrices," *Mathematical Proceedings of the Cambridge Philosophical Society*, vol. 51, pp. 406-413, 1955.

[86] Y. C. Ko. (2009, 29 Sep 2012). *KEEE494 Communication Systems and Lab: MMSE Detection for Spatial Multiplexing MIMO (SM-MIMO)*. Available: http://ocw.korea.edu/ocw/college-of-engineering/communciation-systems-and-lab/lecture-note-data/week12.pdf

[87] I. Berenguer, J. Adeane, I. J. Wassell, and X. D. Wang, "Lattice-reduction-aided receivers for MIMO-OFDM in spatial multiplexing systems," in *Personal, Indoor and Mobile Radio Communications, 2004. PIMRC 2004. 15th IEEE International Symposium on*, 2004, pp. 1517-1521 Vol.2.

[88] J. Adeane, M. R. D. Rodrigues, I. Berenguer, and I. J. Wassell, "Improved detection methods for MIMO-OFDM-CDM communication systems," in *Vehicular Technology Conference, 2004. VTC2004-Fall. 2004 IEEE 60th*, 2004, pp. 1604-1608 Vol. 3.

[89] J. Adeane, M. R. D. Rodrigues, and I. J. Wassell, "Lattice-reduction-aided detection for MIMO-OFDM-CDM communication systems," *IET Communications*, vol. 1, pp. 526-531, Jun 2007.

[90] A. Cano-Gutierrez, M. Stojanovic, and J. Vidal, "Effect of channel estimation error on the performance of SVD-based MIMO communication systems," in *Personal, Indoor and Mobile Radio Communications, 2004. PIMRC 2004. 15th IEEE International Symposium on*, 2004, pp. 508-512 Vol.1.

[91] E. K. S. Au and M. Wai Ho, "Exact Bit Error Rate for SVD-based MIMO systems with Channel Estimation Errors," in *Information Theory, 2006 IEEE International Symposium on*, 2006, pp. 2289-2293.

[92] J. Wang, S. Jin, Z. L. Liu, Y. Wang, and X. H. Yu, "WLC06-3: Analysis of the Sum Capacity of MIMO Broadcast Systems with Channel Estimation Errors," in *Global Telecommunications Conference, 2006. GLOBECOM '06. IEEE*, 2006, pp. 1-5.

[93] C.-E. Chen, "Lattice-reduction-aided MIMO detection under imperfect channel state information," in *Acoustics Speech and Signal Processing (ICASSP), 2010 IEEE International Conference on*, 2010, pp. 3446-3449.

[94] F. Tsuzuki and T. Ohtsuki, "SPC03-6: SAGE Algorithm for Channel Estimation and Data Detection Using Superimposed Training in MIMO System," in *Global Telecommunications Conference, 2006. GLOBECOM '06. IEEE*, 2006, pp. 1-5.

[95] M. Yoshino, S. Haruyama, and M. Nakagawa, "High-accuracy positioning system using visible LED lights and image sensor," in *Radio and Wireless Symposium, 2008 IEEE*, 2008, pp. 439-442.

[96] A. H. Azhar, T.-A. Tran, and D. O'Brien, "Demonstration of high-speed data transmission using MIMO-OFDM visible light communications," in *GLOBECOM Workshops (GC Wkshps), 2010 IEEE*, 2010, pp. 1052-1056.

[97] L. N. Trefethen and D. Bau III, *Numerical linear algebra*. Philadelphia: SIAM, 1997.

[98] S. Winitzki. (2008, 21 Sep 2012). *A handy approximation for the error function and its inverse (06 Feb 2008 ed.)*. Available: http://sites.google.com/site/winitzki/sergei-winitzkis-files/erf-approx.pdf

[99] M. J. M. Peacock, I. B. Collings, and M. L. Honig, "A relationship between the SINR of MMSE and ALS receivers," in *Information Theory, 2005. ISIT 2005. Proceedings. International Symposium on*, 2005, pp. 327-331.

[100] P. Li, D. Paul, R. Narasimhan, and J. Cioffi, "On the distribution of SINR for the MMSE MIMO receiver and performance analysis," *IEEE Transactions on Information Theory*, vol. 52, pp. 271-286, Jan 2006.

[101] MathWorks Inc. (2009, 19 Jan 2010). *MATLAB® 7 - Function Reference: Volume 2 (F-O) (R2009b ed.)*. Available: www.mathworks.com/help/releases/R2009b/pdf_doc/matlab/refbook2.pdf

[102] M. S. Mueller, R.; McHugh, R., "Total Jitter Measurement at Low Probability Levels, Using Optimized BERT Scan Method," Agilent Technologies, White Paper 2005.

[103] I. Glover and P. Grant, *Digital communications*. London: Prentice Hall, 2000.

[104] J. S. Liu, A. J. Caley, A. J. Waddie, and M. R. Taghizadeh, "Comparison of simulated quenching algorithms for design of diffractive optical elements," *Applied Optics*, vol. 47, pp. 807-16, Feb 20 2008.

[105] S. Boyd and L. Vandenberghe, *Convex optimization*. Cambridge: Cambridge University Press, 2008.

[106] J. C. Spall, *Introduction to stochastic search and optimization: Estimation, Simulation, and Control*. New Jersey: John Wiley & Sons, 2003.

[107] T. Cormen, C. Leiserson, R. Rivest, and C. Stein, *Introduction to Algorithms*, 3rd ed. Cambridge: MIT Press, 2009.

[108] A. Atukorala, "Visible light communications," Master of Engineering Project report, Department of Engineering Science, University of Oxford, Oxford, UK, 2010.

[109] CRL Opto Ltd, "SXGA-R2-H1 Datasheet," 2003.

[110] Matrox Electronic Systems Ltd., "Camera interface guide," Guideline03-November-2010 2010.

[111] National Instruments Corp., "IMAQ PCI/PXI-1407 User Manual," 2001.

[112] T. D. Wilkinson, W. A. Crossland, S. T. Warr, T. C. B. Yu, A. B. Davey, and R. J. Mears, "New Applications for Ferroelectric Liquid Crystals," *Liquid Crystals Today*, vol. 4, pp. 1-6, 1994/12/01 1994.

[113] Thorlabs GmbH, "Operations Manual Thorlabs Blueline Series Laser Diode Controller LDC 2xx," 20-June-2006 2006.

[114] Hewlett Packard, "HP 8112A 50MHz Programmable Pulse Generator Operating, Programming and Servicing Manual," 1992.

[115] MathWorks Inc. (2009, 19 Jan 2012). *MATLAB® 7 - Function Reference: Volume 1 (A-E) (R2009b ed.)*. Available: www.mathworks.com/help/releases/R2009b/pdf_doc/matlab/refbook.pdf

[116] A. H. Azhar, T.-A. Tran, and D. C. O'Brien, "A Gigabit/s Indoor Wireless Transmission Using MIMO-OFDM Visible-Light Communications," *IEEE Photonics Technology Letters,* vol. 25, pp. 171-174, Jan 15 2013.